Numerical study of convection and dynamo in a rotating spherical shell: Implications for solidification scenarios in planetary cores

谷口, 陽菜実

2020年度　博士論文

Numerical study of convection and dynamo in a rotating spherical shell: Implications for solidification scenarios in planetary cores

Department of Earth and Planetary Sciences

Graduate School of Science, Kyushu University

Deep Earth Physics Group

Hinami Taniguchi

谷口　陽菜実

February, 2021

Contents

Abstract

Critical convective flows and dynamos driven by bottom-up and top-down buoyancy are examined for an electrically conducting Boussinesq fluid in a rotating spherical shell. This system represents dynamics and dynamos in terrestrial planetary core, in which it is believed that the compositional source of buoyancy is mainly supplied by bottom-up type for the Earth and the Mercury, and by top-down type for the Ganymede, currently. Although it is recognized that dynamos driven by the different mechanisms tend to have distinguishably different magnetic fields, the reason why the differences arise has not yet been known. Understanding the physics of the core convection and dynamos is important for unveiling the thermal history and internal structure in various bodies. In order to understand the basic features of convection and dynamos, we investigate linear stability of convection without magnetic fields, and then, dynamos, in which the obtained critical convection are given as initial condition, for both top-down and bottom-up buoyancy types.

First, the onsets of bottom-up and top-down convection are searched for the Prandtl number, P_r, fixed at 1. The Ekman number, E_k, is varied from 5×10^{-5} to 10^{-3}, and the critical value of the Rayleigh number, Ra, is obtained at each E_k. The critical Rayleigh number, Ra_c, varies in proportion to $E_k^{-1.14}$ in the bottom-up case, and $E_k^{-1.28}$ in the top-down case. It is consistent with previous works[1], but a little difference, especially for the bottom-up case, could be caused by two factors: E_k is not sufficiently low, and the flow patterns are different from the local analysis. The radial position of the columnar convection is located at the middle of the shell for the top-down case, and adjacent to the inner core tangent cylinder for the bottom-up case. Although the main convection column exists outside the tangent cylinder, the bottom-up type flows have influx and outflux through the tangent cylinder to conserve the mass around the inner boundary at low latitudes. The non-convective influx and outflux in the bottom-up cases plays a role in balancing the total kinetic energy budget by increasing the viscous dissipation.

The onsets of the dynamos are obtained at $P_r = 1$ and $E_k = 10^{-4}$. It is found that the critical Rayleigh number of a self-sustaining dynamo is $4.5Ra_c$ in top-down case, but it is not obtained until $Ra = 20Ra_c$ in bottom-up case. The successful dynamos for top-down buoyancy cases generate magnetic fields with low dipolarity on the outer boundary. This could result from the weak influence of the convection column on the total kinetic energy. The flows in both successful and failed dynamos are dominated by the zonal flows owing not to the thermal wind but to the Reynolds stresses. However, in many previous works, the full MHD dynamo action driven by the bottom-up buoyancy has the thermal wind in the zonal flows. Because achieving the successful dynamo driven by the bottom-up buoyancy is more difficult than that by top-down buoyancy according to our results, the zonal flows formed by the thermal wind could be required in the bottom-up-driven dynamos. It is possible that the absence of thermal wind is caused by coupling equatorially symmetric flows only with antisymmetric magnetic fields. The difference in the force balance of the zonal flows between the top-down and bottom-up dynamos could affect the temporal variation of the observed magnetic field in each terrestrial body.

Acknowledgements

All the study in this thesis has been carried out at the Deep Earth Physics Laboratory, while I was in a doctoral course at the Department of Earth and Planetary Sciences, Graduate School of Science, Kyushu University.

I would like to express my sincere gratitude to my supervisor, Associate Prof. Futoshi Takahashi for his continuous support, encouragement, and patience. I would like to thank Prof. Satoshi Kaneshima and Associate Prof. Shigeo Yoshida for disscussion and incisive comments in our research seminars.

Chapter 1

Introduction

1.1   Planetary core dynamo

The core dynamos in the current terrestrial bodies are powered and sustained by a certain kind of compositional buoyancy sources. The solidification scenarios for each body are decided by three factor: pressure, temperature distribution and contents of light element in the core. Here, we focus on sulfur as the representative of the light elements. The eutectic temperature and the eutectic composition of the Fe-FeS core depend on the core pressure, and the temperature distribution. The amount of sulfur decides whether the core is in the Fe-rich side or FeS-rich side in the phase diagram. Table 1 shows basic information of the structure and the observed magnetic field for Earth, Mercury and Ganymede, which currently have the intrinsic fields maintained by the core dynamo (Connerney, 2007[2]). The geodynamo generates the strongest magnetic field of about 10^4nT in the three bodies. In case of the Earth, density deficit of the outer core inferred from the typical seismic velocity structure such as PREM (Preliminary Reference Earth Model: Dziewonski and Anderson, 1981[3]) suggests the presence of some light elements of $\sim 10\%$ in the outer core. This observational evidence implies that the Earth's core lies in the Fe-rich side. Under the circumstances of the Earth's core, if the melting curve of iron has a slope steeper than that of the adiabatic temperature in the P-T diagram, the inner core nucleation should start at the geocenter in the Earth's thermal evolution. Since light elements are incompatible with the solid iron, they are not included into the inner core upon solidification but left at the solidification front, giving rise to compositional buoyancy. Thus, in the core, it is believed that the main buoyancy is currently fed by light element ejection due to the inner core growth; here, I refer to the mechanism supplying buoyancy from the bottom of the outer core as 'bottom-up' type. The solidification is often followed by the ejection of thermal buoyancy released by latent heat at the inner core boundary.

In the case of the Mercury, the strength of magnetic field on the surface is very low because the core size is more than 75 percent depth in the planetary radius (Smith et al. 2012[5]; Hauck et al. 2013[6]; Rivoldini and Van Hoost 2013[7]). It is unknown why the weak magnetic field is sustained by core dynamo. In addition to the strength, the compositional buoyancy type in the core is ambiguous because the core could have silicate as well as sulfur (e.g., Malavergne et al. 2010[8]; Chabot et al. 2014[9]). Hence, the core may need to be considered as a Fe-Si-S system. According to numerical study by dynamo simulation (Takahashi et al. 2019[10]), it is, however, possible that bottom-up type dynamo generates the magnetic field with an offset dipole, consistent with MESSENGER observation (Anderson et al. 2012[11]; Johnson et al. 2012[12]). If the core should be a Fe-FeS system, compositional buoyancy is

Table 1.1: Basic information of the Earth, Mercury and Ganymede.[4]

	Earth	Mercury	Ganymede
Planetary radius (km)	6371	2439	2632
Core radius (km)	3480	1965 - 2050	650 - 880
Pressure at the CMB (GPa)	139	2.8 - 3.3	5.5 - 7.0
Pressure at the center (GPa)	357	33 - 37	9.5 - 11
Strength of magnetic field at planetary surface (nT)	30000	700	700
$E_m(quadrupole)/E_m(dipole)$	0.14	0.33	0.04

Strength of magnetic field is at equatorial surface in Earth and Ganymede, and at high northern latitudes in Mercury. $E_m(quarupole)$ and $E_m(dipole)$ is magnetic power of the quadrupole and dipole fields at the planetary surface.

fed by inner core growth for the Fe-rich core, or by FeS floatation for the FeS-rich core.

The Ganymede's core could have the different buoyancy source type with the Earth's one. Pressure in the Ganymede's core is less than 10GPa according to table 1, and the estimated sulfur concentration in the core is 12 to 20wt%S according to Kuskov and Kronrod (2001)[13]. Under the conditions, the melting curve of iron in the Fe-rich core has a negative slope in the P-T diagram (e.g., Fei et al. 1997[14], 2000[15]; Chudinovskikh and Boehler 2007[16]; Stewart et al. 2007[17]; Chen et al. 2008[18]; Buono and Walker 2011[19]). Then, the iron solidification could start at the core-mantle boundary, resulting in 'iron snow' (Hauck et al. 2006[20]). The iron snow remelts at some depth during free fall, and gives a negative buoyancy near the outer boundary. Here, such a mechanism is classified as 'top-down' type. However, it is known that the dynamos driven by top-down buoyancy trends to generate a non-dipole dominant field (Zhan and Schubert 2012[21]), except for the cases with a stably stratified layer on the outer boundary as a snow zone (Christensen 2015[22]). Driving force of the Ganymede's dynamo still has been in debate.

As mentioned above, compositional convection in these terrestrial bodies is driven by either bottom-up or top-down type buoyancy. However, it is highly uncertain which one is actually chosen due to lack of information about light elements contained in the core.

1.2 General theory of MHD in the core

1.2.1 Core flow

Core dynamics in the terrestrial bodies is primarily governed by the strong effects of rotation and magnetic field as in Table 1.2, which shows the basic physical properties in the Earth's core in terms of the non-dimensional number (Roberts and King (2013)[23]). The most important parameters is the Ekman number defined by

$$E_k = \frac{\nu}{2\Omega D^2} \tag{1.1}$$

where ν is the kinetic viscosity of the fluid, Ω the scale of angular velocity of rotating body, and D the thickness of the fluid layer. The Ekman number is a measure of the relative importance of the viscous force to the Coriolis force. In the core, the Ekman number is extremely smaller than unity, so that the viscous force is forced much more weakly than the Coriolis force.If the magnetic effect on the motion is small, the Coriolis force is balanced by

the force due to pressure gradient: it is so-called 'geostrophic' balance

$$2\vec{\Omega} \times \vec{u} = -\frac{1}{\rho}\vec{\nabla}P \; , \tag{1.2}$$

where $\vec{\Omega}$ is the angular velocity, $\vec{u}$ the velocity field, ρ the fluid density, and P the pressure. Taking the curl of the equation yields

$$(\vec{\Omega} \cdot \vec{\nabla})\vec{u} = 0 \; . \tag{1.3}$$

Under the force balance, thus, the flow does not change in the direction of the rotating axis, known as the Taylor-Proudman theorem. In fact, the many numerical researches for convection (e.g. Zhang and Busse (1987)[24]; Christensen (2002)[25]; Aubert (2005)[26]) and magnetoconvection (e.g. Zhang (1995)[27]; Olson and Glatzmaier (1995)[28]) obtain the flows that possess the features of the Taylor Proudman theorem. If the strong magnetic field, $\vec{B}$, is applied, the system could be in equilibrium with magnetostrophic balance:

$$2\vec{\Omega} \times \vec{u} = -\frac{1}{\rho}\vec{\nabla}P + \frac{1}{\rho}\vec{J} \times \vec{B} \; , \tag{1.4}$$

where $\vec{J}$ is electric current density, and the force of $\vec{J} \times \vec{B}$ is the Lorentz force. In order to measure the effects of the magnetic field on core dynamics, using the Elsasser number, Λ, given by

$$\Lambda = \frac{B^2}{2\rho\mu_o\eta\Omega} \tag{1.5}$$

is useful. B is the characteristic magnetic strength, η the magnetic diffusivity, and μ_o the magnetic permeability in free space, where the magnetic diffusivity is related with the electrical conductivity, σ, as

$$\eta = \frac{1}{\sigma\mu_o} \; .$$

The Elsasser number is defined by the ratio of the Lorentz force to the Coriolis force. As the Elsasser number is of the order of 10 (Table 1.2), it is likely that the geodynamo operates in the magnetostrophic state.

In addition to the magnetostrophic flows, the observation of the geomagnetic field suggests that the Earth's core has zonal flow to move the geomagnetic field westward (Pais and Hulot (2000)[29]; Finlay and Jackson (2003)[30]). The zonal flow is generated by the divergence of the Reynolds stress, the zonal thermal wind, energy exchanged by the Lorentz force and the viscous force. For convection without magnetic field, the Reynolds stresses is dominated in the kinetic energy budget of zonal flow (e.g. Busse (1970)[31]; Busse and Hood (1982)[32]; Aubert et al. (2001)[33]; Christensen (2002)[25]). When the effect of magnetic field is added in the system, the geostrophic zonal flow is destroyed by the Lorentz force, and the zonal thermal wind becomes dominant in the dipole-dominant dynamo driven by bottom-up type buoyancy (Aubert (2005)[26]). Most dynamos driven by top-down type buoyancy has geostrophic zonal flow, although boundary conditions of velocity often affect the zonal flow when the Ekman number is not close to zero (Simitev and Busse (2005)[34]).

Table 1.2: Basic physical properties in the Earth's core in terms of the non-dimensional numbers.

Dimensionless parameter	Definition	Core
Elsasser number, Λ	$B^2 \,/\, 2\Omega\eta\rho\mu_o$	10
Ekman number, E_k	$\nu \,/\, 2\Omega D^2$	10^{-15}
Magnetic Reynolds number, Rm	$\mathcal{U}D \,/\, \eta$	10^3
Magnetic Prandtl number, Pm	$\nu \,/\, \eta$	10^{-6}
Prandtl number, Pr	$\nu \,/\, \kappa$	10^{-1}
Rayleigh number, Ra	$g_o D\alpha\Delta T_c \,/\, 2\Omega\kappa$	10^9
Schmidt number, S_c	$\nu \,/\, \kappa^\xi$	10^2

α is the coefficient of thermal expansion, ΔT_c is the difference in the temperature of the core-mantle boundary and Earth's surface, κ and κ^ξ are the thermal and composition diffusivity, respectively, and g is the gravitational acceleration.

1.2.2 MHD approximation

First, Maxwell's equations and Ohm's law give

$$\vec{\nabla} \times \left(\mu_o^{-1}\vec{B} \right) = \vec{J} + \frac{\partial \vec{D}}{\partial t} \tag{1.6}$$

$$\vec{\nabla} \times \vec{E} = -\frac{\partial \vec{B}}{\partial t} \tag{1.7}$$

$$\vec{\nabla} \cdot \vec{B} = 0 \tag{1.8}$$

$$\vec{\nabla} \cdot \vec{D} = q \,, \tag{1.9}$$

$$\vec{J} = \sigma(\vec{E} + \vec{u} \times \vec{B}) \,, \tag{1.10}$$

where $\vec{D}$, and $\vec{E}$ are the electric flux density, and the electric field, which are related as $\vec{D} = \varepsilon_o\vec{E}$, ε_o is the permittivity in free space, and q the volume density of charge. First, the scales of (1.7) and (1.6) is estimated:

$$\frac{E}{l} = \frac{B}{\tau_b}$$

$$\frac{B}{l\mu_o} = \varepsilon_o \frac{E}{\tau_e} \,,$$

by assuming the time scale of $\vec{E}$ and $\vec{B}$, the spetial scale, and the characteristic intensity of $\vec{E}$ and $\vec{B}$ as τ_e, τ_b, l, E, and B. The relation between the two time scales is that

$$\frac{\tau_b}{\tau_e} = \frac{1}{\varepsilon_o\mu_o} \left(\frac{B}{E} \right)^2 = \left(\frac{cB}{E} \right)^2$$

$$\tau_b\tau_e = l^2\varepsilon_o\mu_o = \left(\frac{l}{c} \right)^2 \,,$$

where c is the light speed. We consider the system in which the time scale of the magnetic field, τ_b, is much longer than the propagation time scale of the light, l/c. In this situation, another time scale, τ_e, is negligible;

$$\tau_e = \frac{l^2/c^2}{\tau_b} \ll 1 .$$

Thus, the relation of the time scales is $\tau_b \gg \tau_e$. The ratio of the term on the right hand side to the second term on the left hand side in (1.6) is written as

$$\frac{O\left(\partial \vec{D}/\partial t\right)}{O\left(\vec{\nabla} \times (\mu_o^{-1}\vec{B})\right)} = \frac{\tau_e}{\tau_b} \ll 1 ,$$

so that this condition makes the temporal variation of $\vec{D}$ removed from the equation (1.6), i.e.

$$\vec{\nabla} \times \left(\mu_o^{-1}\vec{B}\right) = \vec{J}. \tag{1.11}$$

These equations are the Maxwell equations with magnetohydrodynamics (MHD) approximation. By using (1.11), (1.7), and (1.10), the induction equation is also obtained

$$\frac{\partial \vec{B}}{\partial t} = \vec{\nabla} \times (\vec{u} \times \vec{B}) - \vec{\nabla} \times \left(\eta \vec{\nabla} \times \vec{B}\right) . \tag{1.12}$$

1.2.3 Kinematics in dynamo theory

In this section the basic theory of kinematic dynamo is introduced when the Lorentz force is negligible in the dynamics. We shall consider a basic property for fluid with a perfect conductor is zero. An infinitesimal element on any curve frozen in the fluid, dx_i, can be represented as

$$dx_i = \frac{\partial x_i}{\partial a_j}da_j ,$$

where $\vec{x}(\vec{a}, t)$ is the displacement field, which is the position of a fluid particle through $\vec{x}(\vec{a}, 0) = \vec{a}$ at $t = 0$. The Lagrangian derivative of dx_i is

$$\frac{D}{Dt}dx_i = \sum_j dx_j \nabla_j u_i . \tag{1.13}$$

The induction equation of (1.12) is rewritten as

$$\frac{D\vec{B}}{Dt} = (\vec{B} \cdot \vec{\nabla})\vec{u} - \vec{B}(\vec{\nabla} \cdot \vec{u}) . \tag{1.14}$$

Using the equation of continuity, $d\rho/dt = -\rho \vec{\nabla} \cdot \vec{u}$, where d/dt is Lagrange differentiation as $d/dt = \partial/\partial t + (\vec{u} \cdot \vec{\nabla})$, the equation (1.14) become

$$\frac{d}{dt}\left(\frac{\vec{B}}{\rho}\right) = \frac{\vec{B}}{\rho} \cdot \vec{\nabla}\, \vec{u} . \tag{1.15}$$

9

This formulation is similar to equation (1.13). Thus, $\vec{B}(\vec{x},t)/\rho(\vec{x},t)$ has the similar solution as $d\vec{x}$,

$$\frac{B_i(\vec{x},t)}{\rho(\vec{x},t)} = \frac{\partial x_i}{\partial a_j} \frac{B_j(\vec{a},0)}{\rho(\vec{a},0)} .$$

Suppose here that $d\vec{a}$ is along the magnetic field line, $\vec{B}(\vec{a},0)$, at $= 0$, so that $\vec{B}(\vec{a},0) \times d\vec{a} = 0$. The result is

$$\varepsilon_{ijk} B_j(\vec{x},t)dx_k(\vec{a},t) = \varepsilon_{ijk} \left[\frac{\partial x_j}{\partial a_m} \frac{\rho(\vec{x},t)}{\rho(\vec{a},0)} B_m(\vec{a},0) \right] \left[\frac{\partial x_k}{\partial a_n} da_n \right]$$

$$= \varepsilon_{lmn} \frac{\partial a_l}{\partial x_i} \frac{\rho(\vec{x},t)dx^3}{\rho(\vec{a},0)da^3} B_m(\vec{a},0) da_n$$

$$= \varepsilon_{lmn} \frac{\partial a_l}{\partial x_i} B_m(\vec{a},0) da_n$$

$$\left[\vec{B}(\vec{x},t) \times d\vec{x}(\vec{a},t) \right]_i = \left[\vec{B}(\vec{a},0) \times d\vec{a} \right]_l \frac{\partial a_l}{\partial x_i}$$

$$= 0 .$$

Thus, the magnetic field line is parallel to the infinitesimal displacement along the curve, so that the magnetic lines in the perfect conductor is 'frozen in' the flow, and it is so-called 'Alfvén theorem' (c.f. Moffatt, 1978[35]; Gubbins and Herrero-Bervera (2007)[36]).

When the conductor has a finite electrical conductivity, the magnetic energy is dissipated by the Joule effect. In this system the magnetic diffusion term is added in (1.14), then

$$\frac{d\vec{B}}{dt} = (\vec{B} \cdot \vec{\nabla})\vec{u} - \vec{B}(\vec{\nabla} \cdot \vec{u}) - \vec{\nabla} \times (\eta \vec{\nabla} \times \vec{B}) . \tag{1.16}$$

Multiplying $\mu_o^{-1}\vec{B}\cdot$ by (1.16), the magnetic energy equation

$$\frac{\partial}{\partial t} \left(\frac{B^2}{2\mu_o} \right) = -\vec{u} \cdot (\vec{J} \times \vec{B}) - \frac{J^2}{\sigma} - \vec{\nabla} \cdot \left(\frac{\vec{E} \times \vec{B}}{\mu_o} \right) \tag{1.17}$$

is obtained. The second term on the right hand in (1.17) is the Joule dissipation, which must decreases the magnetic energy in any non-perfect electrical conductor. The source of magnetic energy is the first term, represented by the work of the flow done against the Lorentz force. The residual term in the right hand is the magnetic energy flux convergence, known as the energy flux of the Poynting vector. When dynamo is maintained, positive contribution from the magnetic energy source in (1.17) needs to be larger than the dissipation.

There are some anti-dynamo theorems which say that the magnetic field cannot be maintained in principle by the velocity field with a certain property. First, the toroidal velocity can not drive the dynamo (Bullard and Gellman (1954)[37]). The toroidal flows can not generate enough source for overcoming the Joule dissipation. The well-known anti-dynamo theorem is known as 'Cowling's theorem' (Cowling (1933)[38]; Braginsky (1965)[39]; Ivers and James (1984)[40]). Cowling's theorem says that the axisymmetric magnetic field cannot be maintained by any axisymmetric velocity fields. Since the magnetic field satisfies equation (1.8), the axisymmetric magnetic field, $\vec{B}_o$, is represented in the cylindrical coordinate system, (s, ϕ, z), as

$$\vec{B}_o(s,z) = \vec{B}_p(s,z) + \vec{B}_t(s,z) = \vec{\nabla} \times (X(s,z)\vec{e}_\phi) + Y(s,z)\vec{e}_\phi ,$$

where $\vec{B_p}$, $\vec{B_t}$, X, Y, and $\vec{e_\phi}$ are the poloidal magnetic field, the toroidal magnetic field, the poloidal scalar, the toroidal scalar, and the unit vector in the azimuthal direction. Multiplying the induction eqution (1.12) by $\vec{e_\phi}\cdot$ and $\vec{e_\phi} \cdot \vec{\nabla}\times$ gives

$$\frac{\partial Y}{\partial t} = \left[\vec{\nabla} \times (\vec{u_t} \times \vec{B_p}) + \vec{\nabla} \times (\vec{u_p} \times \vec{B_t}) \right]_\phi + \eta \Delta_l Y$$

$$-\frac{\partial}{\partial t} \Delta_l X = \left[\vec{\nabla} \times \vec{\nabla} \times (\vec{u_p} \times \vec{B_p}) \right]_\phi - \Delta_l \Delta_l X \,,$$

where $\vec{u_p}$, $\vec{u_t}$, and Δ_l are the poloidal velocity, the toroidal velocity, and the operator

$$\Delta_l = \nabla^2 - \frac{1}{s^2} \,.$$

$[\vec{A}]_\phi$ denotes taking the azimuthal component from $\vec{A}$. The equations are rewritten

$$\frac{\partial Y}{\partial t} = \left[\vec{\nabla}(\vec{e_\phi} \cdot \vec{u_t}) \times \vec{\nabla}(sX) \right]_\phi - s\vec{u_p} \cdot \vec{\nabla} \left(\frac{Y}{s} \right) + \eta \Delta_l Y \qquad (1.18)$$

$$\frac{\partial X}{\partial t} = -\frac{1}{s} \vec{u_p} \cdot \vec{\nabla}(sX) - \Delta_l X \,. \qquad (1.19)$$

By using two relations

$$s^2 A \Delta_l A = s^3 A \vec{\nabla} \cdot \left(\frac{1}{s^2} \vec{\nabla}(sA) \right)$$

$$= \vec{\nabla} \cdot \left[sA\vec{\nabla}(sA) \right] - (\vec{\nabla}s^3 A) \cdot \left(\frac{1}{s^2} \vec{\nabla}(sA) \right)$$

$$= \vec{\nabla} \cdot \left[sA\vec{\nabla}(sA) \right] - [\vec{\nabla}(sA)]^2 - 2s^2 A \left(\frac{1}{s}\frac{\partial A}{\partial s} + \frac{1}{s^2}A \right)$$

$$= \vec{\nabla} \cdot \left[sA\vec{\nabla}(sA) - \vec{e_s}sA^2 \right] - [\vec{\nabla}(sA)]^2$$

$$s^{-2} B \Delta_l B = \frac{B}{s^3} \vec{\nabla} \cdot \left[s^2 \vec{\nabla} \left(\frac{B}{s} \right) \right]$$

$$= \vec{\nabla} \cdot \left[\frac{B}{s} \vec{\nabla} \left(\frac{B}{s} \right) \right] - \left(\vec{\nabla} \frac{B}{s^3} \right) \cdot \left(s^2 \vec{\nabla} \frac{B}{s} \right)$$

$$= \vec{\nabla} \cdot \left[\frac{B}{s} \vec{\nabla} \left(\frac{B}{s} \right) \right] - \left[\vec{\nabla} \left(\frac{B}{s} \right) \right]^2 + \frac{2}{s^2} B \left(\frac{1}{s}\frac{\partial B}{\partial s} - \frac{1}{s^2}B \right)$$

$$= \vec{\nabla} \cdot \left[\frac{B}{s} \vec{\nabla} \left(\frac{B}{s} \right) + \vec{e_s} \frac{B^2}{s^3} \right] - \left[\vec{\nabla} \left(\frac{B}{s} \right) \right]^2 \,,$$

multiplying equations (1.18) and (1.19) by $s^{-2}Y$ and $s^2 X$, respectively, and integrating the equations over the volume, we can obtain

$$\frac{d}{dt} \int_V \frac{1}{2} \left(\frac{Y}{s} \right)^2 dV = -\eta \int_V \left[\vec{\nabla} \left(\frac{Y}{s} \right) \right]^2 + \int_V \frac{Y}{s^2} \left[\vec{\nabla}(\vec{e_\phi} \cdot \vec{u_t}) \times \vec{\nabla}(sX) \right]_\phi \qquad (1.20)$$

11

$$\frac{d}{dt}\int_V \frac{1}{2}(sX)^2 dV = -\int_V \left[\vec{\nabla}(sX)\right]^2 dV \,. \tag{1.21}$$

According to equation (1.21), the poloidal magnetic energy decreases with time. Because the toroidal magnetic energy is generated by the poloidal magnetic field, the toroidal energy cannot be maintained if the poloidal energy is small in the system. Thus, when the fields have only the axisymmetric components, the poloidal magnetic energy decays, and then the toroidal magnetic energy could not increase with time if enough time is passed. It is an inevitable conclusion that we must consider a general three-dimensional problem, which strongly restricts analytic study and makes dynamo problem formidable for us.

1.2.4 Mean field theory

Dynamos driven by random ingredient of the flows have been studied as mean field electro-dynamics. In case of the cylindrical and spherical coordinate system, the mean field is often defined as the azimuthal average, while deviations from the means correspond to the fluctuating parts. Typical magnetic field generation processes derived from the mean field theory are the well-known α-effect (Parker, 1955[41]; Moffatt, 1978[35]). In addition, large-scale toroidal field is often generated by shearing large-scale poroidal field due to differential rotation, and it is so-called ω-effect (Soward, 1972[42]; Roberts, 1972[43]). When the magnetic field, $\vec{B}$, and the velocity field, $\vec{u}$, are separated in terms of the mean and the fluctuating parts, we have

$$\vec{B} = \vec{B_o} + \vec{b} \tag{1.22}$$

$$\vec{u} = \vec{U_o} + \vec{v} \,, \tag{1.23}$$

where $\vec{B_o}$ and $\vec{U_o}$ are the mean parts, and $\vec{b}$ and $\vec{v}$ are the fluctuating parts. Substituting the expression to (1.16), we obtain the equations for the mean and fluctuating parts of the magnetic field as;

$$\frac{\partial}{\partial t}\vec{B_o} = \vec{\nabla} \times (\vec{U_o} \times \vec{B_o}) + \vec{\nabla} \times <\vec{v} \times \vec{b}> + \eta\nabla^2\vec{B_o} \tag{1.24}$$

$$\frac{\partial}{\partial t}\vec{b} = \vec{\nabla} \times (\vec{U_o} \times \vec{b}) + \vec{\nabla} \times (\vec{v} \times \vec{B_o}) + \vec{\nabla} \times \vec{G} + \eta\nabla^2\vec{b} \,, \tag{1.25}$$

where

$$\vec{G} = \vec{v} \times \vec{b} - <\vec{v} \times \vec{b}> \,,$$

and $<\vec{v} \times \vec{b}>$ means the azimuthal average of $\vec{v} \times \vec{b}$. Let us decompose the mean fields into the poloidal and toroidal parts:

$$\vec{B_o} = \vec{B_p} + \vec{B_t}$$

$$\vec{U_o} = \vec{U_p} + \vec{U_t} \,,$$

then the equation (1.24) yields the equations for the poloidal and toroidal magnetic field::

$$\frac{\partial}{\partial t}\vec{B_p} = \vec{\nabla} \times (\vec{U_p} \times \vec{B_p}) + \vec{\nabla} \times \varepsilon_t + \eta\nabla^2\vec{B_p} \tag{1.26}$$

$$\frac{\partial}{\partial t}\vec{B_t} = \vec{\nabla} \times \left[\vec{U_p} \times \vec{B_t}\right] + \vec{\nabla} \times \left[\vec{U_t} \times \vec{B_p}\right] + \vec{\nabla} \times \varepsilon_p - \eta\nabla^2\vec{B_t} \,. \tag{1.27}$$

In these equations ε_t and ε_p mean the toroidal components and poloidal components of $<\vec{v} \times \vec{b}>$, respectively. The mean electro-motive force denoted by ε_t and ε_p includes the α

effect, which generates the mean fields via interaction between the fluctuating parts of the magnetic and velocity fields. Another famous effect is the ω effect, and acts as a source of the mean toroidal field through the second term on the right hand in the equation (1.27). The term is written as

$$\vec{\nabla} \times \left[\vec{U_t} \times \vec{B_p} \right] = s(\vec{B_p} \cdot \vec{\nabla})\omega$$

with $\vec{U_t} = s\omega\vec{e_\phi}$. The differential rotation term includes the ω-effect, which acts as the source of the toroidal magnetic field. The three terms by the α-effect and the ω-effect are the source of the axisymmetric magnetic fields (Kageyama and Sato (1997)[44]; Olson et al. (1999)[45]; Roberts and King (2013)[23]).

By using the effects, the dynamo types have been defined (Moffatt, 1978[35]). When contributions to the mean fields from ε_t and the ω effect are significant, the dynamos are called as '$\alpha\omega$-dynamos'. These dynamos are characterized by the mean toroidal component much stronger than mean poloidal counterpart. If the mean fields are almost generated due to the α effects, the dynamos are described as 'α^2-dynamos'. For α^2-dynamos, strength of the mean poloidal field tends to be similar to that of the mean toroidal field. Finally, so-called '$\alpha^2\omega$- dynamos' are dynamos maintained by the three contributions in magnitude. It is found that most of the numerical MHD dynamos are classified as α^2 type (Roberts and King, 2013[23]).

1.3   Previous works of linear stability analysis

The onset of thermal and/or compositional convection in a rotating spherical system has been investigated because of its importance in finding out the basic features of dynamo driven by convection in the interior of stars and planets. Convection depends upon the geometry, various physical parameters that emerge in governing equations, and the distribution of buoyancy sources and gravity. In particular, in the self-gravitating system the distribution of the buoyancy sources decides the radial position where convection cells emerge. For example, the flows caused by a homogeneous distribution of heat source are located at mid-depth depth of the shell with the Prandtl number unity, whereas the flows caused by temperature difference across the shell are located where adjacent to the inner sphere at the equator outside the tangent cylinder (Dormy et al. 2004[46]). Although the structures of the flows and the mathematical descriptions with asymptotic theory are investigated for each parameters and conditions (e.g., Jones et al. 2000[47]; Dormy et al. 2004[46]), the physical reasons are not clearly understood.

The understanding of the mechanism for convection is achieved through the budget analysis of the vorticity, heat, and kinetic energy. Hirsching and Yano (1994)[48] investigated the thermal and the vorticity balance of the three types of critical convective flows, which are columnar mode, spiralling mode and wall-attached mode, and distinguished the physics of these morphologies by the differences of the balance. Although they explain the branches of the mode by the analysis, the physical interpretation of each modes could not be investigated.

The physical interpretation for the spiraling mode is investigated by Takehiro (2010)[49]. He showed the kinetic energy balance for a critical spiraling convection driven by internal heating type buoyancy in a thick shell, and then he explained how the balance could be achieved with vorticity budget analysis. The kinetic energy is generated by the buoyancy force most efficiently in the equatorial region, while it is dissipated by viscosity which is distributed at higher latitude. The gap of the position between the generation and the dissipation is bridged by a dynamic energy flux convergence, which results from ageostrophic equatorward flows. However, the balance could change in a case that the inner boundary has

an effect on the onset of convection. One of the aims of this thesis is to clarify the influence of the inner sphere, which could be significant in the Earth ' s core, upon convective flow in a rotating spherical shell.

Whereas the above works consider uniform heat source distribution corresponding to the top-down type buoyancy profile, the main driving force of convection in the Earth's core is believed to be the bottom-up type. Al-shamali et al. (2004)[50] investigated the effect of spherical shell geometry without the internal heat source similar to bottom-up type one. They found a relation between the critical Rayleigh number, Ra_c, and the Ekman number, E_k, as $Ra_c = C(\chi)E_k^{-1.16}$, in which $C(\chi)$ is the coefficient depending on the aspect ratio of the radius at the inner boundary to the radius at the outer boundary, $\chi = R_i/R_o$, for $E_k = 10^{-4}$ to 10^{-3}. The relation is a little different from a relation $Ra_c \propto E_k^{-4/3}$ as $E_k \to 0$ for the homogeneous heat source case (Chandrasekhar, 1961[1]; Roberts, 1968[51]), probably because numerical calculations are carried out with different buoyancy source type and also in a limited range of E_k . Another kind of works for this source case focuses on mathematical description of the onset (e.g. Jones et al. 2000[47]; Dormy et al. (2004)[46]). Dormy et al. (2004)[46] obtained the correct asymptotic relations, considering the boundary layer in the two buoyancy source cases into account. It is, however, more awkward for this case than the homogeneous source case to describe the solution of the governing equations with asymptotic analysis due to a $E_k^{1/3}$ ageostrophic shear layer, which plays a role of reducing the amplitude of convective flows and temperatures to zero, on the inner core tangent cylinder. By this work the mathematical problem about the onset of the linear stability analysis in the core is almost complete for the no internal source case. However, its physical understanding of the difference between the homogeneous and no internal source case have been far from complete.

1.4   Previous works of MHD dynamo

The bottom-up type dynamos as the geodynamo driven by compositional convection have been investigated by many researchers. According to the previous studies (e.g. Nakajima and Kono 1993[52]; Roberts and Schubert 2015[53]), it is found that the kinetic helicity of the velocity field is important not only for in the mean field dynamo but also in the laminar dynamo; for example, Nakajima and Kono (1993)[52] showed that the larger a mean helicity, the more efficient the dynamo becomes.. In fact, correlation between the helicity and dipolarity is apparent in modestly supercritical dynamos (Soderlund et al. 2012[54]), where the dipolarity is defined by the ratio of the power in the dipole component to the total power of the magnetic field on the outer boundary. The dipolarity on the Earth's core-mantle boundary surface up to spherical harmonic degree 12 is 0.68 (Soderlund et al. 2012[54]). The geodynamo is regarded as a dipole-dominant dynamo, considering a dynamo with dipolarity greater than 0.5 to be dipole-dominant.

The dipole-dominant dynamo is often obtained in the bottom-up-type source case. When the dynamo is dipole-dominant at low Rayleigh number, the zonal flows in most cases are generated by thermal wind, which destroys the geostrophic balance of zonal flows, owing to difficulty for the geostrophic zonal flows forced by Reynolds stresses to coexist with the axisymmetric dipole field (Ferraro, 1937[55]). In addition to the source of zonal flows, the dipolarity is decided by the second-order force balance of inertial force versus viscous force. The higher magnitude of the viscous effect than the inertial force makes the dipole-dominant dynamo. For the low Rayleigh number the second-order force, thus, affects magnetic field morphology (Soderlund et al. 2012[54]).

When the Rayleigh number is not low, the dynamo tends to generate multipole-dominant

magnetic fields in the bottom-up-type dynamos (Soderlund et al. 2012[54]; Aubert 2005[26]). According to Aubert (2005)[26], the zonal flows in the multipole-dominant dynamo are generated by both the Reynolds stresses and thermal wind, and more geostrophic than the dipole-dominant cases. At higher Rayleigh number, the convection column in dynamos is destroyed, and an axial helicity becomes much lower than one. The dipole-dominant field in the bottom-up cases requires the columnar convection with high helicity.

The temporal variations of the magnetic fields are investigated in Takahashi (2003)[56]. For differential heating case the flows inside the inner core tangent cylinder has high temporal dependence, although the flows outside it are stable. The zonal toroidal magnetic field outside the tangent cylinder are almost equatorial antisymmetric. Inside the tangent cylinder, the equatorially symmetric toroidal field is often generated, and vanished by intermittent fluctuation of the meridional circulation. The flows inside the tangent cylinder plays a role of generating magnetic fields only when the Rayleigh number is large, generating the magnetic field with the different temporal variation from outside.

Although the bottom-up type convection tends to generate dipole-dominant fields, the top-down type convection has different field morphology. Dynamos generated in the top-down cases with fixed temperature boundaries at low Rayleigh number are mainly divided into three categories: quadrupole-family dynamo, dipole-family dynamo and hemispherical dynamo. Grote et al. (2000)[57] show that the quadrupole-family components are dominant at the magnetic Prandtl number of the order of unity and the Prandtl number equal to 1 with fixed temperature boundary condition. The axisymmetric magnetic fields for the quadrupole-family dynamo oscillate in the direction of high latitude. As increasing P_m, the dipole-family dynamo appears. Hemispherical dynamo is found as the intermediate case, where the magnetic energy is equipartitioned between the dipole-family components and the quadrupole-family components.

It is still in debate what causes the non-dipolar dynamo. Hori et al. (2010)[58] investigated the influence of thermal boundary conditions on dynamos driven by internal heating. Dynamos with fixed temperature boundaries tend to generate multipole fields at $P_m = 3$ and $P_r = 1$, when the Rayleigh number is low. On the other hand, the dipole-dominant dynamo is more easily obtained with fixed flux boundaries. Other studies, however, showed results that dynamos driven by bottom-up convection often result in large dipolaritiy than those by top-down convection, even when other conditions are kept unchanged, with no-slip and fixed heat flux boundaries (e.g., Zhan and Shubert 2012[21]). Thus, both thermal boundary condition and the profile of thermal or chemical flux are important in determining the morphology of the resultant magnetic field.

1.5 Purpose of this study

The primary purpose of this thesis is to understand the basic features of convection and dynamos driven by top-down/bottom-up buoyancy source in a rotating spherical shell. It is important for comprehensive understanding of dynamics and dynamos in the planetary core as well as its evolution history. For this purpose, I carry out the following investigation. Firstly, in chapter 2, I investigate the physical elementary processes of convection in a rotating spherical shell based on linear stability analysis without magnetic field. Because the full, nonlinear problem is too complicated to clearly understand physics, it is reasonable to begin with a simpler problem. Although linear stability analysis is helpful to understand the basic features of core dynamics, mostly treated is thermal convection with internal heating as buoyancy source. This study investigates the onset of the convection for both bottom-up case and top-down case, in order to clarify difference between them, and to understand how

such difference arises. Based on the understanding in chapter 2, results of MHD dynamos are examined in chapter 3. In order to understand the physics of the dynamos for each buoyancy case, the MHD dynamo treats a simpler, low nonlinearity problem; the onset of the dynamo with limitation of equatorial dymmetry is considered. Finally, concluding remarks are summarized in chapter4.

Chapter 2

Critical Compositional Convection with Linear Stability Analysis

2.1 Problem Setup & Method

We consider linear stability analysis of compositional convection driven by both the bottom-up and top-down type buoyancy source without the magnetic fields in a spherical shell rotating at a constant angular velocity, $\vec{\Omega}$, about the z-axis. Although the most linear stability has been used in critical thermal convection, the mathematical problem of the thermal convection is the same as that of the critical compositional convection. Thus, in this chapter, our results are compared with the results of the critical thermal convection in the previous works. The shell with aspect ratio, $\chi = 0.2$ is filled with the Boussinesq fluid, in which it is assumed that the vertical length scale is sufficiently shorter than hydrostatic scale height of pressure, temperature, and density. By using the Boussinesq approximation, we can remove the local sound speed, c_s. The total derivative of the density, $\rho = \rho(S, P)$, is written

$$d\rho = \left(\frac{\partial \rho}{\partial S}\right)_P dS + \left(\frac{\partial \rho}{\partial P}\right)_S dP$$

$$= \left(\frac{\partial C}{\partial S}\right)_P \left(\frac{\partial \rho}{\partial C}\right)_P dS + \left(\frac{\partial \rho}{\partial P}\right)_S dP \tag{2.1}$$

$$\frac{d\rho}{dz} = -\frac{\alpha^\xi \xi \rho}{C_p}\frac{dS}{dz} + \frac{1}{c_s^2}\frac{dP}{dz}, \tag{2.2}$$

where α^ξ, C_p and ξ are the coefficient of chemical expansion, the specific compositional capacity at constant pressure, and the mass fraction. Since c_s is much larger than the speed of the variation in the magnetic and velocity fields in the Boussinesq fluid, the second term on the right hand side of (2.2) is negligible, i.e. the dependency of the density on the pressure is neglected. When the variable is changed from the entropy, S, to the mass fraction, ξ, equation (2.1) is rewritten as

$$d\rho = -\rho_o \alpha d\xi, \tag{2.3}$$

where ρ_o is a constant reference value of the density. This represents the density variation in the Boussinesq fluid. In this thesis, the compositional fluxes at both boundaries are fixed, and the stress-free boundary conditions at both boundaries are used:

$$\frac{\partial \xi}{\partial r} = 0, \qquad u_r = \frac{\partial}{\partial r}\left(\frac{u_\theta}{r}\right) = \frac{\partial}{\partial r}\left(\frac{u_\phi}{r}\right) = 0, \tag{2.4}$$

where u_r, u_θ and u_ϕ is the radial, colatitudinal, and longitudinal, respectively, components of the velocity, $\vec{u}$.

The fluid in the shell is self-gravitating as

$$\vec{g} = -\gamma \vec{r} \,, \tag{2.5}$$

where γ is a constant, and $\vec{r}$ is a position vector with respect to the center of the system. The governing equations are

$$\frac{\partial}{\partial t}\vec{u} + (\vec{u} \cdot \vec{\nabla})\vec{u} + 2\Omega \vec{e_z} \times \vec{u} = -\vec{\nabla}P + \frac{d\rho}{\rho_o}\vec{g} + \nu\nabla^2\vec{u} \tag{2.6}$$

$$\frac{\partial C}{\partial t} + (\vec{u} \cdot \vec{\nabla})C = \kappa^\xi \nabla^2 C + \sigma \tag{2.7}$$

$$\vec{\nabla} \cdot \vec{u} = 0 \,, \tag{2.8}$$

where σ is the rate of heating by source in the fluid. The unknown variables, $\vec{u}$ and C, are divided into two parts: the time-independent, hydrostatic reference state and the deviation. In a non-dimensional form, the governing equations for the perturbations are

$$\frac{\partial}{\partial t}\vec{u} + E_k^{-1}\vec{e_z} \times \vec{u} = Ra\xi\vec{r} - \vec{\nabla}P + \nabla^2\vec{u} \tag{2.9}$$

$$\frac{\partial}{\partial t}\xi + (\vec{u} \cdot \vec{\nabla})\xi_o = S_c^{-1}\nabla^2\xi \tag{2.10}$$

$$\vec{\nabla} \cdot \vec{u} = 0 \,, \tag{2.11}$$

using the thickness of the shell d for the unit of length, the viscous diffusion time d^2/ν for the unit of time, and $-\beta_i d$ and $-\beta_o d$ for the unit of mass fraction in the bottom-up and top-down cases, respectively. Here $\beta_i = (d\xi_o/dr)_{R_i}$ $(\beta_o = (d\xi_o/dr)_{R_o})$ is the total compositional flux at the inner (outer) boundary, where ξ_o is the mass fraction of the basic state, and R_i and R_o are the radius at the inner and outer boundary, respectively. The profiles of the $d\xi_o/dr$ are

$$\frac{d\xi_o}{dr} = -\frac{R_i^2(R_o^3 - r^3)}{r^2(R_o^3 - R_i^3)} \tag{2.12}$$

in the bottom-up buoyancy case, and

$$\frac{d\xi_o}{dr} = -\frac{R_o^2(r^3 - R_i^3)}{r^2(R_o^3 - R_i^3)} \tag{2.13}$$

in the top-down buoyancy case (Appendix Figure 4.1). These equations include three non-dimensional parameters: the Rayleigh number, $Ra = -\beta\alpha^\xi\gamma d^5/\nu^2$, the Ekman number, $E_k = \nu/2\Omega d^2$, and the Schmidt number, $S_c = \nu/\kappa^\xi$. Since the velocity field is the solenoidal, it is represented by using a poloidal scalar U and a toroidal scalar W as the form of

$$\vec{u} = \vec{\nabla} \times (\vec{\nabla} \times U\vec{r}) + \vec{\nabla} \times W\vec{r} \,. \tag{2.14}$$

We multiply the curl and the double curl of the momentum equation by $\vec{r}$, obtaining two equations for U and W:

$$\left[\left(\nabla^2 - \frac{\partial}{\partial t}\right)L_2 + E_k^{-1}\vec{e_z} \times \vec{r} \cdot \vec{\nabla}\right]W - E_k^{-1}QU = 0 \tag{2.15}$$

18

$$\left[\left(\nabla^2 - \frac{\partial}{\partial t} \right) L_2 + E_k^{-1} \vec{e_z} \times \vec{r} \cdot \vec{\nabla} \right] \nabla^2 U + E_k^{-1} QW - Ra L_2 \xi = 0 \;, \qquad (2.16)$$

where L_2 is the angular momentum operator,

$$L_2 = -\frac{1}{\sin\theta} \frac{\partial}{\partial\theta} \left(\sin\theta \frac{\partial}{\partial\theta} \right) - \frac{1}{\sin^2\theta} \frac{\partial^2}{\partial\phi^2} \;,$$

and Q is the form as

$$Q = \vec{e_z} \cdot \vec{\nabla} - \frac{1}{2}(L_2 \vec{e_z} \cdot \vec{\nabla} + \vec{e_z} \cdot \vec{\nabla} L_2) \;.$$

The boundary conditions of (2.4) are rewritten as

$$U = \frac{\partial^2 U}{\partial r^2} = \frac{\partial}{\partial r}\left(\frac{W}{r} \right) = \frac{\partial \xi}{\partial r} = 0 \quad \text{at} \;\; r = \frac{\chi}{1-\chi} \;\; \text{and} \;\; r = \frac{1}{1-\chi} \;. \qquad (2.17)$$

Three unknown scalars, $U(r,\theta,\phi,t), W(r,\theta,\phi,t)$ and $\xi(r,\theta,\phi,t)$, are expanded by spherical harmonics in the angular directions, and varied exponentially with time. Therefore the scalars are

$$U(r,\theta,\phi,t) = \sum_{m,l}^{L} U_l^{mc,s}(r) Y_l^{mc,s}(\theta,\phi) e^{kt}$$

$$W(r,\theta,\phi,t) = \sum_{m,l}^{L} W_l^{mc,s}(r) Y_l^{mc,s}(\theta,\phi) e^{kt}$$

$$\xi(r,\theta,\phi,t) = \sum_{m,l}^{L} \xi_l^{mc,s}(r) Y_l^{mc,s}(\theta,\phi) e^{kt} \;,$$

where k is the complex growth rate of the unknown scalars. In the expansions $Y_l^{mc,s}$ is a spherical harmonics of degree l and order m, which defined as $Y_l^{mc}(\theta,\phi) = P_l^m(\cos\theta) \cos m\phi$ and $Y_l^{ms}(\theta,\phi) = P_l^m(\cos\theta) \sin m\phi$, where P_l^m is the associated Legendre polynomial, and it satisfies the orthogonality relations:

$$\int_0^{2\pi} \int_0^{\pi} Y_{l_1}^{m_1 c,s} Y_{l_2}^{m_2 c,s} \sin\theta d\theta d\phi = \delta_{l_1,l_2} \delta_{m_1,m_2} (1 + \delta_{m_1,0}) \pi$$

$$\int_0^{2\pi} \int_0^{\pi} Y_{l_1}^{m_1 c,s} Y_{l_2}^{m_2 s,c} \sin\theta d\theta d\phi = 0 \;,$$

where δ_{l_1,l_2}, δ_{m_1,m_2} and $\delta_{m_1,0}$ are the Kronecker delta.

Finally, the expansions are substituted into (2.15), (2.16) and (2.10), and then integrating them over the unit sphere after multiplying the equations by $Y_l^{mc,s}$ results in the following equations to be solved numerically:

$$l(l+1)\nabla_l^2 W_l^{mc,s} + E_k^{-1} \left[d_{l+1}^m \left(\frac{\partial}{\partial r} + \frac{l+2}{r} \right) U_{l+1}^{mc,s} + d_l^m \left(\frac{\partial}{\partial r} - \frac{l-1}{r} \right) U_{l-1}^{mc,s} \right]$$
$$\pm E_k^{-1} m W_l^{ms,c} = l(l+1) k W_l^{mc,s} \;, \qquad (2.18)$$

$$l(l+1) Ra \Theta_l^{mc,s} + E_k^{-1} \left[d_{l+1}^m \left(\frac{\partial}{\partial r} + \frac{l+2}{r} \right) W_{l+1}^{mc,s} + d_l^m \left(\frac{\partial}{\partial r} - \frac{l-1}{r} \right) W_{l-1}^{mc,s} \right]$$
$$-l(l+1)\nabla_l^2 \nabla_l^2 U_l^{mc,s} \mp E_k^{-1} m \nabla_l^2 U_l^{ms,c} = -l(l+1) k \nabla_l^2 U_l^{mc,s} \;, \qquad (2.19)$$

19

and

$$\nabla_l^2 \Theta_l^{mc,s} + l(l+1)U_l^{mc,s} = S_c k\Theta_l^{mc,s} \, , \qquad (2.20)$$

where ∇_l^2 is a operation

$$\nabla_l^2 = \frac{\partial^2}{\partial r^2} + \frac{2}{r}\frac{\partial}{\partial r} - \frac{l(l+1)}{r^2} \, ,$$

and d_l^m is defined as

$$d_l^m = (l+1)(l-1)\sqrt{\frac{(l+1)(l-1)}{(2l+1)(2l-1)}} \, .$$

Note that the component of the unknown scalars having an order is not coupled with that having the other orders since the system has no nonlinear effect. The radial derivations in this chapter are approximated by finite differences; by using a second-order central difference, the first and second derivatives of a scalar, $f(r_i)$, are

$$\left.\frac{df}{dr}\right|_{r_i} = -\frac{b}{a(a+b)}f(r_i-a) - \frac{a-b}{ab}f(r_i) + \frac{a}{b(a+b)}f(r_i+b)$$

$$\left.\frac{d^2f}{dr^2}\right|_{r_i} = \frac{2}{a(a+b)}f(r_i-a) - \frac{2}{ab}f(r_i) + \frac{2}{b(a+b)}f(r_i+b) \, ,$$

where $a = r_i - r_{i-1}$ and $b = r_{i+1} - r_i$. However, the viscous term in the equation (2.16) is approximated by the differences with five-point stencil, and the differentiations at the boundaries are calculated by using the ghost grids outside the spherical shell. These equations are solved as eigenvalue problem for k by using the LAPACK. In the above calculation, the onsets of the convection, which have the lowest Rayleigh number in the cases with the zero growth rate, $Re(k) = 0$, when the E_k and the S_c is fixed, are obtained, and then the flows and the composition at the onset are investigated for the bottom-up and top-down type buoyancy cases.

At first, validity of the numerical code that I have developed from scratch is checked by comparison with the previous studies. Table 2.1 shows the reproduced results of critical convection for the same conditions as Al-shamali et al. (2004)[50], Dormy et al. (2004)[46] and Takehiro (2010)[49]. The Schmidt number in our numerical code is set up at the same value of the Prandtl number in the previous works because the mathematical problem in compositional convection is the same as in thermal convection. Although the numerical methods in our study are different from those in three studies, Ra_c in the previous papers and the reproduced Ra_c in our code match in the top two digits. It is confirmed that the reproduction with my numerical code succeeds. In addition to the critical Rayleigh number, the flow pattern and the temperature is reproduced, for example the second case from the top in table 2.1. Figure 2.1 shows the temperature and radial velocity on the equatorial plane, calculated at $E_k = 3 \times 10^{-4}$ with $\chi = 0.25$. Although the solving method is different between the previous work[50] and our study, two results agree not only for the critical Rayleigh number but also for the flow pattern and the temperature. Therefore, our numerical code is confirmed to be correct.

2.2 Results

In previous works (Hirsching and Yano (1994)[48]; Takehiro (2010)[49]), the analysis of vorticity, thermal and kinetic energy have been used in order to understand the physical

Table 2.1: Reproduced results of critical convection for the same conditions as previous works.

paper	B.C.	E_k	χ	Ra_c	m_c	reproduced Ra_c	reproduced m_c	n_r	n_l
A	rigid	10^{-3}	0.35	0.56×10^5	4	0.56×10^5	4	50	31
A	rigid	3×10^{-4}	0.25	2.44×10^5	3	2.42×10^5	3	50	31
A	rigid	10^{-4}	0.15	10.71×10^5	3	10.67×10^5	3	50	31
A	rigid	10^{-4}	0.35	7.00×10^5	7	6.90×10^5	7	50	31
D	free	10^{-5}	0.35	2.1007×10^7	13	2.0956×10^7	13	100	63
D	rigid	10^{-5}	0.35	2.0720×10^7	13	2.0600×10^7	13	100	63
T	free	10^{-5}	0.10	404	19	401	19	80	63

Column 1: the papers in which I have reproduced the onset of the convection here. A, D and T denote the paper of Al-shamali et al. (2004)[50], Dormy et al. (2004)[46] and Takehiro (2010)[49], respectively.; Column 2: boundary condition used in the calculation.; Ra_c and m_c are the critical Rayleigh number and the critical azimuthal wavenumber, respectively , calculated in the previous works.; Reproduced Ra_c and reproduced m_c are the values reproduced with my numerical code.; n_r and n_l is the number of radial grid, and the truncated degree of the spherical harmonics, respectively, in the reproduced calculation.

process of critical convective flows. The critical flows have been investigated mostly in the case of a fluid with a homogeneous heat source distribution, which provides a stationary heat flux of basic state in proportion to the spherical radius. This study investigates other types of convection that has 'bottom-up' type and 'top-down' type buoyancy source, and reveal the differences of the underlying physics.

First, results of linear stability analysis are briefly summarized. Figure 2.2 shows the critical Rayleigh number and the critical azimuthal wavenumber as a function of the E_k^{-1} for the bottom-up case (a) and the top-down case (b). The symbols denote the critical horizontal wavenumbers, and the grey line is produced by fitting the obtained critical Rayleigh number when the E_k is 1.1×10^4 to 2.0×10^4, with the relationship $Ra_c = Co.E_k^j$, where $Co. = 43.07$ and $j = -1.14$ for the bottom-up case, and $Co. = 4.88$ and $j = -1.28$ for the top-down case. It is well known that j becomes $-4/3$ as $E_k \to 0$ due to the analytic solution for the uniform source type convection (Chandrasekhar, 1961[1]; Roberts, 1968[51]), while the obtained relationship for the present results is close to the analytic solution with a slight difference, especially for the bottom-up case. Both the critical Rayleigh number and the critical wavenumber increase as increase in E_k^{-1}. The positive correlation between Ra_c and E_k^{-1} results from the fact that effects of rotation in the spherical system without magnetic field prevents convection from occurring easily.

Spatial structures of the critical convective flows are shown in figure 2.3, calculated at $E_k = 2.0 \times 10^4$ for the bottom-up case in the top, and for the top-down case in the bottom, where the vorticity, ω, is defined as the curl of the velocity, $\omega = \vec{\nabla} \times \vec{u}$. The first column shows (a) the axial component of the vorticity on the equatorial plane. The second, third and fourth columns show (b) the azimuthal-averaged axial helicity, $\int_0^{2\pi} (\vec{e_z} \cdot \vec{u})(\vec{e_z} \cdot \vec{\omega})d\phi$, (c) azimuthal velocity, and (d) flow vector, respectively, on a meridional cross section through a cyclonic convection column. The convection columns for the top-down case are located at the middle of the shell, and for the bottom-up case are adjacent to the inner core tangent cylinder. The difference of the column position could be caused by the profile of buoyancy source, which is the same reason as that between uniform source case and differential heating case (see Dormy et al. (2004)). As we can see in the azimuthal velocity profile, the contour
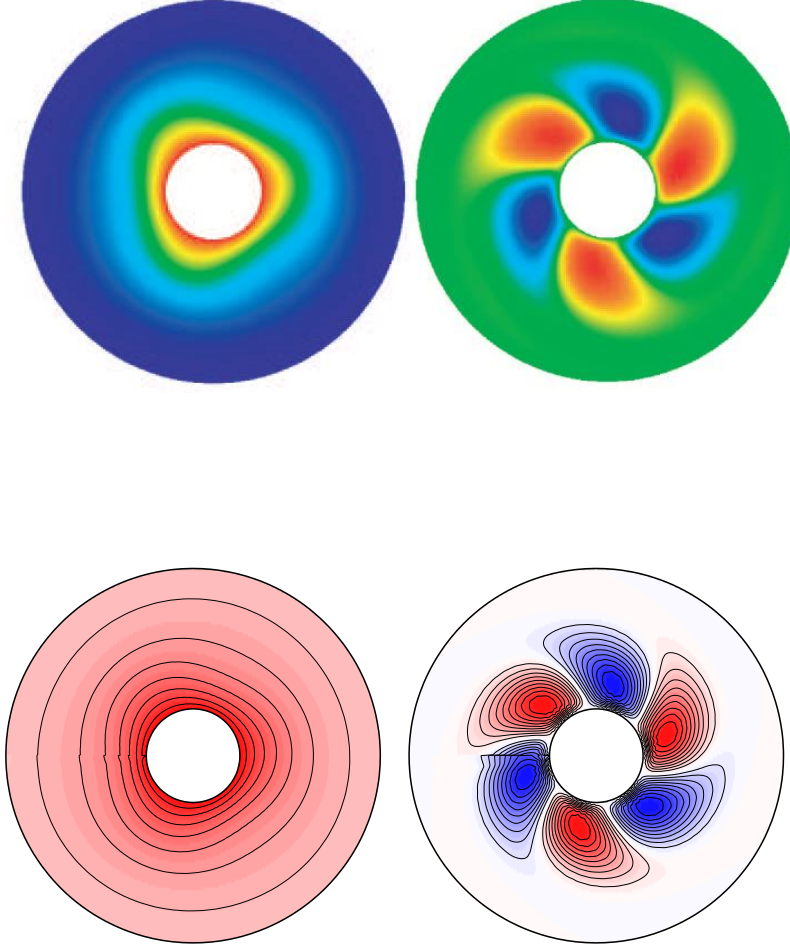
Figure 2.1: Temperature and radial velocity on equatorial plane, calculated for $\chi = 0.25$ in table 2.1. The top and the bottom are the result in Al-shamali et al. (2004) and with my numerical code, respectively. The red (blue) color is high (low) for temperature, or positive (negative) for radial velocity.

lines are parallel to the rotation axis, so the force balance seems to be the quasi-geostrophic one, except for the boundary region. As shown in figure 2.3(d), the flows near the equator penetrate into the inner core tangent cylinder and then move upward or downward along the inner boundary for the bottom-up case, but there is no counterpart for the top-down case.

It is not certain whether the flows inside the tangent cylinder vanishes as $E_k \to 0$, or not.Figure 2.4 shows the contour lines of the radial component of the vorticity on the outer boundary surface, calculated at $E_k^{-1} =$3000, 7000, 8000 and 20000 for the bottom-up buoyancy cases. Although the main vortex tubes in the convection are located at outside of the tangent cylinder, about 70 degrees for all cases, the onsets for $E_k^{-1} = 7000$ and 20000 have the strong vortex tubes inside the tangent cylinder in which convection is not easy to occur. The presence of vortex tubes inside the tangent cylinder relates to the critical azimuthal wavenumber, m_c. The critical azimuthal wavenumbers increase as the Ekman number, E_k, increases for both the top-down and bottom-up cases (Figure 2.2). For the bottom-up cases in Figure 2.2, the onsets of convection have the instability with $m_c = 1$ for $E_k^{-1} = 10^3$ to 2×10^3,
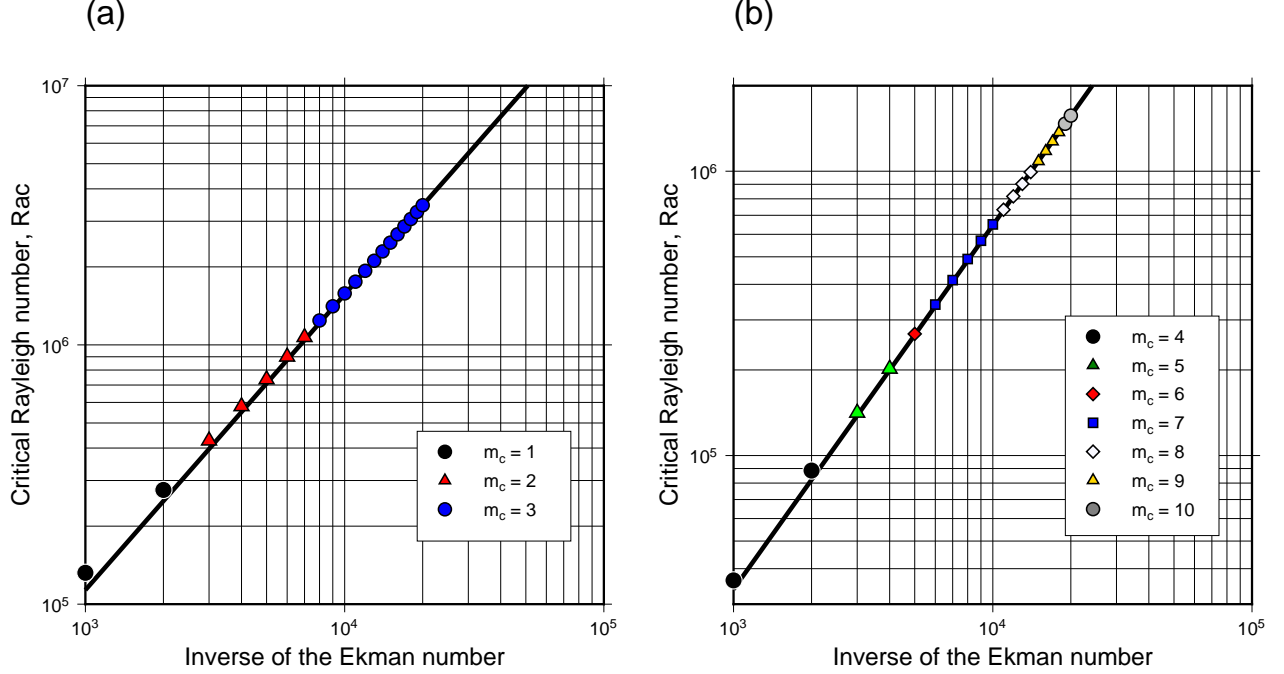
Figure 2.2: The critical Rayleigh numbers, Ra_c, as a function of E_k^{-1} for (a) bottom-up type and (b) top-down type convection. The critical azimuthal wavenumber, is represented by m_c. The Ra_c varies in proportion to $E_k^{-\gamma}$, where $\gamma = 1.14$ for the left and $\gamma = 1.28$ for the right.

$m_c = 2$ for $E_k^{-1} = 3 \times 10^3$ to 7×10^3, and $m_c = 3$ for $E_k^{-1} = 8 \times 10^3$ to 2×10^4. When the Ekman number is the largest in the critical convection with the same m_c, i.e. $E_k^{-1} = 7 \times 10^3$ and 2×10^4, the vortex tubes inside the tangent cylinder are stronger. When the azimuthal wavelength is unchanged even if E_k decreases, the lower E_k increases the Rayleigh number, so that the motion at the low Ekman number has larger viscous effect. The viscous effect tends to transfer the kinetic energy into the tangent cylinder (see the detail later). It is, thus, possible that the flows inside the tangent cylinder exist if $E_k \rightarrow 0$.

The remarkable helicities in figure 2.3(b) for both cases corresponds to the convection columns with negative value in the northern hemisphere and positive values in the southern hemisphere, respectively. The relative axial helicity is often used to see correlation between the axial components of the velocity and vorticity,

$$H_z^{rel} = \frac{< u_z \omega_z >_h}{(< u_z u_z >_h < \omega_z \omega_z >_h)^{1/2}} \, ,$$

where $<>_h$ is the volumetric average in a hemisphere excluding boundary layer (e.g. Olson et al. (1999)[45]; Schmitz and Tilgner (2010)[59]). We write the axial helicity magnitude averaged over both hemispheres, $|H_z^{rel}|$ (Soderlund et al. 2012[54]). The figure 2.5 shows the relative axial helicity versus the E_k^{-1} for bottom-up case (solid circles) and the top-down
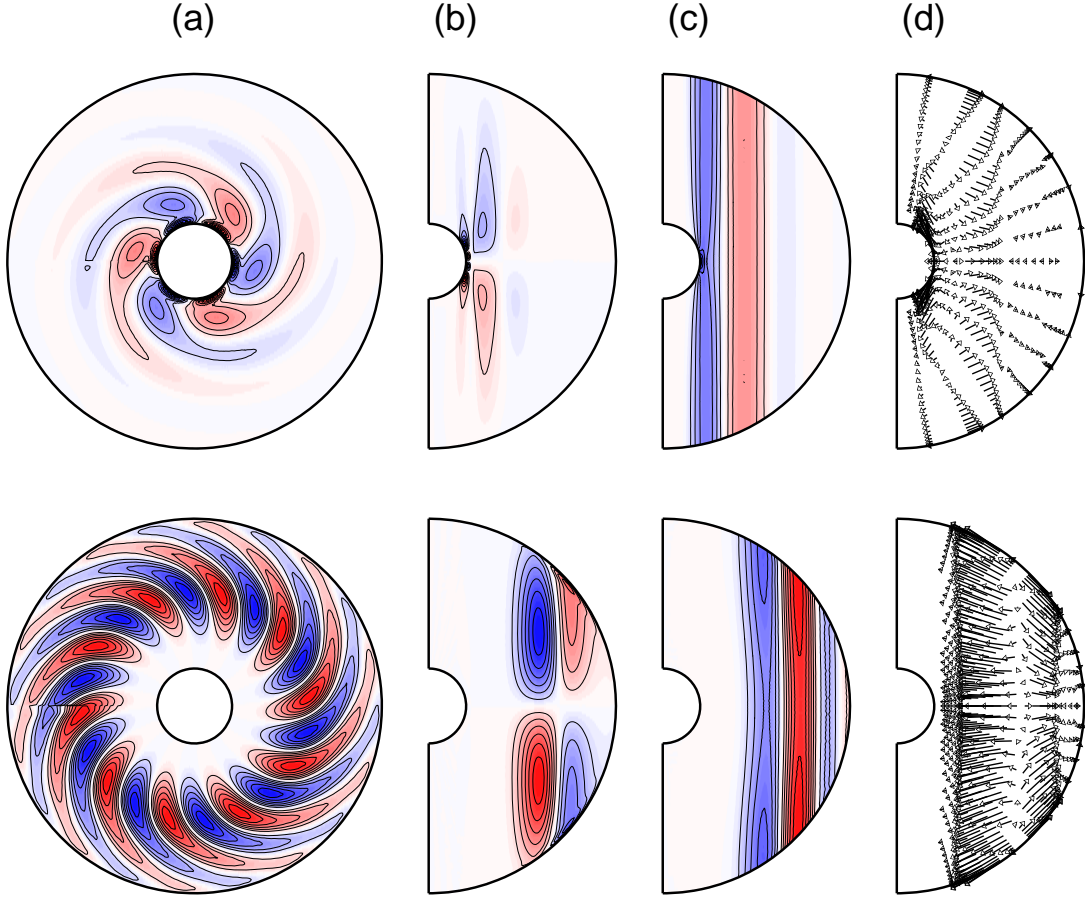
Figure 2.3: Flow patterns for the bottom-up case in the top and for the top-down case in the bottom, calculated at $E_k = 5 \times 10^{-5}$. (a) The axial vorticity in the equatorial plane; (b) the axial helicity; (c) the azimuthal component of the velocity; (d) the flow vector. (b)-(d) are drawn in a meridional cross section through the middle of a cyclonic convection column.

case (open circles). The helicity in the bottom-up case is higher than that in the top-down case. The lower helicity in the top-down cases is caused by the presence of the helicity with opposite sign to the helicity of the columnar convection in the hemisphere (see Figure 2.3(b)). For mean field theorem, helicities strengthen α effect; according to Moffatt (1978)[35], the strength of the $\alpha-$effect is proportional to a helicity. The $\alpha-$effect is thought to be necessary for generating large-scale magnetic field (e.g. Parker, 1955[41]; Moffatt, 1978[35]). It could be expected that the bottom-up type dynamo is easier to achieve the successful dynamos with the large-scale magnetic field than the top-down type dynamo.

Kinetic energy budget analysis was used in this study to understand the physical process of the critical convective flows, and the our results are compared with those in a previous work which investigated the kinetic energy budget in a uniform heating source case (Takehiro, 2010[49]). The kinetic energy transfer equation

$$\frac{\partial}{\partial t}\left(\frac{1}{2}\vec{u}\cdot\vec{u}\right) = Ra\xi\vec{r}\cdot\vec{u} - \vec{\nabla}\cdot(P\vec{u}) - D_k - \vec{\nabla}\cdot\vec{\Phi} \qquad (2.21)$$

is derived by multiplying the momentum equation by $\vec{u}\cdot$, where Φ is the viscous energy
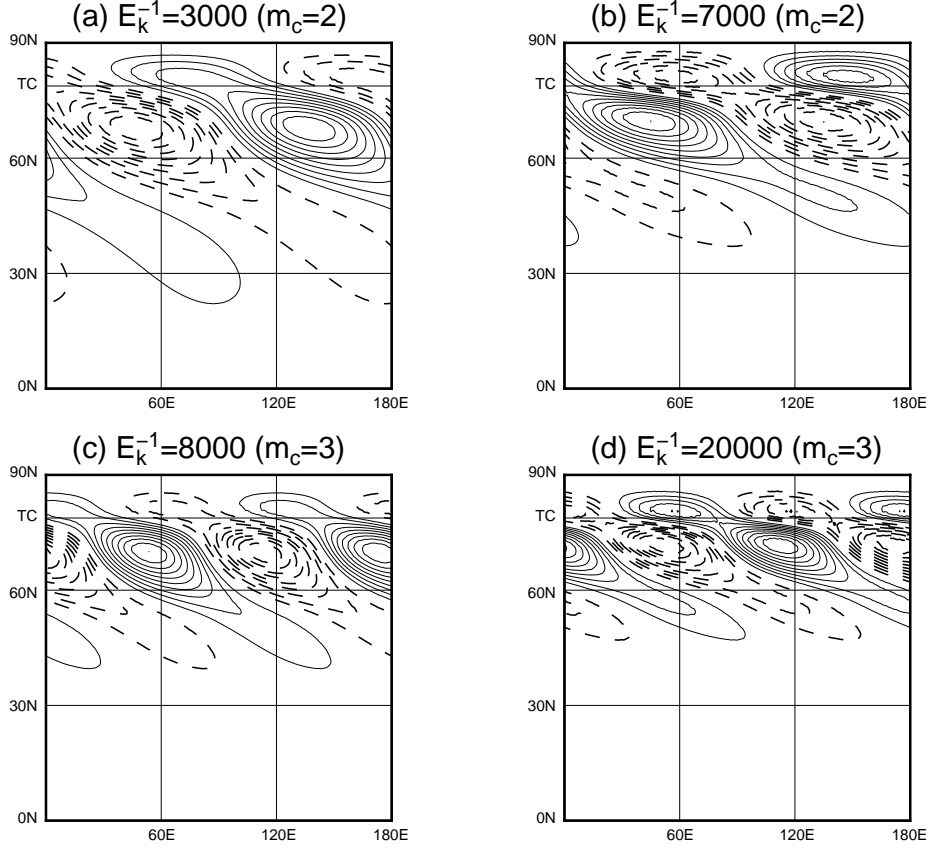
Figure 2.4: Contour lines of the radial component of the vorticity on the outer boundary surface, calculated at E_k^{-1} =3000 (a), 7000 (b), 8000 (c) and 20000 (d) for the bottom-up buoyancy cases. The vertical axis is latitude from 0 to 90 degrees; the horizontal axis is longitude from 0 to 180 degrees. TC in the vertical axis indicates the latitude, about 78.8 degrees, corresponding to the limb of inner core tangent cylinder.

transfer,

$$\Phi_i = -\sum_j \sigma_{ij} u_j \,,$$

and D_k is the viscous dissipation,

$$D_k = \frac{1}{2} \sum_{i,j} \sigma_{ij}^2 \,.$$

σ_{ij} is the viscous stress tensor in the spherical coordinate, whose expressions are given in Landau and Lifshitz (1987)[60]. In the cylindrical coordinate system, (s, ϕ, z), the components of the stress tensor are

$$\sigma_{ss} = 2\frac{\partial u_s}{\partial s}, \qquad \sigma_{s\phi} = \frac{1}{s}\frac{\partial u_s}{\partial \phi} + \frac{\partial u_\phi}{\partial s} - \frac{u_\phi}{s}$$

$$\sigma_{\phi\phi} = 2\left(\frac{1}{s}\frac{\partial u_\phi}{\partial \phi} + \frac{u_s}{s}\right), \qquad \sigma_{\phi z} = \frac{\partial u_\phi}{\partial z} + \frac{1}{s}\frac{\partial u_z}{\partial \phi}$$

$$\sigma_{zz} = 2\frac{\partial u_z}{\partial z}, \qquad \sigma_{zs} = \frac{\partial u_z}{\partial s} + \frac{\partial u_s}{\partial z} \,.$$
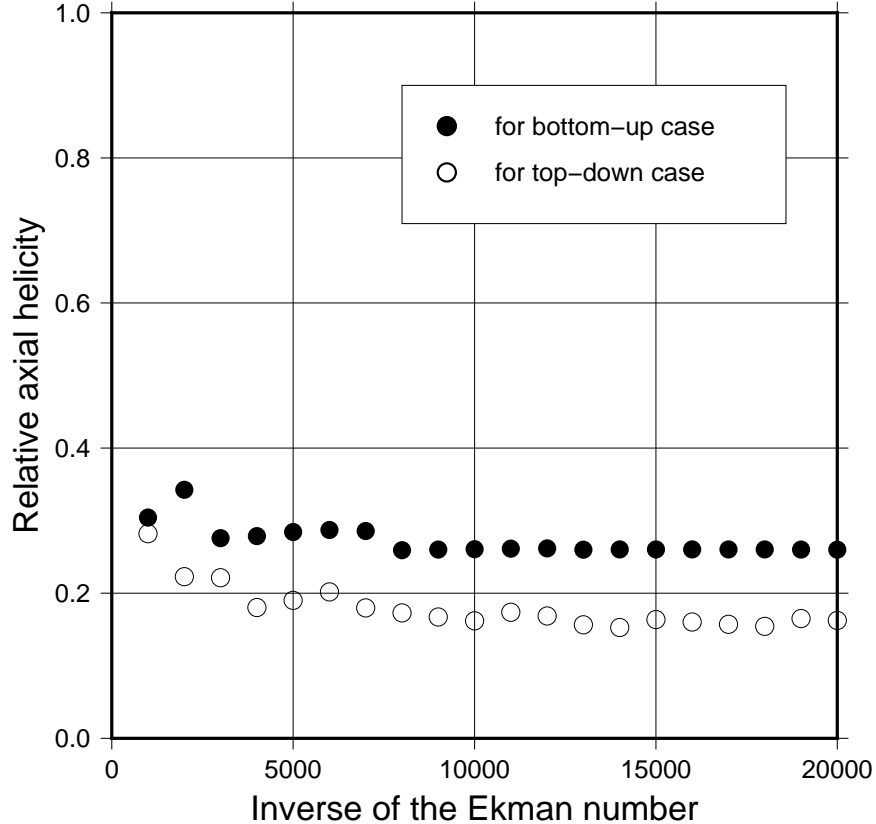
Figure 2.5: Relative axial helicity as a function of the inverse of the Ekman number for the bottom-up case and the top-down case. The solid (open) circles show the helicities for the bottom-up (top-down) case.

In the transfer equation the left-hand-side shows temporal change of the kinetic energy, and the right-hand-side show the generation of the energy due to the buoyancy force, the dynamic energy flux convergence caused by the pressure gradient force, the viscous dissipation and the viscous energy flux convergence from the left to right. The figure 2.6 illustrates the meridional distribution of the azimuthally averaged terms of the right-hand side of the kinetic energy equation (2.21) at $E_k^{-1} = 2 \times 10^4$ for (a) the bottom-up convection and (b) the top-down convection. In the bottom-up case generation of the kinetic energy is located adjacent to, and outside, the tangent cylinder. The kinetic energy in the top-down type convection at onset is generated at the middle cylindrically-radius of the shell, especially on the equatorial plane. The viscous dissipation has different patterns in each cases. Significant dissipation occurs around the inner and the outer edges of the convection columns aligned to the rotation axis in the bottom-up case. In addition, the strongest dissipation is found around the top and the bottom edges of the convection columns in the top-down case. As seen in Takehiro (2010)[49], the distribution of the generation term for a uniform source type convection is apart from the tangent cylinder, and that of the viscous dissipation term is at the same cylindrical-radius as the generation term but around the top and the bottom of the convection column (the detail is described in Takehiro 2010[49]). The kinetic energy is dissipated in the top-down case and the uniform source type case differently from that in the bottom-up case. The profile of the viscous dissipation in the bottom-up case is different from that in the top-down case.

The kinetic energy generated by the buoyancy force is transferred to the region of strong
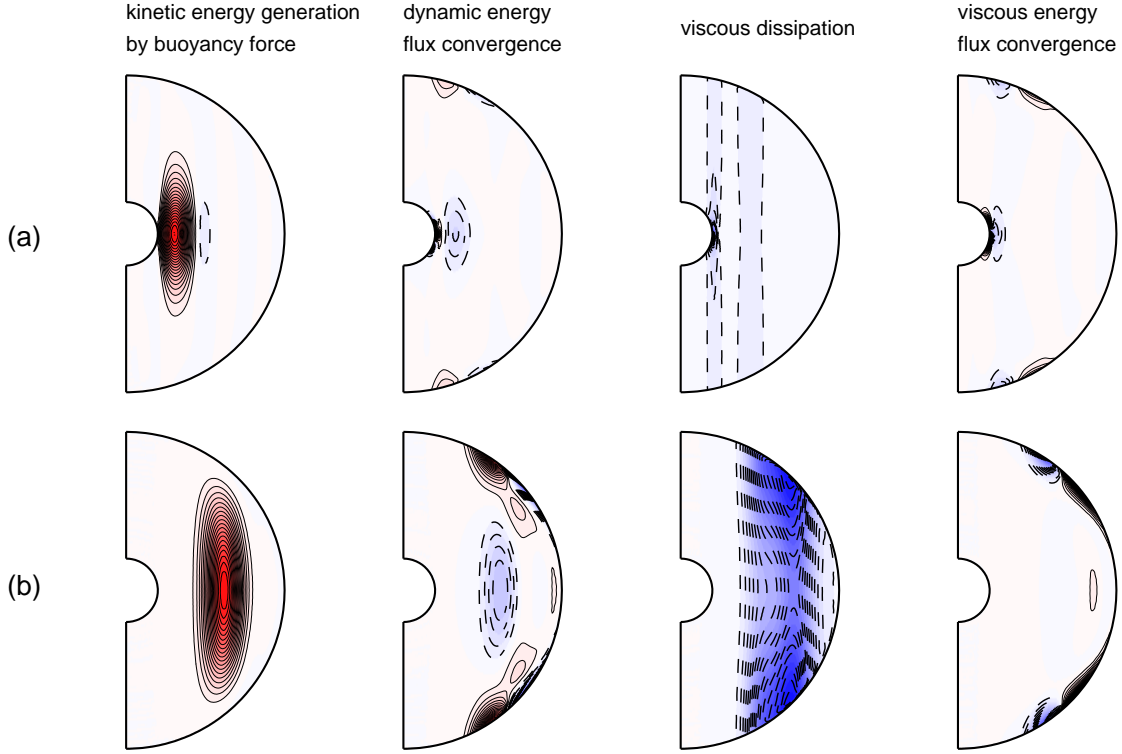
Figure 2.6: Azimuthally averaged terms on the right hand side of the kinetic energy transfer equation (2.21), calculated at $E_k = 5 \times 10^{-5}$, and normalized by the maximum value in each terms. (a) The distributions for the bottom-up case. (b) The distributions for the top-down case. The each figures from the left column are corresponding to the terms on the right hand side of the kinetic energy equation from left to right.

viscous dissipation by the dynamic energy flux convergence in a uniform heat source case (Takehiro (2010)[49]). The dynamic energy flux convergence in the present top-down cases plays the same role as in the previous work, because negative contribution in the convection region, and positive contribution in the top and bottom edges are observed (Figure 2.6 (a)). It is also confirmed that dynamic energy flux convergence term plays a similar role in the bottom-up cases. Figure 2.7 shows cylindrically radial distribution of the axially and zonally averaged terms of the kinetic energy equation. According to figure 2.7(a), the kinetic energy generated in the convection is dissipated strongly at the inner and outer edges of the convection column, especially at the inner one on the tangent cylinder.For the inner edge the energy is transferred from the convection column to the tangent cylinder by the dynamic energy flux convergence, and from the tangent cylinder to the interior of the cylinder by the viscous energy flux convergence.The viscous energy flux convergence is important for the balance of the kinetic energy budget for the bottom-up case.

Then, the viscous dissipation term is decomposed into individual contributions to analyze in detail. Although the distribution of the viscous dissipation in the bottom-up case is different from that in the top-down case, the same viscous stress tensors contribute the profile of the dissipation. Figure 2.8 shows th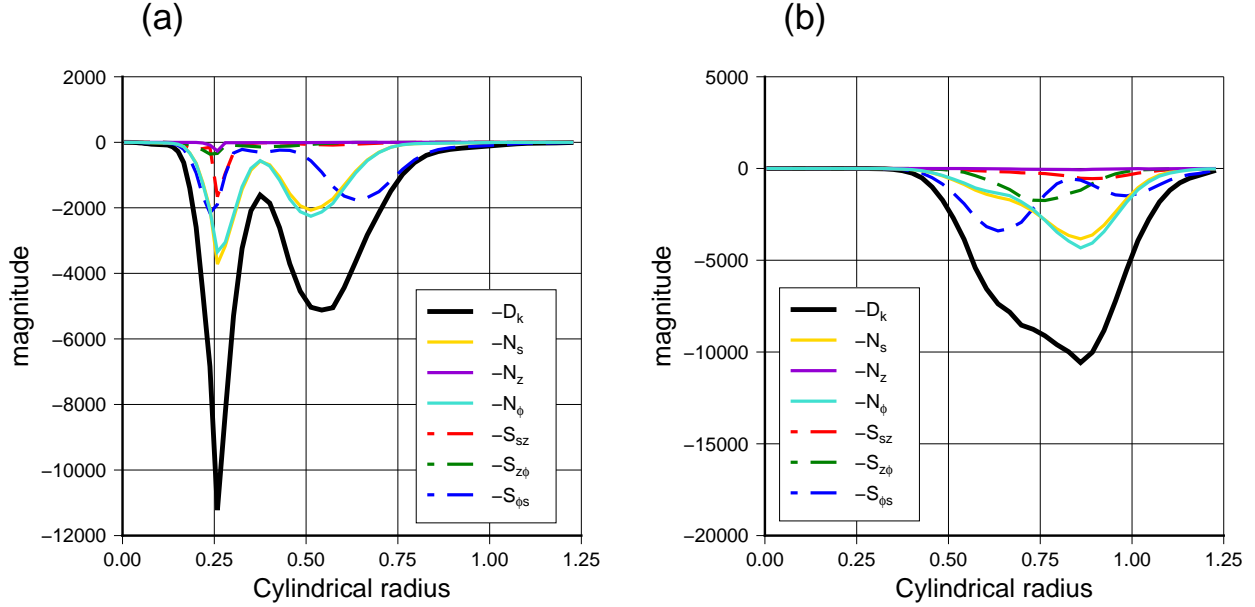e cylindrically radial distributions of the viscous dissipation and the six constituents of the viscous dissipation, averaged over the cylindrical
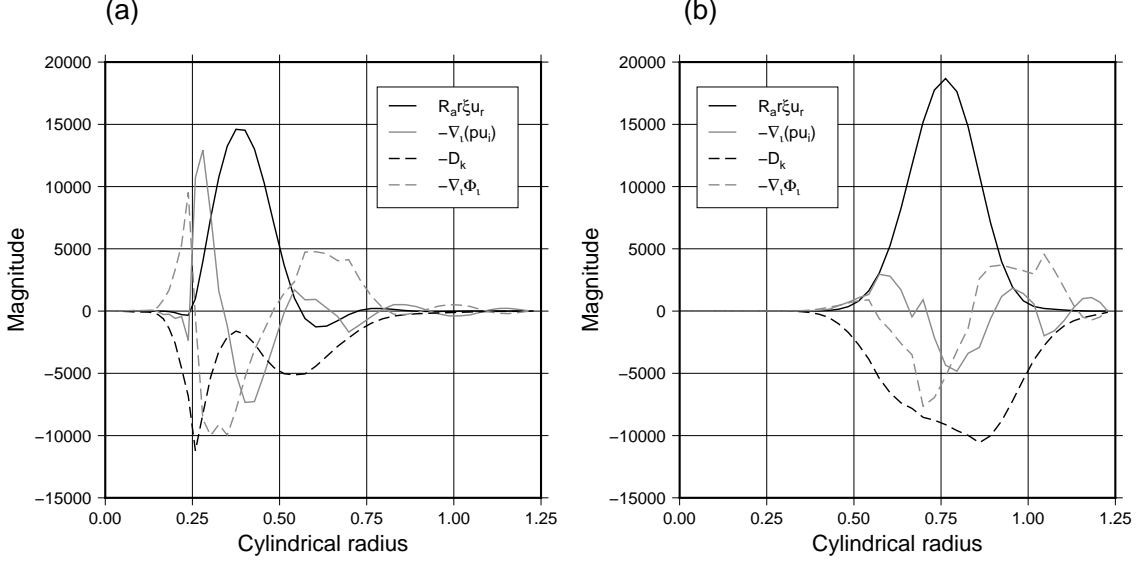
Figure 2.7: Cylindrical radial distributions of the axially and zonally averaged terms of the kinetic energy equation, calculated at $E_k = 5 \times 10^{-5}$. (a) The distributions for the bottom-up case. (b) The distributions for the top-down case. Black solid line: generation term of kinetic energy by buoyancy force; grey solid line: term of dynamic energy flux convergence; black broken line: viscous dissipation term; grey broken line: term of viscous energy flux convergence.

surfaces. The six constituents in this section are defined as

$$
\begin{aligned}
-D_k &= -\tfrac{1}{2}\sigma_{ss}^2 \quad -\tfrac{1}{2}\sigma_{zz}^2 \quad -\tfrac{1}{2}\sigma_{\phi\phi}^2 \quad -\tfrac{1}{2}(\sigma_{sz}^2 + \sigma_{zs}^2) \quad -\tfrac{1}{2}(\sigma_{z\phi}^2 + \sigma_{\phi z}^2) \quad -\tfrac{1}{2}(\sigma_{s\phi}^2 + \sigma_{\phi s}^2) \\
&\equiv -N_s \quad\quad -N_z \quad\quad -N_\phi \quad\quad\quad -S_{sz} \quad\quad\quad\quad\quad -S_{z\phi} \quad\quad\quad\quad\quad -S_{\phi s} \; .
\end{aligned}
$$

In both cases the viscous dissipation related to the normal stress tensors in the cylindrically-radial and azimuthal direction, N_s and N_ϕ, mainly form the distribution of the total viscous dissipation. The less dominance of N_z implies that the ageostrophic balance in the boundary layer does not affect the viscous normal stresses, although the boundary layers destroy the quasi-geostrophic balance. Because the critical convection in the bottom-up case is strongly generated near the inner boundary on the low latitude, the system needs to make N_s stronger on the inner boundary layer. The large magnitide of N_s require the equivalent one of N_ϕ owing to the mass conservation (2.11). In contrast, the top-down-type critical convection separates the profile of the kinetic energy generation with the outer boundary touching the convection column. The viscous dissipation in the top-down cases has influence of the secondary flows in the convection column rather than the boundary layers. It seems that the distribution of the viscous dissipation is attributed to the effect of the boundaries.

Further, viewed from another point, the viscous dissipation inside vorticity structure in the bottom-up case is divided to the inner and outer edges of the structure by an energy

Figure 2.8: Cylindrically radial distributions of the viscous dissipation and the six constituents of the viscous dissipation, averaged over the cylindrical surfaces, calculated at $E_k = 5 \times 10^{-5}$ in the bottom-up case (a) and the top-down case (b). The gold, violet and turquoise lines are the distributions of the normal stress represented as N_s, N_z and N_ϕ, respectively. The red, green and blue lines are the distributions of the shear stresses represented as S_{sz}, $S_{z\phi}$ and $S_{\phi s}$, respectively.

convergence. The representation of viscous dissipation, D_k, is separated into two terms as

$$-D_k = -\vec{\omega} \cdot \vec{\omega} - 2\vec{\nabla} \cdot \left[(\vec{u} \cdot \vec{\nabla}) \vec{u} \right]$$
$$= -\omega^2 + D_A .$$

The first term on the right hand is kinetic energy reduction due to vorticity, and the second term is advective energy flux convergence. The kinetic energy is dissipated by the vorticity in the column convection, and then the energy is transferred from the convection column to the inner and outer edges, more especially in the bottom-up case.

It is not certain that the viscous effect is vanished as decreasing with E_k. Figure 2.10 shows the cylindrically radial distributions of the viscous dissipation for five cases of the Ekman number. The magnitude of the viscous dissipation at two strong points, which is the inner edge and the outer edge of the convection, increase with the Ekman number decreasing. Thus, this kinetic energy balance could be important if $E_k \to 0$.

2.3   Discussion

The onsets of the convection in the bottom-up buoyancy cases and the top-down buoyancy cases have been investigated in the previous section in order to discover differences between the two cases, and to understand its mechanisms. The differences in terms of the main convection structure and the numerical problem have be clarified; the flow pattern in the internal heating case like the top-down type and in the differential heating case like the bottom-up type is located at the mid-depth of the shell, and adjacent (but exterior) to the tangent cylinder, respectively ; according to the correct asymptotic theory (Dormy et al.

29
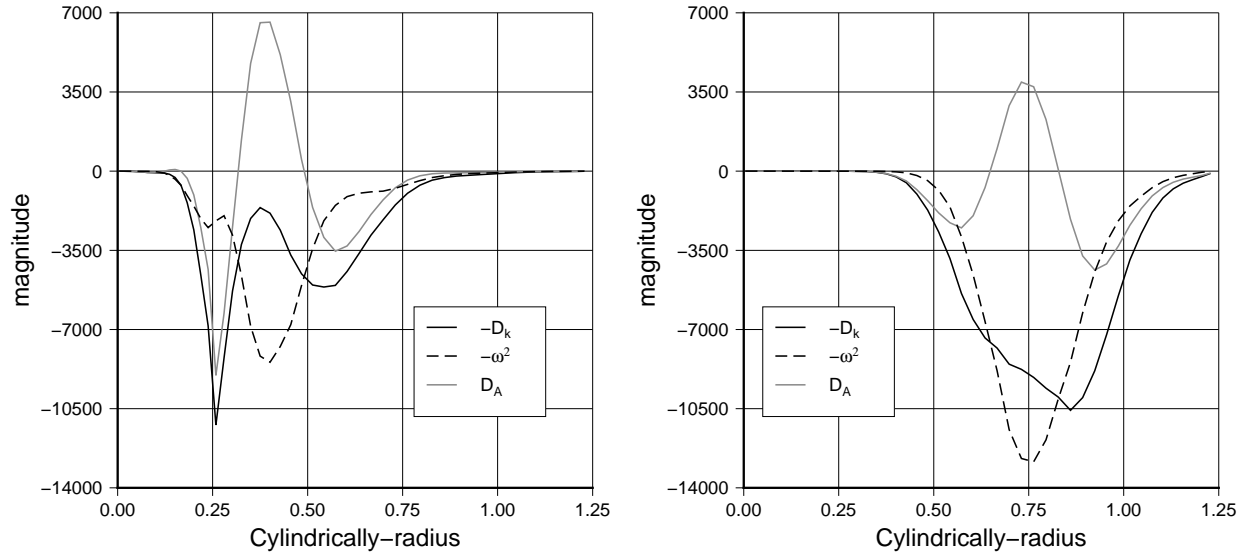
Figure 2.9: Cylindrically radial distributions of the viscous dissipation, and two constituents, averaged over the cylindrical surfaces. Thick solid line is viscous dissipation. Broken line (thin solid line) is the viscous dissipation by vorticity structure (advective energy flux convergence).
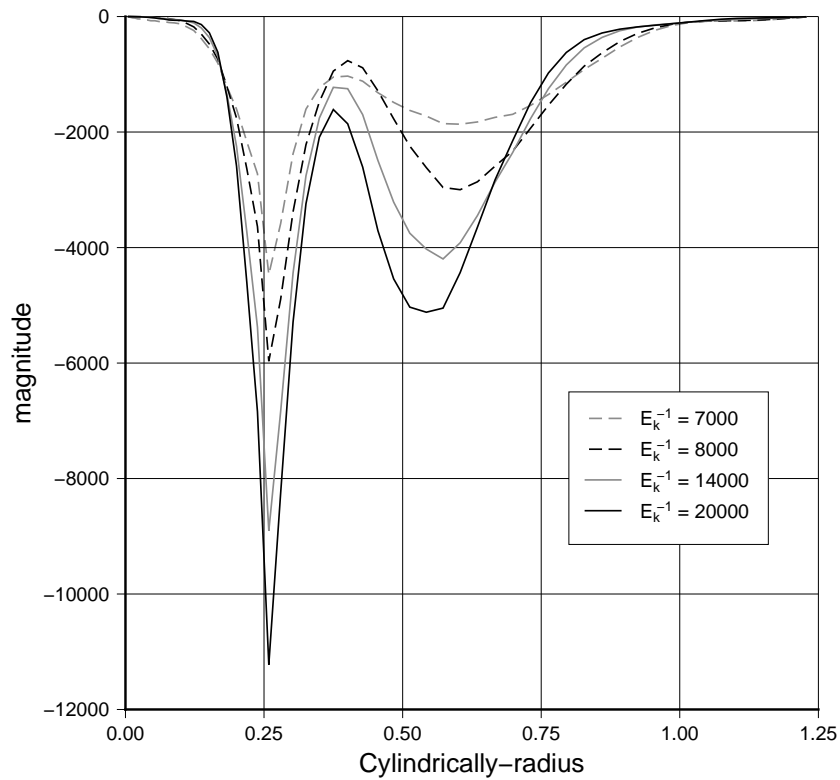
Figure 2.10: The cylindrically radial distributions of the viscous dissipation for five cases of the Ekman number: $E_k^{-1} = 7000$, 8000, 14000 and 20000.

2004[46]), the numerical description for the differential heating case needs to include the effect of an ageostrophic shear layer on the tangent cylinder. In this paper the purpose is to clarify the physical reasons why the difference arises by the different buoyancy cases.

The decrement of the critical Rayleigh number with the Ekman number is slightly smaller in the bottom-up case than that calculated by a local analysis at $E_k \to 0$ (e.g. Chandrasekhar, 1961[1]; Roberts, 1968[51]). The same result was obtained in Al-shamali et al. (2004)[50], and they found that the critical Rayleigh number varies in proportion to $E_k^{-1.16}$, although they concluded that the reason is that the calculation was not set up at $E_k \to 0$. One of possible reasons is E_k adopted in the present study is not small enough to be in the asymptotic limit. In addition, the local analysis has not considered the influence of the inner boundary on convection. In the bottom-up cases the effect is not negligible because the flows outside the convection columns play the important role of balancing kinetic energy budget. Therefore, it is not necessary that the present calculations yields the same results as those based on local analysis.

A previous work (Dormy et al. 2004[46]) treats the ageostrophic shear layer on the inner boundary as the one playing the role in vanishing the amplitude of the velocities. Because the role leads to increasing the viscous dissipation in the layer, the distribution of the dissipation in this results could be similar to that in the previous work. However, the onsets of the bottom-up type convection in this study have the additional flows through the tangent cylinder, and the flows help the viscous dissipation. The ageostrophic shear layer plays role of strengthening the dissipation rather than vanishing the amplitude.

The reason why the the flows through the inner core tangent cylinder around the inner boundary are formed in the bottom-up cases is probably as follows. Because the convection column generally tends to have axisymmetric structure about the center axis of the convection column, the convective flows around the tangential points to the inner core have little flux in the azimuthal direction, but strong flux in the radial direction. The radial influx or outflux needs to flow in the latitude or rotation-axis direction around the inner boundary because the fluid at any point satisfies the continuity equations (2.11). The strong mass flux makes the viscous dissipation in the ageostrophic layer more effectively (see Figure 2.7(a)) since $\vec{\nabla} \cdot \vec{u} = \sigma_{ss} + \sigma_{\phi\phi} + \sigma_{zz} = 0$.

Although our calculations of the critical convection are in linear problem, the mass conservation must be satisfied also in the MHD dynamo, if the fluid is still considered as the Boussinesq one. For MHD numerical dynamos driven by bottom-up buoyancy, the magnetic and velocity fields inside the inner core tangent cylinder often have different features from outside (e.g. Takahashi et al. 2003[56]; Aubert, 2005[26]) ; for example, the multipolar dynamos driven by the bottom-up cases has the zonal flows by thermal wind inside the tangent cylinder, but by the Reynolds stress outside (Aubert, 2005[26]). Although generating the convection in the interior of the tangent cylinder is more difficult than the exterior, the flows inside the tangent cylinder might exist, and have the different strucure from that outside. It is possible that the position of the convection adjacent to the tangent cylinder in bottom-up type produces the influx and outflux through the cylinder, and their flows could affect the planetary core dynamics inside the tangent cylinder.

Chapter 3

MHD Dynamo in a Rotating Spherical Shell

3.1 Problem Setup & Method

MHD dynamo simulations are performed by the code based on Takahashi (2012)[61]. In the similar system to the previous chapter we consider the dynamos driven by compositional convection in a rotating spherical shell. The Boussinesq fluid in the shell shall has a finite electrical conductivity in this chapter. By using the thickness of the shell d for the unit of length, the viscous diffusion time d^2 / ν for the unit of the time, $(2\rho\mu\eta\Omega)^{1/2}$ for the unit of the magnetic field, and $-\beta_i d$ and $-\beta_o d$ for the unit of mass fraction in the bottom-up case and the top-down case, respectively, the non-dimensional equations are

$$E_k \left[\frac{\partial \vec{u}}{\partial t} + (\vec{u} \cdot \vec{\nabla})\vec{u} - \nabla^2 \vec{u} \right] = \vec{u} \times \vec{e_z} - \vec{\nabla}P + RS_c^{-1}\xi \frac{\vec{r}}{R_o} + \frac{1}{P_m}(\vec{\nabla} \times \vec{B}) \times \vec{B} \tag{3.1}$$

$$\frac{\partial \vec{B}}{\partial t} = \frac{1}{P_m}\nabla^2 \vec{B} + \vec{\nabla} \times (\vec{u} \times \vec{B}) \tag{3.2}$$

$$\frac{\partial}{\partial t}(\xi_o + \xi) + (\vec{u} \cdot \vec{\nabla})(\xi_o + \xi) = \frac{1}{S_c}\nabla^2(\xi_o + \xi) \tag{3.3}$$

$$\vec{\nabla} \cdot \vec{u} = 0 \tag{3.4}$$

$$\vec{\nabla} \cdot \vec{B} = 0 \,, \tag{3.5}$$

where the gravitational acceleration is assumed as $\vec{g} = -g_o \vec{r}/R_o$ in this section. These equations have four non-dimensional parameter: the modified Rayleigh number $R = -\alpha^\xi g_o \beta d^2 / 2\Omega\kappa^\xi (= RaE_k S_c)$, the Ekman number $E_k = \nu/2\Omega d^2$, the magnetic Prandtl number $P_m = \nu/\eta$, and the Schmidt number $S_c = \nu/\kappa^\xi$. In this study, the parameter is set up at $E_k = 10^{-4}$, $P_m = 3$ and $Sc = 1$. The profiles of the $d\xi_o/dr$ are the same as the previous chapter. The unknown vectors, $\vec{u}$ and $\vec{B}$, are expanded to the form as

$$\vec{u} = \vec{\nabla} \times (\vec{\nabla} \times U_p \vec{e_r}) + \vec{\nabla} \times W_t \vec{e_r} \tag{3.6}$$

$$\vec{B} = \vec{\nabla} \times (\vec{\nabla} \times S_p \vec{e_r}) + \vec{\nabla} \times T_t \vec{e_r} \,, \tag{3.7}$$

where U_p and W_t are the poloidal and toroidal, respectively, scalars of $\vec{u}$, S_p and T_t are the poloidal and toroidal, respectively, scalars of $\vec{B}$ in this section.

We multiply the double curl and the curl of the momentum equation, and the induction equation and the curl of the induction equation by $\vec{e_r}$, obtaining four equations for U_p, W_t, S_p and T_t:

$$\frac{E_k}{r^2}\left[\frac{\partial}{\partial t} - \nabla_s^2\right]L_2\nabla_s^2 U_p = -\vec{e_r}\cdot\vec{\nabla}\times\vec{\nabla}\times\vec{M} \tag{3.8}$$

$$\frac{E_k}{r^2}\left[\frac{\partial}{\partial t} - \nabla_s^2\right]L_2 W_t = \vec{e_r}\cdot\vec{\nabla}\times\vec{M} \tag{3.9}$$

$$\frac{1}{r^2}\left[\frac{\partial}{\partial t} - \frac{1}{P_m}\nabla_s^2\right]L_2 S_p = \vec{e_r}\cdot[\vec{\nabla}\times(\vec{u}\times\vec{B})] \tag{3.10}$$

$$\frac{1}{r^2}\left[\frac{\partial}{\partial t} - \frac{1}{P_m}\nabla_s^2\right]L_2 T_t = \vec{e_r}\cdot[\vec{\nabla}\times\vec{\nabla}\times(\vec{u}\times\vec{B})]\ , \tag{3.11}$$

where

$$\nabla_s^2 = \frac{\partial^2}{\partial r^2} - \frac{L_2}{r^2}\ ,$$

and

$$\vec{M} = -(\vec{u}\cdot\vec{\nabla})\vec{u} + \vec{u}\times\vec{e_z} + RS_c^{-1}\xi\frac{\vec{r}}{R_o} + \frac{1}{P_m}(\vec{\nabla}\times\vec{B})\times\vec{B}\ .$$

The shell is electrically insulating with stress-free boundaries, and chemical flux is fixed at the both boundaries:

$$U_p = \frac{\partial}{\partial r}\left(\frac{1}{r^2}\frac{\partial U_p}{\partial r}\right) = \frac{\partial}{\partial r}\left(\frac{W_t}{r^2}\right) = \frac{\partial \xi}{\partial r} = T_t = 0 \quad at\ \ r = \frac{\chi}{1-\chi}\ \ and\ \ r = \frac{1}{1-\chi}\ . \tag{3.12}$$

The unknown scalars are expanded by the spherical harmonics that is introduced in the previous chapter;

$$U_p(r,\theta,\phi,t) = \sum_{m,l}^{L} U_{p,l}^{mc,s}(r,t)Y_l^{mc,s}(\theta,\phi)$$

$$W_t(r,\theta,\phi,t) = \sum_{m,l}^{L} W_{t,l}^{mc,s}(r,t)Y_l^{mc,s}(\theta,\phi)$$

$$S_p(r,\theta,\phi,t) = \sum_{m,l}^{L} S_{p,l}^{mc,s}(r,t)Y_l^{mc,s}(\theta,\phi)$$

$$T_t(r,\theta,\phi,t) = \sum_{m,l}^{L} T_{t,l}^{mc,s}(r,t)Y_l^{mc,s}(\theta,\phi)$$

By multiplying the equations (3.8), (3.9), (3.10) and (3.11) by $Y_l^{mc,s}$, and integrating them over a spherical surface, equations for the unkown scalars are derived as forms of

$$E_k n_m\frac{l(l+1)}{r^2}\left[\frac{\partial}{\partial t} - \nabla_s^2\right]\nabla_s^2 U_{p,l}^{mc,s} = -\int_S Y_{l'}^{m'c,s}\vec{e_r}\cdot\vec{\nabla}\times\vec{\nabla}\times\vec{M}dS \tag{3.13}$$

$$E_k n_m\frac{l(l+1)}{r^2}\left[\frac{\partial}{\partial t} - \nabla_s^2\right]W_{t,l}^{mc,s} = \int_S Y_{l'}^{m'c,s}\vec{e_r}\cdot\vec{\nabla}\times\vec{M}dS \tag{3.14}$$

33

$$n_m \frac{l(l+1)}{r^2} \left[\frac{\partial}{\partial t} - \frac{1}{P_m} \nabla_s^2 \right] S_{p,l}^{mc,s} = \int_S Y_{l'}^{m'c,s} \vec{e_r} \cdot [\vec{\nabla} \times (\vec{u} \times \vec{B})] dS \tag{3.15}$$

$$n_m \frac{l(l+1)}{r^2} \left[\frac{\partial}{\partial t} - \frac{1}{P_m} \nabla_s^2 \right] T_{t,l}^{m'c,s} = \int_S Y_{l'}^{m'c,s} \vec{e_r} \cdot [\vec{\nabla} \times \vec{\nabla} \times (\vec{u} \times \vec{B})] dS . \tag{3.16}$$

The poloidal magnetic field needs to be connected with the exterior potential fields at the boundaries as

$$\left(\frac{\partial}{\partial r} - \frac{l+1}{r} \right) S_{p,l}^{mc,s} = 0 \quad at \ r = R_i \tag{3.17}$$

$$\left(\frac{\partial}{\partial r} + \frac{l}{r} \right) S_{p,l}^{mc,s} = 0 \quad at \ r = R_o . \tag{3.18}$$

The Crank-Nicolson scheme for the diffusion terms, and the 3rd-order Adams-family predictor-corrector scheme for the others are used to time-integrate the equations (3.13), (3.14), (3.15) and (3.16). As the initial conditions in this time-integration, the obtained critical convection in Chapter 2, calculated at $E_k = 10^{-4}$ in the top-down and bottom-up cases, and axisymmetric dipole magnetic fields are given. Note that the dynamos in this study can generate only quadrupole symmetric velocities and dipole dymmetric magnetic fields. Spatial resolution is set at $n_r = 60$, $n_\theta = 192$, $n_\phi = 288$. Truncation level in the spherical harmonic expansion is $n_l = 95$, and the time increment is $\delta t = 2.5 \times 10^{-7}$.

3.2   Results

First, we search for successful dynamos in the bottom-up and top-down buoyancy cases. Figure 3.1 and 3.2 show temporal variation of the kinetic and magnetic energy density in the cases of bottom-up and top-down source. The kinetic and magnetic energy densities in Figure 3.2 are calculated as

$$
\begin{aligned}
E_{mag} &= \frac{1}{2E_k P_m} B^2 &= \frac{1}{2E_k P_m V} \int_V \left[|\vec{\nabla} \times (\vec{\nabla} \times S_p \vec{e_r})|^2 + |\vec{\nabla} \times T_t \vec{e_r}|^2 \right] dV \\
E_{kin} &= \frac{1}{2} U^2 &= \frac{1}{2V} \int_V \left[|\vec{\nabla} \times (\vec{\nabla} \times U_p \vec{e_r})|^2 + |\vec{\nabla} \times W_t \vec{e_r}|^2 \right] dV ,
\end{aligned}
$$

where V is volume of the spherical shell, and then the densities are output in time increment of 2×10^{-5}. In this study, if the magnetic energy density drops by more than two orders of magnitude, the case is defined as a failed dynamo. If the statistically steady state of the magnetic and kinetic energy is obtained, the case is treated as a successful dynamo. As a result, the steady states of the energy are achieved only in the two top-down cases which are calculated at $Ra = 4.5 Ra_c$ (in the middle of Figure 3.2) and at $Ra = 5 Ra_c$ (in the bottom of Figure 3.2). Thus, the onset of dynamo action in the top-down case starts at the Rayleigh number about $4.5 Ra_c$, where Ra_c is the critical Rayleigh number for the onset of convection, although we cannot obtain any successful dynamos up to $Ra = 20 Ra_c$ in the bottom-up case.

In Table 3.1, the time-averaged results of MHD dynamo for the top-down and bottom-up buoyancy cases, calculated at $E_k = 10^{-4}$ are represented. According to the time-averaged $|H_z^{rel}|$ in Table 3.1, although the onset of the dynamo in bottom-up case cannot be achieved in this study, the relative axial helicities are not so different between the top-down and bottom-up cases. In general, helical flows efficiently generate the magnetic field. It seems that the onset of dynamo action in our results are not related only to helicity.
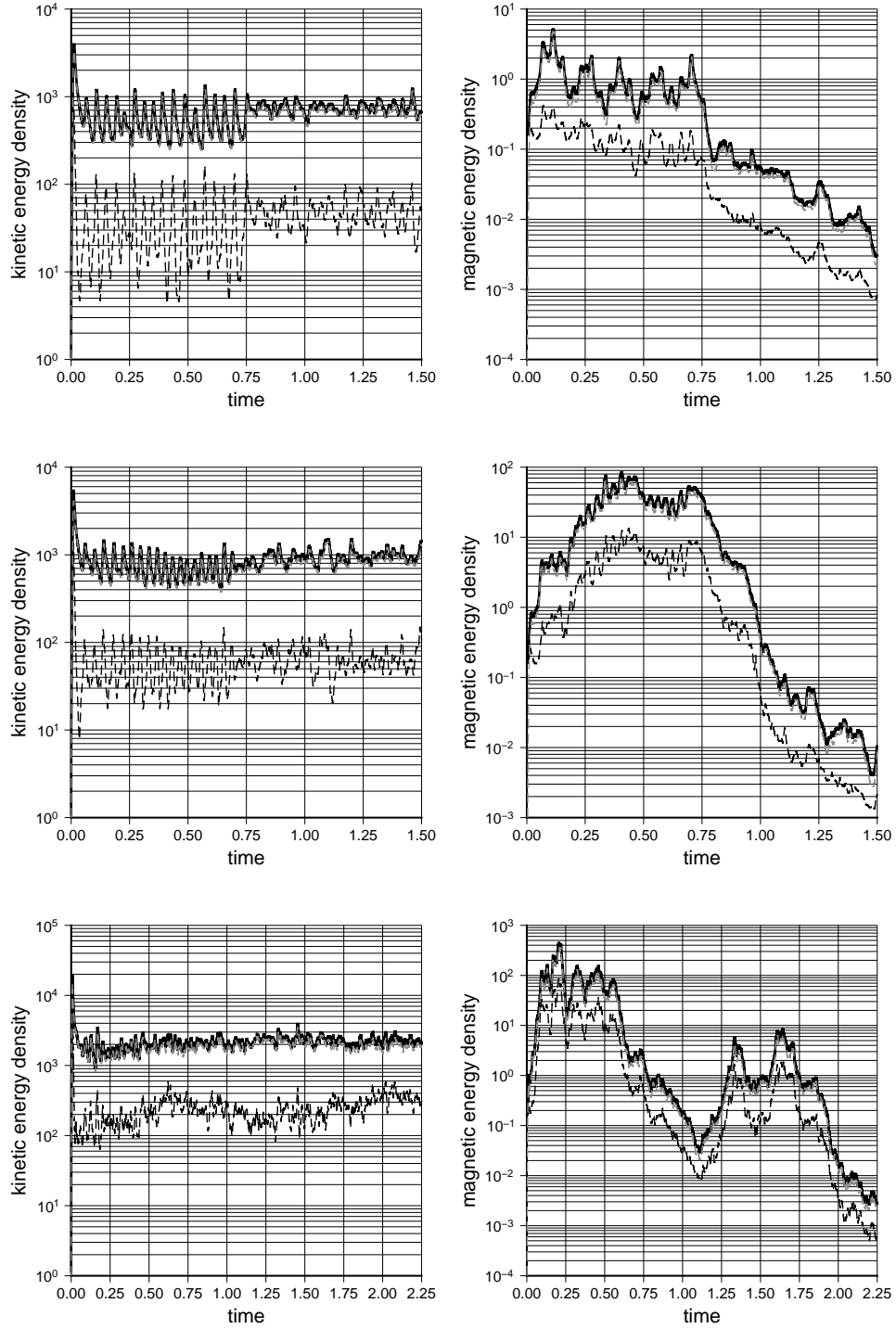
Figure 3.1: Temporal variation of the kinetic (left) and magnetic (right) energy density at $Ra = 10Ra_c$ (top), $Ra = 12Ra_c$ (middle), and $Ra = 20Ra_c$ (bottom) in the bottom-up cases. Dimensionless time is scaled by the viscous diffusion timescale. Black solid lines denote the total energy density, black broken lines denote the poloidal energy density, and grey solid lines denote the toroidal energy density The energy densities are output in time increments of 2×10^{-5}.
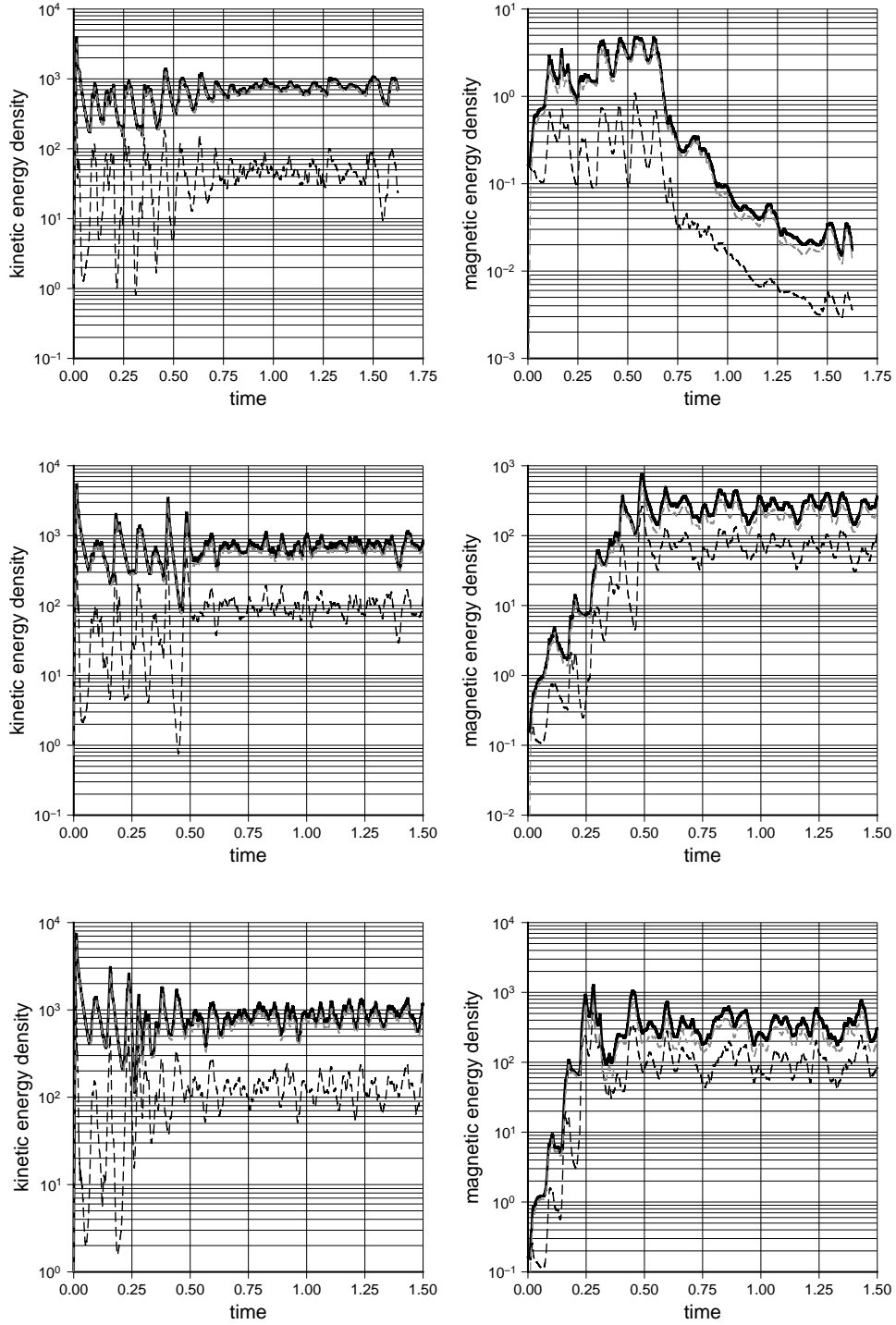
Figure 3.2: Same as Figure 3.1 but at $Ra = 4Ra_c$ (top), $Ra = 4.5Ra_c$ (middle), and $Ra = 5Ra_c$ (bottom) in the top-down cases.

The time-averaged kinetic energy and the ratio of the poloidal to toroidal kinetic energy,

$$P_{kin} = \frac{1}{2V} \int_V \left[|\vec{\nabla} \times (\vec{\nabla} \times U_p \vec{e_r})|^2 \right] \, dV$$

$$T_{kin} = \frac{1}{2V} \int_V \left[|\vec{\nabla} \times W_t \vec{e_r}|^2 \right] \, dV \ ,$$

36

Table 3.1: The time-averaged results of MHD dynamo.

Type	Ra/Ra_c	Dynamo	$\bar{E}_{kin}$	P_{kin}/T_{kin}	$|H_z^{rel}|$	Λ_i	$\bar{E}_{mag}$	P_{mag}/T_{mag}	f_{dip}	f_{oct}
T	4.0	F	770	6.8%	0.29	-	-	-	-	-
T	4.5	S	713	12%	0.36	0.14	240	23%	0.39	0.53
T	5.0	S	899	15%	0.38	0.24	405	30%	0.31	0.42
B	10	F	760	6.0%	0.35	-	-	-	-	-
B	12	F	990	7.3%	0.37	-	-	-	-	-
B	20	F	2390	16%	0.29	-	-	-	-	-

Column 1: buoyancy source type that is either bottom-up case (B) or top-down case (T); Column 2: the input Rayleigh number normalized by the critical Rayleigh number; Column 3: symbols of successful dynamo (S) or failed dynamo (F); Column 4; kinetic energy density; Column 5: the ratio of poloidal kinetic energy to toroidal kinetic energy; Column 7: Elsasser number; Column 8: magnetic energy density; Column 9 : the ratio of the poloidal magnetic energy to the toroidal magnetic energy; Column 10: dipolarity,

$$f_{dip} = \left[\int \vec{B}_{l=1}(r = R_o) \cdot \vec{B}_{l=1}(r = R_o)dS\right]^{1/2} / \left[\int \vec{B}(r = R_o) \cdot \vec{B}(r = R_o)dS\right]^{1/2}, \text{ Column 11: octupolarity,}$$

$$f_{oct} = \left[\int \vec{B}_{l=3}(r = R_o) \cdot \vec{B}_{l=3}(r = R_o)dS\right]^{1/2} / \left[\int \vec{B}(r = R_o) \cdot \vec{B}(r = R_o)dS\right]^{1/2}.$$
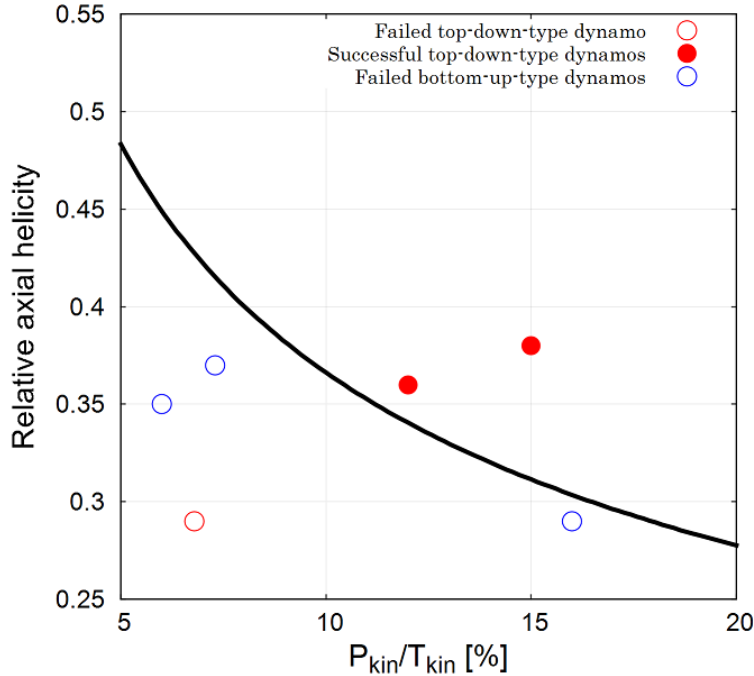
Figure 3.3: Time-averaged relative axial helicity versus the ratio of the poloidal kinetic energy to the toroidal kinetic energy, P_{kin}/T_{kin}. Red (blue) circle is in the top-down (bottom-up) cases. Solid (hollow) circle means the plot in the successful (failed) dynamo. Black line indicates the onset of the dynamo action.

in Table 3.1, increase as increasing the Rayleigh number. In the top-down buoyancy cases the successful dynamos are driven by the convection in which the ratio is more than 10 percent, although the failed bottom-up dynamo calculated at $Ra = 20Ra_c$ has the strongest ratio in the six cases.
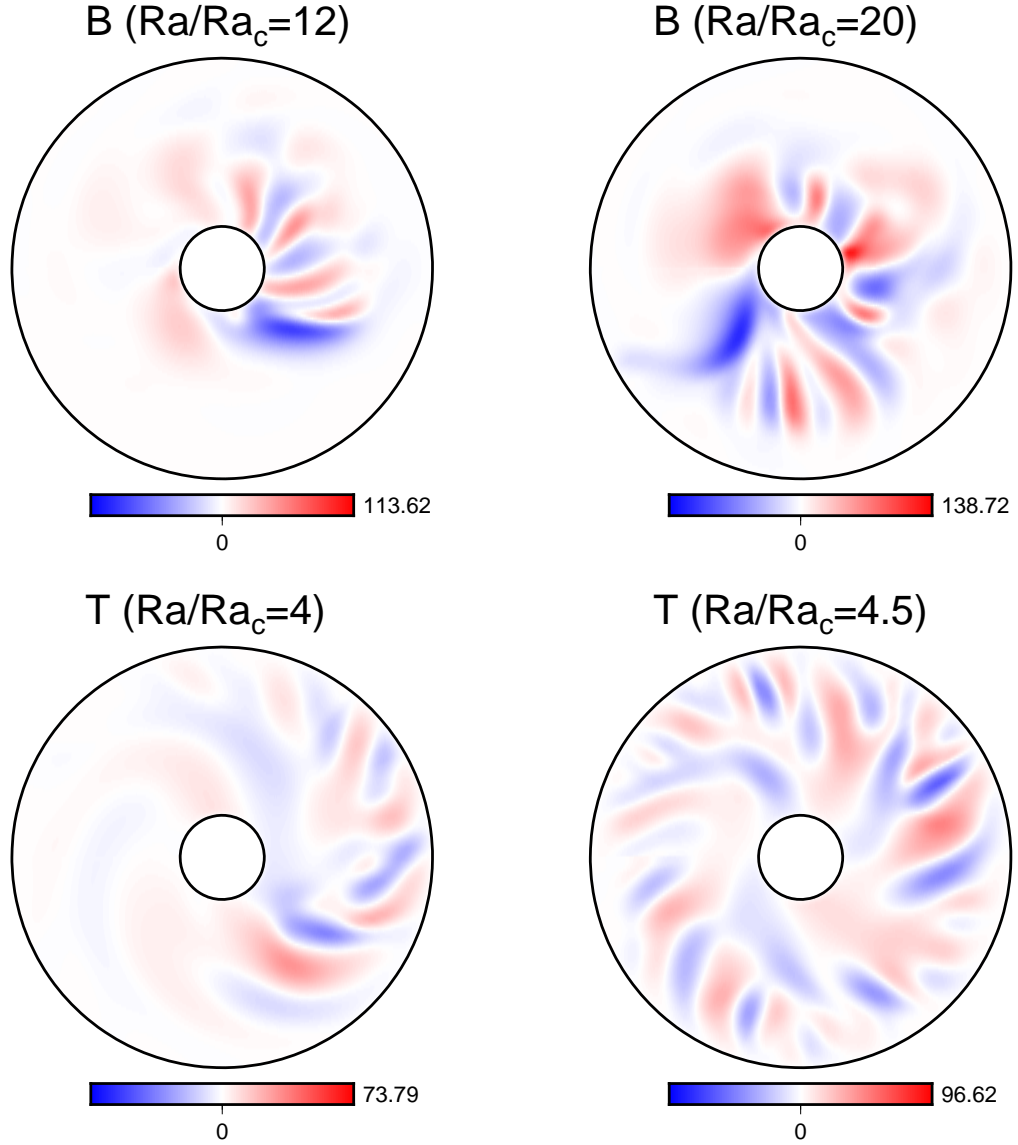
Figure 3.4: The radial component of the velocity field on the equatorial plane viewed from the north. The top (bottom) is the profile for the bottom-up case, B, (top-down case, T). The left column is the failed dynamo cases ($Ra/Ra_c = 12$ in the bottom-up case, and $Ra/Ra_c = 4$ in the top-down case), and the right column is the failed dynamo at $Ra/Ra_c = 20$ in the bottom-up case and the successful dynamo at $Ra/Ra_c = 4.5$ in the top-down case.

Figure 3.3 shows the time-averaged relativ axial helicity versus the time-averaged ratio of the poloidal kinetic energy to the toroidal kinetic energy. The successful dynamos in the top-down cases have the relative axial helicity close to that in the failed bottom-up dynamo at $Ra/Ra_c = 4$ and 4.5, but P_{kin}/T_{kin} in the successful dynamos is larger. On the other hand, the failed bottom-up dynamo at $Ra/Ra_c = 20$ generates flows with the highest P_{kin}/T_{kin}, but the lowest relative axial helicity in the six cases. Both $|H_z^{rel}|$ and P_{kin}/T_{kin} affect the onset of the dynamos, and the successful dynamos need the large value of both $|H_z^{rel}|$ and P_{kin}/T_{kin}.
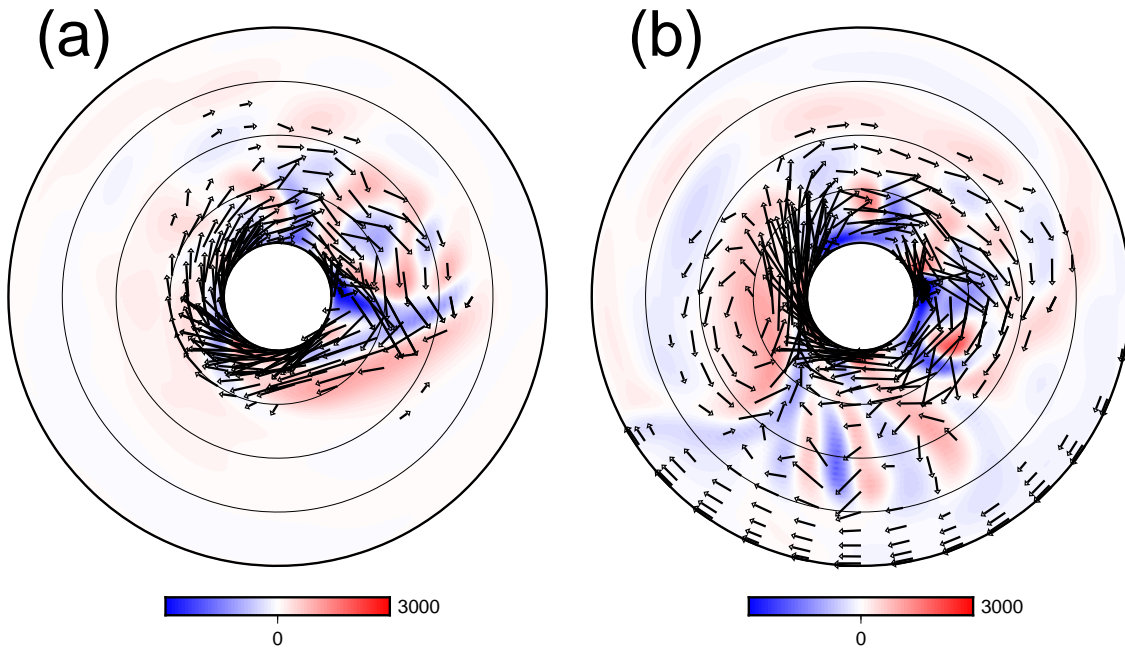
Figure 3.5: Flow patterns (arrows) and the axial vorticity (color) for the failed dynamo of the bottom-up case at $Ra = 12Ra_c$ and $t = 1.495$ (a), and $Ra = 20Ra_c$ and $t = 1.5$ (b) on the equatorial plane.
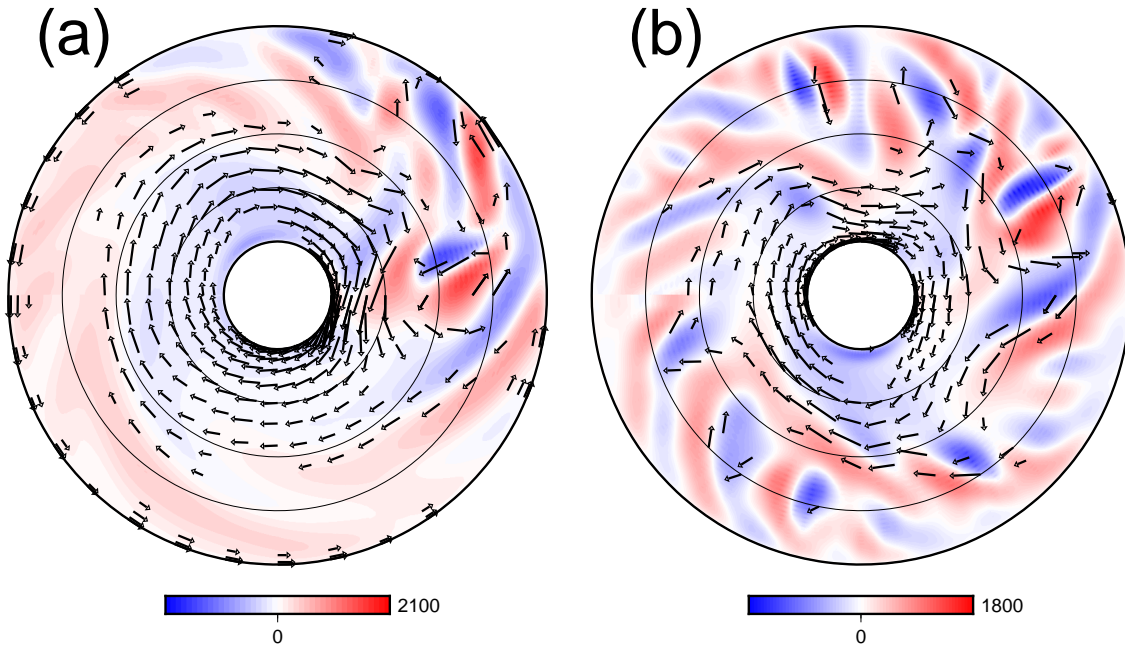
Figure 3.6: Same as Figure 3.5 but for the failed and successful dynamo of the top-down case at $Ra = 4Ra_c$ and $t = 1.49$ (a), and $Ra = 4.5Ra_c$ and $t = 1.5$ (b), respectively.
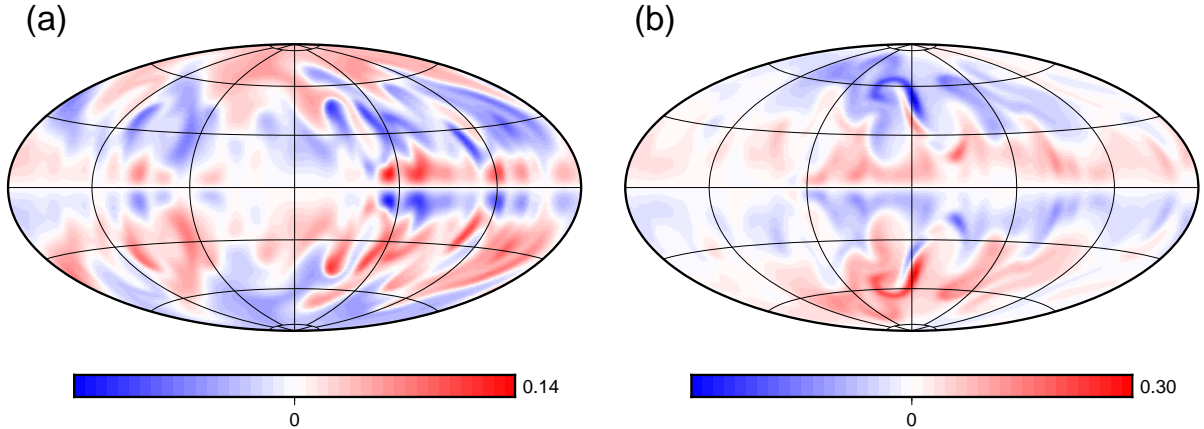
Figure 3.7: Snapshot of the radial component of the magnetic field at the outer boundary at $Ra = 4.5Ra_c$ (a) and $Ra = 5Ra_c$ (b) in the successful top-down cases.

Figure 3.4 shows the radial component of velocity on the equatorial plane for the bottom-up cases and the top-down cases. Compared with the bottom-up cases, the radial velocity concentrates in the outer region of the shell in the top-down cases. This distribution is similar to that in the internal heating case in the previous works (e.g. Hori et al. 2010[58]; Hori et al. 2012[62]). The distribution of the radial velocity in the top-down case could be affected by the conductive compositional gradient steeper than the inner region of the shell, as in the previous studies. On the other hand, the radial flows in the bottom-up case at $Ra = 12Ra_c$ and the top-down case at $Ra = 4Ra_c$ show a hemispherical asymmetry in Figure 3.4. The concentration of the radial velocity, produced only by the poloidal components, could cause the low P_{kin}/T_{kin} in table 3.1.

Figure 3.5 and 3.6 show flow patterns (arrow) and the axial component of the vorticity (color) on an equatorial plane. All the cases have the westward zonal flow in the deep part of the shell. It seems that the zonal toroidal flows become weaker than the other flows as the Rayleigh number increases in the both cases. In fact, the ratios of the kinetic energy constituted by the zonal flows to that by the total flows in the whole system decrease from 22% at $Ra = 12Ra_c$ to 13% at $Ra = 20Ra_c$ in the bottom-up cases, and from 27% at $Ra = 4Ra_c$ to 13% at $Ra = 4.5Ra_c$ in the top-down cases.

Both the convective vorticities and zonal flows are located adjacent to the inner boundary in the bottom-up cases (Figure 3.5). The zonal flows often become strong with increasing the Rayleigh number in some dynamo models (Busse, 2002[63]; Aubert, 2005[26]), where convection also becomes vigorous. According to Busse (2002)[63], but in the internal heating case, the distributions of the convective flows and the zonal flows are spatially or temporally distinct, so that the flows of the convection column can overcome the shearing action. Because the convection column has helical structure, the presence of the convection column is important for the dynamo action. It is likely to be difficult for the bottom-up type dynamos in this study that the convection is spatially distinguished from the zonal flows owing to the profile of the conductive compositional flux.

The distribution of the radial component of the magnetic field on the surface at the outer boundary in the successful top-down cases in shown in Figure 3.7. It seems that the profile of the radial magnetic field is not dipole-dominant on the outer surface. In addition, the dipolarity, which is defined by the ratio of the power in the dipole component to the total
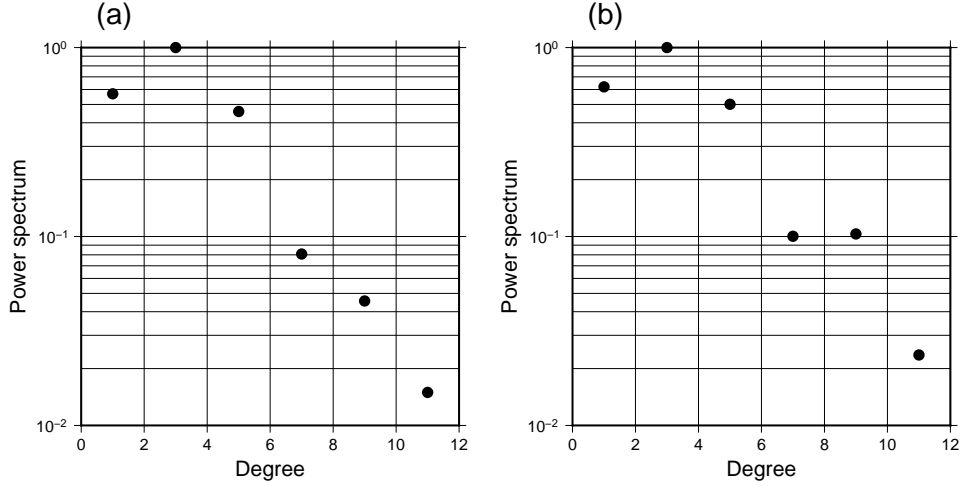
Figure 3.8: Time-averaged magnetic power spectrum at the outer boundary at $Ra = 4.5Ra_c$ (a) and $Ra = 5Ra_c$ (b) in the successful top-down cases, normalized by the value of the power at $l = 3$.

power of the magnetic field as

$$
f_{dip} = \left[\frac{\int \vec{B}_{l=1}(r = R_o) \cdot \vec{B}_{l=1}(r = R_o)dS}{\int \vec{B}(r = R_o) \cdot \vec{B}(r = R_o)dS} \right]^{1/2} ,
$$

is not so large (Table 3.1), so that the dynamos generates non-dipole dominant magnetic fields. The octupole field, which is defined as

$$
f_{oct} = \left[\frac{\int \vec{B}_{l=3}(r = R_o) \cdot \vec{B}_{l=3}(r = R_o)dS}{\int \vec{B}(r = R_o) \cdot \vec{B}(r = R_o)dS} \right]^{1/2} ,
$$

dominates the morphology rather than the dipole, (see also Figure 3.8: the time-averaged magnetic power spectrum at $r = R_o$), because the proportions of octupole field is approximately half of the total fields.

As seen in table 3.1, the successful dynamos have the Elsasser number, $\Lambda = 2P_m E_k \bar{E}_{mag}$, less than one. This means that the total effect of the Lorentz force is smaller than that of the Coriolis force. The convection in the two successful dynamos is hardly affected by the magnetic force. Thus, the force balance in the whole system could be quasi-geostrophic at the leading order.

Figure 3.9 shows zonal flows on meridional cross section in the bottom-up cases at $Ra = 12Ra_c$ and $Ra = 20Ra_c$, and the top-down cases at $Ra = 4Ra_c$ and $Ra = 4.5Ra_c$. The contour lines of the zonal flows in all the cases almost extend in the rotation-axis direction. This means that the zonal flows are almost geostrophic. In both the bottom-up cases and the top-down cases, the thermal wind and Lorentz force have little impact on the zonal flows. Figure 3.10 shows snap shots of the azimuthally-averaged mass fraction on the meridional cross section in the bottom-up cases at $Ra = 12Ra_c$ and $Ra = 20Ra_c$, and the top-down cases at $Ra = 4Ra_c$ and $Ra = 4.5Ra_c$. The axisymmetric mass fractions have homogeneous distribution on the spherical surface. Thus, thermal wind is not dominant in all cases.
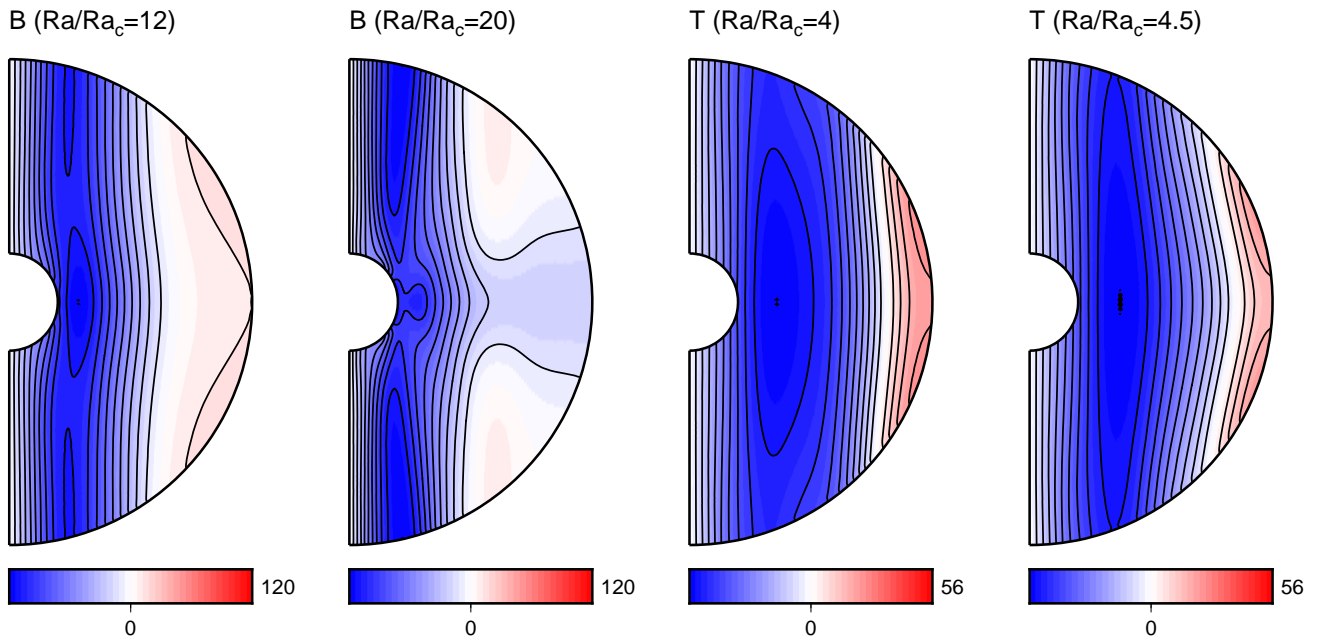
Figure 3.9: Time-averaged zonal flows on the meridional cross section in the bottom-up cases at $Ra = 12Ra_c$ and $Ra = 20Ra_c$, and the top-down cases at $Ra = 4Ra_c$ and $Ra = 4.5Ra_c$ The isolines -120 to 120 in 12 increments in the bottom-up cases, and -56 to 56 in 5.6 increments in the top-down cases.
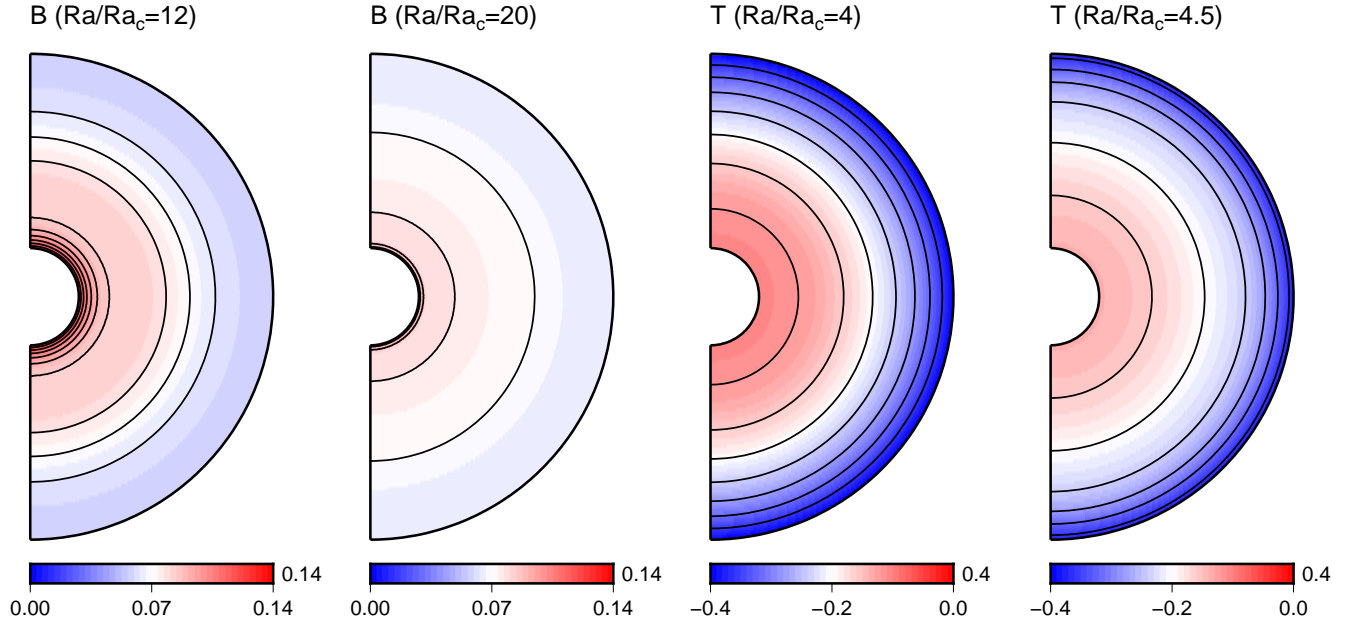
Figure 3.10: Snapshots of the azimuthally-averaged mass fraction on the meridional cross section in the bottom-up cases at $Ra = 12Ra_c$ and $Ra = 20Ra_c$, and the top-down cases at $Ra = 4Ra_c$ and $Ra = 4.5Ra_c$. Red (blue) represents high (low) values. The isolines 0 to 0.14 in 0.07 increments in the bottom-up cases, and -0.4 to 0 in 0.2 increments in the top-down cases.
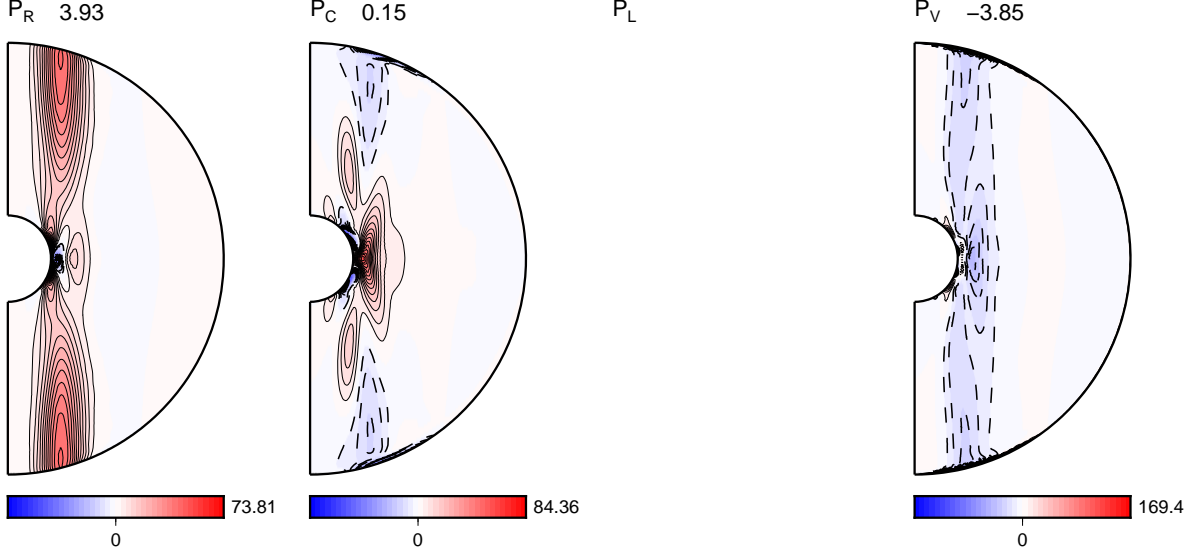
Figure 3.11: Time-averaged power budget of zonal flow in bottom-up case at $Ra = 12Ra_c$. P_R is kinetic energy flux divergence by the Reynolds stress; P_c and P_L are power exchanged by the Coriolis force, and the Lorentz force, respectively; P_V is power that include viscous dissipation and viscous energy flux convergence. The distribution of P_L is not shown because this case is the failed dynamo. The isolines in 3.69 increments in P_R, in 4.23 increments in P_c, and in 8.47 increments in P_V. The value above each figures is the volumic integration of the term.
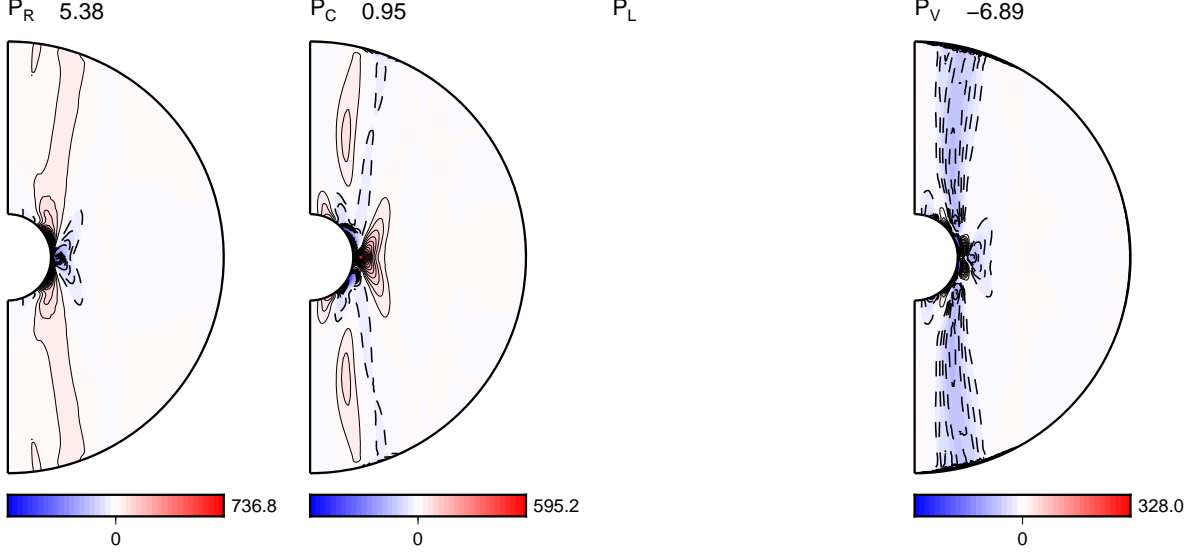
Figure 3.12: Same as Figure 3.11 but in bottom-up case at $Ra = 20Ra_c$. The isolines in 36.8 increments in P_R, in 29.8 increments in P_c, and in 16.4 increments in P_V.

The kinetic energy equation of zonal flow is written as

$$\frac{1}{2}E_k\frac{\partial \overline{u_\phi}^2}{\partial t} = -E_k\overline{[(\vec{u}\cdot\vec{\nabla})\vec{u}]_\phi}\,\overline{u_\phi} - \overline{u_s u_\phi} + \frac{1}{P_m}\overline{\left[(\vec{\nabla}\times\vec{B})\times\vec{B}\right]_\phi}\,\overline{u_\phi} + E_k\overline{\nabla^2\vec{u}_\phi}\,\overline{u_\phi}\,, \qquad (3.19)$$

43
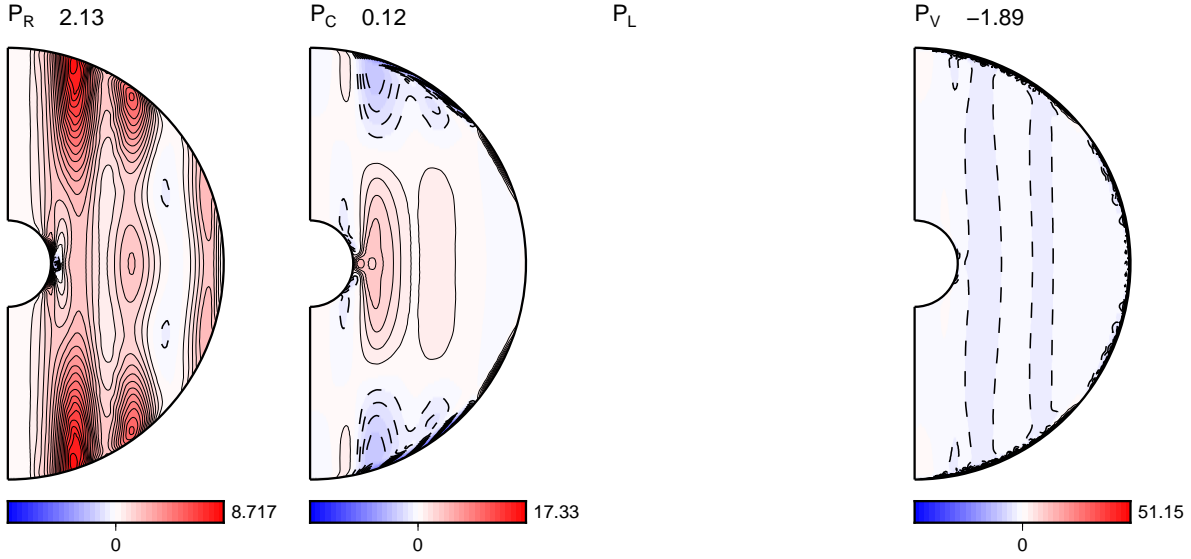
Figure 3.13: Same as Figure 3.11 but in top-down case at $Ra = 4Ra_c$. The isolines in 0.436 increments in P_R, in 0.867 increments in P_c, and in 2.56 increments in P_V
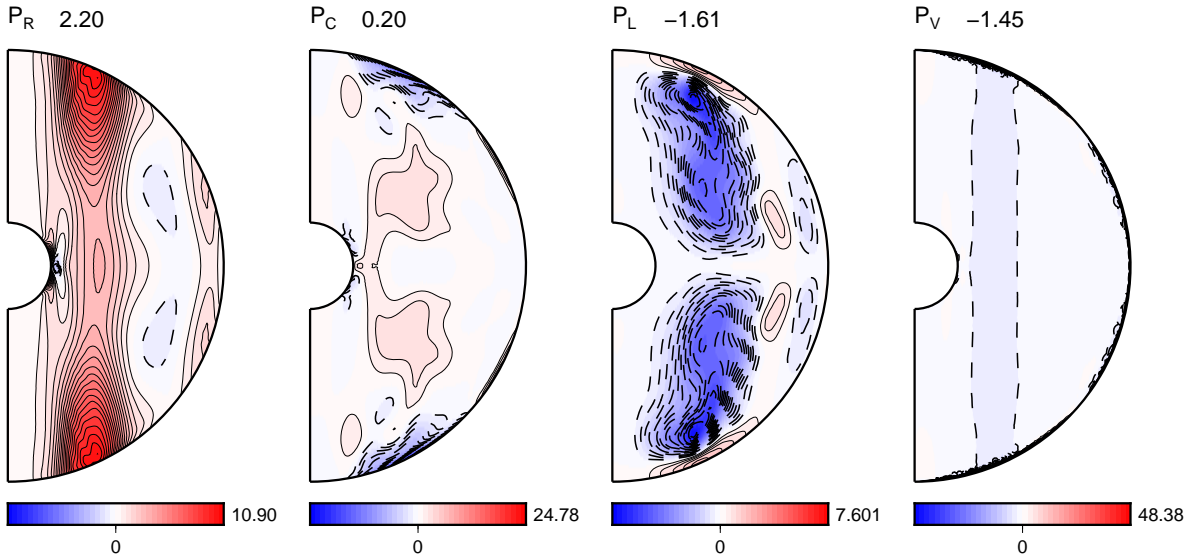
Figure 3.14: Same as Figure 3.11 but in top-down case at $Ra = 4.5Ra_c$. The isolines in 0.545 increments in P_R, in 1.24 increments in P_c, in 0.380 increments in P_L, and in 2.42 increments in P_V

where the overline means the azimuthal averaging operator. The terms on the right-hand-side in equation (3.19) are kinetic energy flux divergence by the Reynolds stress (P_R), power exchanged by the Coriolis force (P_C) and the Lorentz force (P_L), respectively, and sink that include viscous dissipation and viscous energy flux convergence (P_V). In Figures 3.11 to 3.14, the profiles of time-averaged power budget on meridional cross section are shown in the bottom-up cases at $Ra = 12Ra_c$ and $20Ra_c$, and in the top-down cases at $Ra = 4Ra_c$ and $4.5Ra_c$.

In the energy budget of zonal flows, the energy flux divergence by the Reynolds stress

is dominant in all the cases. The power exchanged by the Coriolis force is weak in all the cases, so that the zonal flows do not have the influence of zonal thermal wind. For the failed dynamos (Figures 3.11 to 3.13), the divergence by the Reynolds stress, P_R, is balanced by the viscous effect, P_V. The meridional distributions of P_R are different between the dynamos driven by two buoyancy sources; those in the bottom-up and top-down cases extend on the inner core tangent cylinder, and located outside, respectively. The distribution of P_R could be affected by the position of convection.

The successful dynamos in the top-down cases also have the strong power by the Reynolds stress, but the dominance of the sink term is not only the power exchanged by viscous force (Figure 3.14). The energy sink in the successful top-down dynamo is dominated by both the viscous and Lorentz force. A strong effect of the Lorentz force was not expected because the Elsasser number is lower than one, but the effect of the Lorentz force is strong in the zonal flows. Because the power of P_L is a work by the Lorentz force, the kinetic energy is exchanged with the zonal magnetic energy by using the zonal flow and the axisymmetric poloidal magnetic field.

The kinetic energy in the failed dynamos is dissipated by viscous effect. The distribution of P_V is located at the same region as that of P_R. In the bottom-up cases (Figure 3.11 and 3.12), P_V has positive value on the inner boundary, so that the role of the viscous effect in the kinetic energy budget is not only dissipation but also energy transfer. This profile is similar to the critical convection obtained in Chapter 2, in which the critical convection in the bottom-up cases has the strong effect of the viscous energy flux convergence on the inner boundary. It is possible that the viscous energy flux convergence plays the role of encouraging the dissipation in not only the critical convection but also the energy budget of zonal flows for the dynamo.

In the region of the work by the Lorentz force, the axisymmetric poloidal field line is twisted, and the zonal toroidal field is generated. Figures 3.15 and 3.16 show the time variation of the zonal field (color) and the axisymmetric magnetic field line (lines) for top-down cases at $Ra = 4.5Ra_c$ and $Ra = 5Ra_c$, respectively. The zonal magnetic fields are generated in the region, especially for the high latitude around the outer boundary. This mechanism is the $\omega-$effect. In the top-down successful dynamos, the $\omega-$effect arises in the region.

The axisymmetric magnetic fields in the top-down cases oscillate toward the outer boundary in the latitude direction, especially for the poloidal field lines in Figure 3.15 and 3.16. The patches of the poloidal field line move from the equator to the poles. The oscillation is also found in the previous studies with internal heating (e.g. Grote et al. 2000[57]; Busse 2002[63]; Busse and Simitev 2005[64]), although we calculate a part of the full dynamo action because quadrupole symmetric velocities and dipole magnetic fields can be generated in this study.

3.3   Discussion

In this calculation, we searched for the onset of the dynamos driven by top-down and bottom-up buoyancy by giving the critical convection and the axisymmetric dipole magnetic field as initial conditions. This system can generate only quadrupole symmetric velocities and antisymmetric magnetic fields. The restriction on the symmetry could affect the dynamo mechanism, especially for the bottom-up cases.

The onset of the dynamo driven by the top-down buoyancy was obtained at $Ra = 4.5Ra_c$ in this study. The patches of the axisymmetric magnetic fields in the successful top-down dynamos move from the equator to the poles. This result is the same as the cases with full
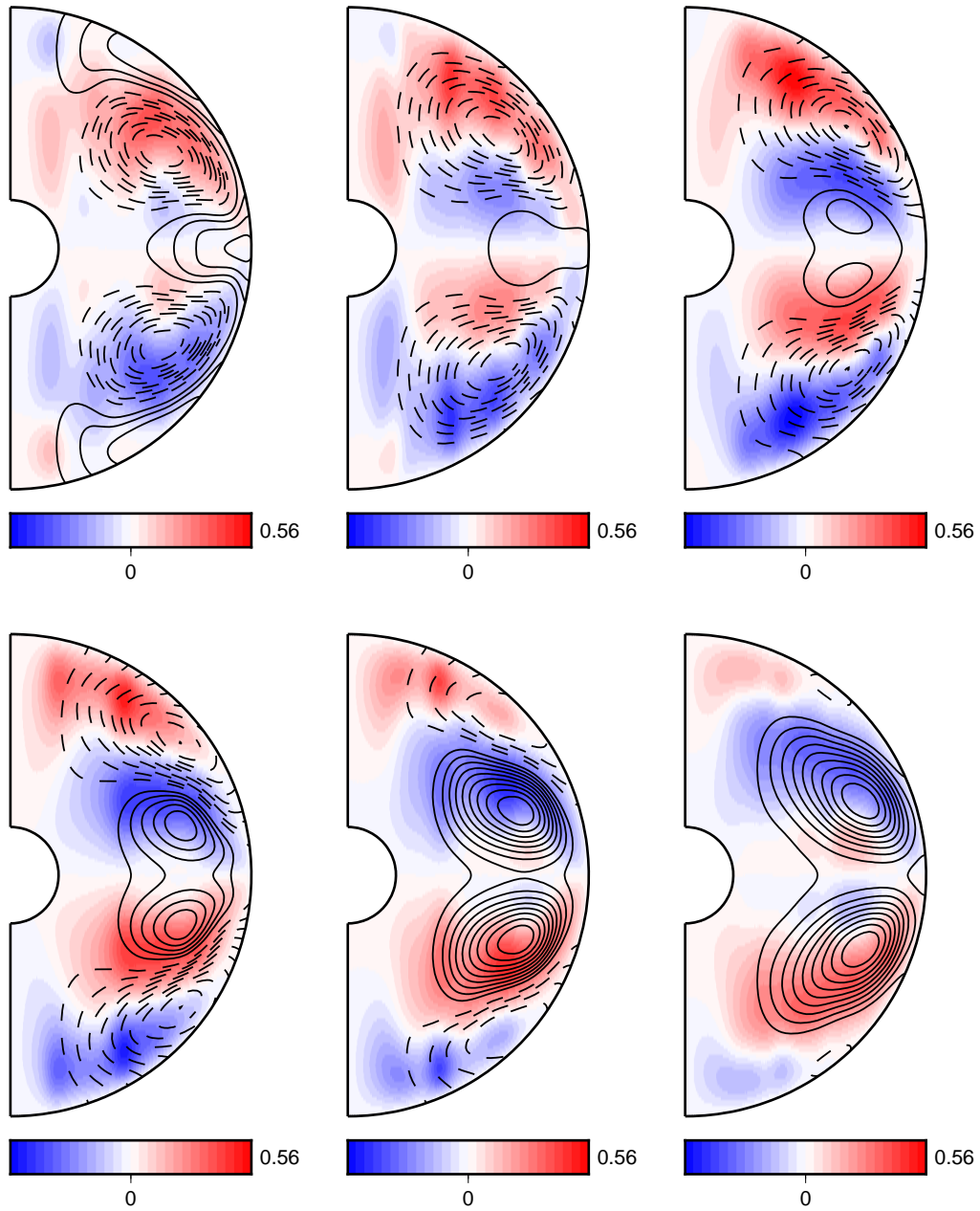
Figure 3.15: Temporal evolution of the zonal field (color) and the axisymmetric magnetic field line (lines) for top-down case at $Ra = 4.5Ra_c$ for equidistant times (from left to right in top, then in bottom) in 0.0075 time-increment. Solid (broken) lines indicate for positive (negative) values.

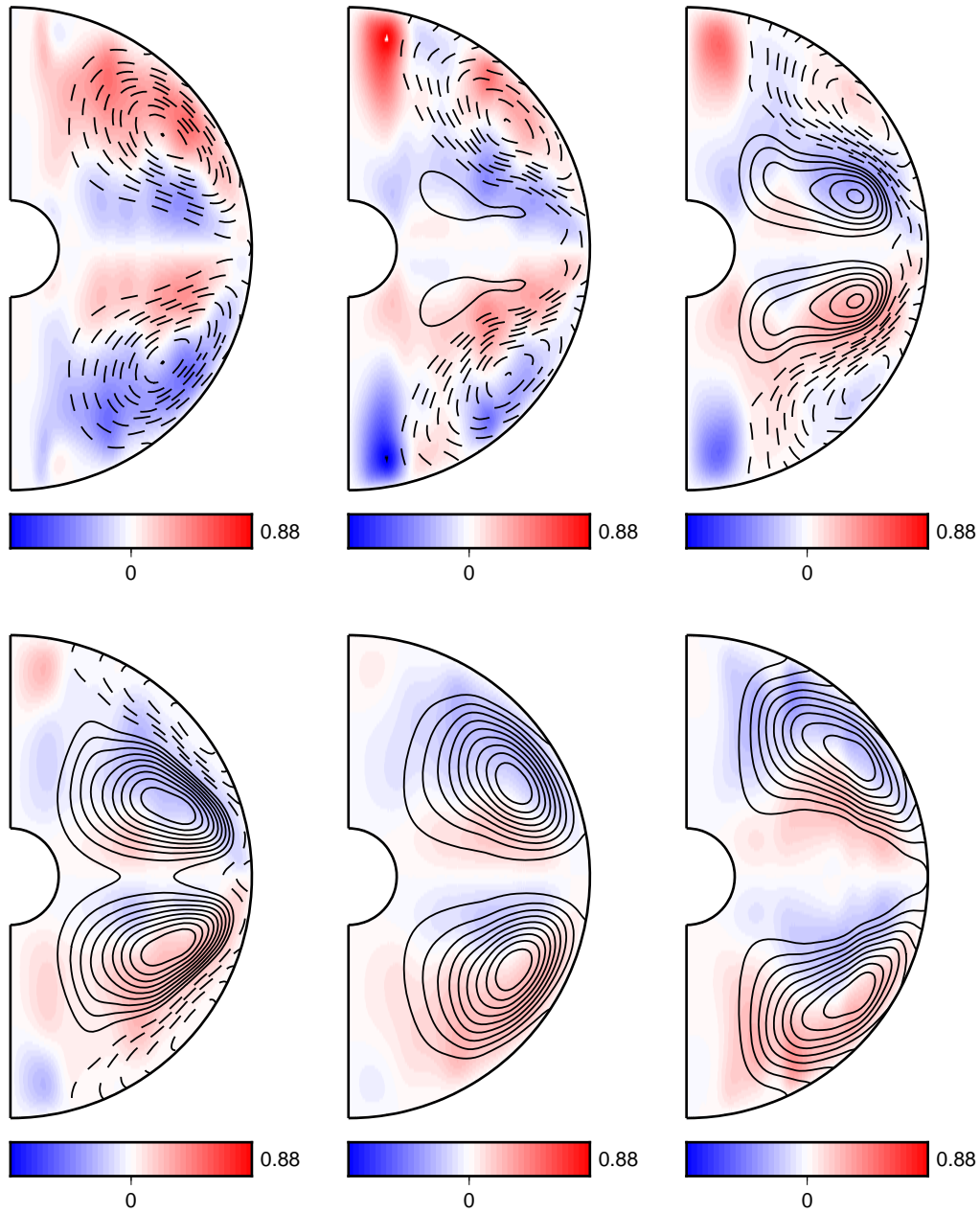dynamo action in the previous works, which consider the dynamos driven by internal heating

Figure 3.16: Same as Figure 3.15 but at $Ra = 5.0Ra_c$.

(e.g. Grote et al. 2000[57]; Busse 2002[63]; Busse and Simitev 2005[64]). In addition to the oscillation, the patterns of axisymmetric fields are similar to that in the dipolar dynamo cases in their previous works. The fact indicates that dipolar magnetic fields in top-down dynamos

can be generated by only the quadrupole-symmetric velocities from the dipole-symmetric magnetic fields.

The results for the top-down dynamo could not be affected by the boundary conditions of velocities and magnetic fields. In this study, boundary conditions are stress-free boundaries for the velocity field, and electrically insulating for the magnetic field. According to Simitev and Busse (2005)[34], the resultant magnetic fields have little difference between the dynamos with insulating and perfectly conducting inner core. For the velocity boundary conditions, if the non-magnetic system is considered, the differential rotation is stronger in the convection with no-slip boundaries than stress-free boundaries because the Ekman layer exists on no-slip boundaries. However, the difference is destroyed by the Lorentz force in the dynamos in which the Elasasser numbers are less than 1 in Simitev and Busse (2005)[34], so that the velocity boundary conditions could not vary the velocity also in our dynamos.

The compositional (or thermal) boundary conditions strongly affect the kinetic energy budget of the zonal flows in the top-down dynamos. In Hori et al. (2010)[58], when the Rayleigh numbers are a few times of the critical Rayleigh number in the dynamos driven by internal heating, the zonal flows are dominated by the Reynolds stresses in the case with the fixed temperature boundaries; in contrast, the dynamos with the fixed heat flux boundaries generate the zonal flows owing to thermal wind. They conclude that the structures in the fixed heat flux cases are promoted by force balance between the Lorentz force by the strong dipole field and the Coriolis force. However, the top-down dynamos in the present study with fixed compositional flux boundaries do not have the thermal wind. It is possible that thermal wind does not happen in the present calculation because of the restriction on symmetry of the fields, with which only the quadrupole-symmetric velocities and the dipole-symmetric magnetic fields are taken into account.

On the other hand, bottom-up dynamo did not succeed up to $Ra = 20Ra_c$. For full dynamo action, successful dynamos in similar situation are obtained at lower Rayleigh number than our result; for example, the onset of the dynamo driven by differential heating buoyancy source is about $Ra = 6Ra_c$ at $\chi = 0.2$ and $E_k = 3 \times 10^{-4}$, but $P_m = 5$ in Heimpel et al. (2005)[65]. Some successful dynamos in full dynamo action have an oscillation of two modes in axisymmetric velocity and magnetic fields, although the time-averaged fields has only one mode; for example, the zonal flows in the time average are much higher quadrupole-symmetry than in a time snapshot (Aubert, 2005[26]). For the previous work (Takahashi 2003[56]), the zonal fields often oscillate between dipolar and quadrupolar symmetries inside the tangent cylinder, but without oscillation outside. This means that the bottom-up dynamo can generate both the dipole-symmetric and quadrupole-symmetric fields inside the tangent cylinder. Because our model generates only the dipole-family magnetic field, the generation process is strongly limited in the present bottom-up cases. It could be essential for dynamo driven by bottom-up buoyancy to generate both the symmetric and antisymmetric fields. Thus, it is possible that coupling dipole-symmetric or quadrupole-symmetric flow with magnetic fields with various symmetry is essential for the onset of the dynamo.

The coupling the symmetry is significant for the Mercury's core dynamo, generating the offset-dipole magnetic field (Takahashi et al. 2019[10]). In Takahashi (2019)[10] using dynamo driven by double-diffusive convection, the dynamo fed by bottom-up-type compositional buoyancy can generate the offset-dipole magnetic field, although the kinematic dynamo action in the bottom-up case generate not offset-dipole but quadrupole-family magnetic field. Thus, the nonlinear Lorentz-force effect is essential for the Mercury's core dynamo. Because the Lorentz force couples dipole-symmetry fields with quadrupole-symmetry fields, the ful bottom-up-type dynamo action could contain the stronger nonlinear effect than the full top-down-type one.

It is possible that the zonal toroidal flows in our bottom-up failed dynamo prevent the

columnar convection from generating the large-scale magnetic fields. The zonal flows were generated by the divergence of the Reynolds stresses, although the most bottom-up dynamos in previous works (e.g. Aubert 2005[26]; Sakuraba 2007[66]) have the zonal flows owing to the zonal thermal wind even if the fixed temperature boundary conditions are satisfied. Because the thermal wind destroys geostrophic balance of zonal flows, and results in differential rotation of the flow, it is difficult for our model to generate the zonal toroidal field by ω-effect. Dynamo might fail due to the difficulty.

The core dynamics in Earth has the strong zonal flows, which are averaged over the 1840-1990 period, and the speed is about $0.3-1.0°$ par a year inside the inner core tangent cylinder (Paris and Hulot (2000)). According to the numerical dynamos in previous works, the zonal flows could be dominated by the zonal thermal wind in the dynamo driven by bottom-up type buoyancy, especially for the interior of the inner core tangent cylinder. The present results suggest a possibility of essential effects of the thermal wind on the zonal flows in the bottom-up dynamos because the effects easily generates the zonal toroidal fields owing to ω-effect. On the other hand, the top-down dynamos are likely to generate the zonal flows by Reynolds stresses in both the present and previous calculations (e.g. Busse, 2002[63]; Grote et al. (1999)[67]; Grote et al. (2000)[57]). The zonal flows by Reynolds stresses have a weaker differential rotation than that by the thermal wind because they cannot directly destroy the geostrophic balance in the zonal flows.

The different mechanisms dominating in zonal flow could affect the observed magnetic fields in the other bodies. In the case of Ganymede, it is believed that the core dynamo is mainly driven by either top-down or bottom-up type compositional buoyancy. The buoyancy types could decide the azimuthally movement of the magnetic field frozen in the zonal flows, so that the difference in the source of the zonal flows should be able to restrain the main buoyancy type in the Ganymede' core. The restraint of the buoyancy types can decide the solidification scenarios in the Ganymede's core. However, the detail of the zonal flows cannot be estimated in this study because we did not calculate full dynamo action. Future work should therefore investigate the full dynamo action, and discover the difference of kinetic energy budget of the zonal flow between bottom-up and top-down types.

Chapter 4

Conclusions

In this thesis, we investigated the onset of the convection (Chapter 2) and dynamo (Chapter 3) driven by the bottom-up and top-down buoyancy in a rotating spherical shell containing the Boussinesq fluid. This research aimed to identify the physics of the critical convection and the dynamo by comparing the results of the bottom-up cases with that of the top-down cases.

In Chapter 2, we found that the location of the critical convection produced the different kinetic energy budget between two buoyancy cases and the additional flow for the bottom-up cases. In the bottom-up cases, the additional flow inward or outward the inner core tangent cylinder is not directly generated by the buoyancy force, but important for balancing the kinetic energy budget. Because this flow could result from mass conservation on the inner boundary, this flow could be generated in the planetary core, and it might affect the core dynamics.

In Chapter 3, it was found that the top-down dynamos are achieved at a Rayleigh number less supercritical than the bottom-up cases. For the bottom-up dynamo it is difficult to generate the poloidal kinetic energy because the convective flows are destroyed by the zonal flows located in the deep part of the shell. Helicity has little connection with the source of dynamos in this research. Although the generation process caused by helical convection have been explained by the equatorially-symmetric flows and equatorially-antisymmetric magnetic fields, it might be important for the process that equatorially-asymmetric flows and equatorially-symmetric magnetic fields affect core dynamics.

Reference

[1] S. Chandrasekhar. Hydrodynamic and hydromagnetic stability. *(Oxford; Clarendon Press)(Reprinted by Dover publications)*, 1961.

[2] J.E.P. Connerney. Planetary magnetism. *Treatise on Geophysics (Amsterdam: Elsevier)*, vol. 10:243–280, 2007.

[3] A.M. Dziewonski and D.L. Anderson. Preliminary reference earth model. *Phys. Earth Planet. Inter.*, 25(4):297–356, 1981.

[4] D. Breuer, T. Rueckriemen, and T. Spohn. Iron snow, crystal floats, and inner-core growth: modes of core solidification and implications for dynamos in terrestrial planets and moons. *Prog. Earth Planet. Sci.*, 2(1):1–26, 2015.

[5] D.E. Smith, M.T. Zuber, R.J. Phillips, S.C. Solomon, S.A. Hauck, F.G. Lemoine, E. Mazarico, G.A. Neumann, S.J. Peale, J.L. Margot, et al. Gravity field and internal structure of mercury from messenger. *science*, 336(6078):214–217, 2012.

[6] S.A. Hauck, J.L. Margot, S.C. Solomon, R.J. Phillips, C.L. Johnson, F.G. Lemoine, E. Mazarico, T.J. McCoy, S. Padovan, S.J. Peale, et al. The curious case of mercury's internal structure. *J. Geophys. Res. Planets*, 118(6):1204–1220, 2013.

[7] A. Rivoldini and T. Van Hoolst. The interior structure of mercury constrained by the low-degree gravity field and the rotation of mercury. *Earth Planet. Sci. Lett.*, 377:62–72, 2013.

[8] V. Malavergne, M.J. Toplis, S. Berthet, and J. Jones. Highly reducing conditions during core formation on mercury: Implications for internal structure and the origin of a magnetic field. *Icarus*, 206(1):199–209, 2010.

[9] N.L. Chabot, E.A. Wollack, R.L. Klima, and M.E. Minitti. Experimental constraints on mercury's core composition. *Earth Planet. Sci. Lett.*, 390:199–208, 2014.

[10] F. Takahashi, H. Shimizu, and H. Tsunakawa. Mercury's anomalous magnetic field caused by a symmetry-breaking self-regulating dynamo. *Nature communications*, 10(1):1–8, 2019.

[11] B.J. Anderson, C.L. Johnson, H. Korth, R.M. Winslow, J.E. Borovsky, M.E. Purucker, J.A. Slavin, M.T. Solomon, S.C. nad Zuber, and R.L. McNutt. Low-degree structure in mercury's planetary magnetic field. *J. Geophys. Res. Planets*, 117(E12):E00L12, 2012.

[12] C.L. Johnson, M.E. Purucker, H. Korth, B.J. Anderson, R.M. Winslow, M.MH Al Asad, J.A. Slavin, I.I. Alexeev, R.J. Phillips, M.T. Zuber, et al. Messenger observations of mercury's magnetic field structure. *J. Geophys. Res. Planets*, 117(E12):E00L14, 2012.

[13] V. Kronrod. Core sizes and internal structure of earth's and jupiter's satellites. *Icarus*, 151:204–227, 2001.

[14] Y. Fei, C.M. Bertka, and L.W. Finger. High-pressure iron-sulfur compound, fe3s2, and melting relations in the fe-fes system. *Science*, 275(5306):1621–1623, 1997.

[15] Y. Fei, J. Li, C.M. Bertka, and C.T. Prewitt. Structure type and bulk modulus of fe3s, a new iron-sulfur compound. *American Mineralogist*, 85(11-12):1830–1833, 2000.

[16] L. Chudinovskikh and R. Boehler. Eutectic melting in the system fe–s to 44 gpa. *Earth Planet. Sci. Lett.*, 257(1-2):97–103, 2007.

[17] A.J. Stewart, M.W. Schmidt, W. van Westrenen, and C. Liebske. Mars: A new core-crystallization regime. *Science*, 316(5829):1323–1325, 2007.

[18] B. Chen, J. Li, and S.A. Hauck. Non-ideal liquidus curve in the fe-s system and mercury's snowing core. *Geophys. Res. Lett.*, 35(7), 2008.

[19] A.S. Buono and D. Walker. The fe-rich liquidus in the fe–fes system from 1 bar to 10 gpa. *Geochim. Cosmochim. Acta*, 75(8):2072–2087, 2011.

[20] S.A. Hauck, J.M. Aurnou, and A.J. Dombard. Sulfur's impact on core evolution and magnetic field generation on ganymede. *J. Geophys. Res. Planets*, 111(E9):E09008, 2006.

[21] X Zhan and G Schubert. Powering ganymede's dynamo. *J. Geophys. Res. Planets*, 117(E8):E08011, 2012.

[22] U.R. Christensen. Iron snow dynamo models for ganymede. *Icarus*, 247:248–259, 2015.

[23] P.H. Roberts and E.M. King. On the genesis of the earth's magnetism. *Rep. Prog. Phys.*, 76(9):096801, 2013.

[24] K. Zhang and F.H. Busse. On the onset of convection in rotating spherical shells. *Geophys. Astrophys. Fluid Dyn.*, 39(3):119–147, 1987.

[25] U.R. Christensen. Zonal flow driven by strongly supercritical convection in rotating spherical shells. *J. Fluid Mech.*, 470:115, 2002.

[26] J. Aubert. Steady zonal flows in spherical shell dynamos. *J. Fluid Mech.*, 542:53, 2005.

[27] K. Zhang. Spherical shell rotating convection in the presence of a toroidal magnetic field. *Proc. R. Soc. Lond. Ser. A: Math. Phys. Sci.*, 448(1933):245–268, 1995.

[28] P. Olson and G.A. Glatzmaier. Magnetoconvection in a rotating spherical shell: structure of flow in the outer core. *Phys. Earth Planet. Inter.*, 92(1-2):109–118, 1995.

[29] A. Pais and G. Hulot. Length of day decade variations, torsional oscillations and inner core superrotation: evidence from recovered core surface zonal flows. *Phys. Earth Planet. Inter.*, 118(3-4):291–316, 2000.

[30] C.C. Finlay and A. Jackson. Equatorially dominated magnetic field change at the surface of earth's core. *Science*, 300(5628):2084–2086, 2003.

[31] F.H. Busse. Differential rotation in stellar convection zones. *Astrophys. J.*, 159:629, 1970.

[32] F.H. Busse and L.L. Hood. Differential rotation driven by convection in a rapidly rotating annulus. *Geophys. Astrophys. Fluid Dyn.*, 21(1-2):59–74, 1982.

[33] J. Aubert, D. Brito, H.C. Nataf, P. Cardin, and J.P. Masson. A systematic experimental study of rapidly rotating spherical convection in water and liquid gallium. *Phys. Earth Planet. Inter.*, 128(1-4):51–74, 2001.

[34] R. Simitev and F.H. Busse. Prandtl-number dependence of convection-driven dynamos in rotating spherical fluid shells. *J. Fluid Mech.*, 532:365–388, 2005.

[35] K. Moffatt. *The Generation of Magnetic Fields in Electrically Conducting Fluids.* (Cambridge: Cambridge University press), 1978.

[36] D. Gubbins and E. Herrero-Bervera. *Encyclopedia of geomagnetism and paleomagnetism.* Springer Science & Business Media, 2007.

[37] E.C. Bullard and H. Gellman. Homogeneous dynamos and terrestrial magnetism. *Phil. Trans. R. Soc. Lond. A*, 247(928):213–278, 1954.

[38] T.G. Cowling. The magnetic field of sunspots. *Mon. Notices Royal Astron. Soc.*, 94:39–48, 1933.

[39] S.I. Braginskii. Self-excitation of a magnetic field during the motion of a highly-conducting fluid. *J. Exp. Theor. Phys.*, 20:726–735, 1964.

[40] D.J. Ivers, R.W. James, P. Fletcher, K.R. Franklin, R.P. Townsend, D.J. Ivers, and R.W. James. Axisymmetric antidynamo theorems in compressible non-uniform conducting fluids. *Phil. Trans. R. Soc. Lond. A*, 312(1520):179–218, 1984.

[41] E.N. Parker. Hydromagnetic dynamo models. *Astrophys. J.*, 122:293, 1955.

[42] A.M. Soward and E.C. Bullard. A kinematic theory of large magnetic reynolds number dynamos. *Phil. Trans. Roy. Soc. Lond. A*, 272(1227):431–462, 1972.

[43] P.H. Roberts and E.C. Bullard. Kinematic dynamo models. *Phil. Trans. Roy. Soc. Lond. A*, 272(1230):663–698, 1972.

[44] A. Kageyama and T. Sato. Generation mechanism of a dipole field by a magnetohydrodynamic dynamo. *Phys. Rev. E*, 55(4):4617, 1997.

[45] P. Olson, U.R. Christensen, and G.A. Glatzmaier. Numerical modeling of the geodynamo: mechanisms of field generation and equilibration. *J. Geophys. Res. Solid Earth*, 104(B5):10383–10404, 1999.

[46] E. Dormy, A. M. Soward, C. A. Jones, D. Jault, and P. Cardin. The onset of thermal convection in rotating spherical shells. *J. Fluid Mech.*, 501:43–70, 2004.

[47] C.A. Jones, A.M. Soward, and A.I. Mussa. The onset of thermal convection in a rapidly rotating sphere. *J. Fluid Mech.*, 405:157–179, 2000.

[48] W.R. Hirsching and J. Yano. Metamorphosis of marginal thermal convection in rapidly rotating self-gravitating spherical shells. *Geophys. Astrophys. Fluid Dyn.*, 74(1-4):143–179, 1994.

[49] S. Takehiro. Kinetic energy budget analysis of spiraling columnar critical convection in a rapidly rotating spherical shell. *Fluid Dyn. Res.*, 42(5):055501, 2010.

[50] F.M. Al-Shamali, M.H. Heimpel, and J.M. Aurnou. Varying the spherical shell geometry in rotating thermal convection. *Geophys. Astrophys. Fluid Dyn.*, 98(2):153–169, 2004.

[51] P.H. Roberts. On the thermal instability of a rotating-fluid sphere containing heat sources. *Phil. Trans. R. Soc. Lond. A*, 263(1136):93–117, 1968.

[52] T. Nakajima and M. Kono. Effect of helicity on the efficiency of laminar kinematic dynamos. *J. Geomag. Geoelectr.*, 45(11-12):1575–1589, 1993.

[53] P.H. Roberts and G. Schubert. Theory of the geodynamo. *Treatise on Geophysics (Amsterdam: Elsevier)*, vol. 8:57–90, 2015.

[54] K.M. Soderlund, E.M. King, and J.M. Aurnou. The influence of magnetic fields in planetary dynamo models. *Earth Planet. Sci. Lett.*, 333:9–20, 2012.

[55] V.C.A. Ferraro. The Non-uniform Rotation of the Sun and its Magnetic Field. *Mon. Not. R. Astr. Soc.*, 97(6):458–472, 1937.

[56] F. Takahashi, M. Matsushima, and Y. Honkura. Dynamo action and its temporal variation inside the tangent cylinder in mhd dynamo simulations. *Phys. Earth Planet. Inter.*, 140(1-3):53–71, 2003.

[57] E. Grote, F.H. Busse, and A. Tilgner. Regular and chaotic spherical dynamos. *Phys. Earth Planet. Inter.*, 117(1-4):259–272, 2000.

[58] K. Hori, J. Wicht, and U.R. Christensen. The effect of thermal boundary conditions on dynamos driven by internal heating. *Phys. Earth Planet. Inter.*, 182(1-2):85–97, 2010.

[59] S. Schmitz and A. Tilgner. Transitions in turbulent rotating rayleigh-bénard convection. *Geophys. Astrophys. Fluid Dyn.*, 104(5-6):481–489, 2010.

[60] L. D. Landau and E.M. Lifshitz. Fluid mechanics 2nd edn. *(Course of Theoretical Physics)(Oxford: Pergamon)*, 6:p 539, 1987.

[61] F. Takahashi. Implementation of a high-order combined compact difference scheme in problems of thermally driven convection and dynamo in rotating spherical shells. *Geophys. Astrophys. Fluid Dyn.*, 106(3):231–249, 2012.

[62] K. Hori, J. Wicht, and U.R. Christensen. The influence of thermo-compositional boundary conditions on convection and dynamos in a rotating spherical shell. *Phys. Earth and Planet. Inter.*, 196:32–48, 2012.

[63] F.H. Busse. Convective flows in rapidly rotating spheres and their dynamo action. *Phys. fluids*, 14(4):1301–1314, 2002.

[64] F.H. Busse and R. Simitev. Dynamos driven by convection in rotating spherical shells. *Astron. Nachrichten: Astronomical Notes*, 326(3-4):231–240, 2005.

[65] M.H. Heimpel, J.M. Aurnou, F.M. Al-Shamali, and N.G. Perez. A numerical study of dynamo action as a function of spherical shell geometry. *Earth Planet. Sci. Lett.*, 236(1-2):542–557, 2005.

[66] A. Sakuraba. A jet-like structure revealed by a numerical simulation of rotating spherical-shell magnetoconvection. *J. Fluid Mech.*, 573:89, 2007.

[67] E. Grote, F.H. Busse, and A. Tilgner. Convection-driven quadrupolar dynamos in rotating spherical shells. *Phys. Rev. E*, 60(5):R5025, 1999.

Appendix

Toroidal and poloidal vector field

In this thesis, the unknown vector was expanded with toroidal and poloidal components. In chapter 2, the velocity was represented by using a poloidal scalar, U, and a toroidal scalar, W, as a form of $\vec{u} = \vec{\nabla} \times (\vec{\nabla} \times U\vec{r}) + \vec{\nabla} \times W\vec{r}$. In a system of spherical coordinates (r, θ, ϕ), the components of the poloidal and toroidal flows are:

$$U_r = \frac{L_2 U}{r}, \qquad U_\theta = \frac{1}{r}\frac{\partial^2 (rU)}{\partial \theta \partial r}, \qquad U_\phi = \frac{1}{r\sin\theta}\frac{\partial^2 (rU)}{\partial \phi \partial r}$$

$$W_r = 0, \qquad W_\theta = \frac{1}{\sin\theta}\frac{\partial W}{\partial \phi}, \qquad W_\phi = -\frac{\partial W}{\partial \theta}.$$

The curl of the velocity, i.e. vorticity, $\vec{\omega}$, is represented as

$$\vec{\omega} = \vec{\nabla} \times \vec{u} = \vec{\nabla} \times [\vec{\nabla} \times (\vec{\nabla} \times U\vec{r})] + \vec{\nabla} \times (\vec{\nabla} \times W\vec{r})$$
$$= \vec{\nabla} \times [-\nabla^2 (U\vec{r})] + \vec{\nabla} \times (\vec{\nabla} \times W\vec{r})$$
$$= \vec{\nabla} \times \left[\left(-\frac{1}{r}\frac{\partial^2 (rU)}{\partial r^2} + \frac{L_2 U}{r^2}\right)\vec{r}\right] + \vec{\nabla} \times (\vec{\nabla} \times W\vec{r}).$$

In chapter 3, the expansion is a little difference from chapter 2: $\vec{u} = \vec{\nabla} \times (\vec{\nabla} \times U\vec{e_r}) + \vec{\nabla} \times W\vec{e_r}$ and $\vec{B} = \vec{\nabla} \times (\vec{\nabla} \times S\vec{e_r}) + \vec{\nabla} \times T\vec{e_r}$. In a system of spherical coordinates (r, θ, ϕ), the components of the poloidal and toroidal magnetic fields are:

$$S_r = \frac{L_2 S}{r^2}, \qquad S_\theta = \frac{1}{r}\frac{\partial^2 S}{\partial \theta \partial r}, \qquad S_\phi = \frac{1}{r\sin\theta}\frac{\partial^2 S}{\partial \phi \partial r}$$

$$T_r = 0, \qquad T_\theta = \frac{1}{r\sin\theta}\frac{\partial T}{\partial \phi}, \qquad T_\phi = -\frac{1}{r}\frac{\partial T}{\partial \theta},$$

and the curl of the magnetic field, i.e. electric current, has a form as

$$\vec{\nabla} \times \vec{B} = \vec{\nabla} \times \left[\left(-\frac{\partial^2 S}{\partial r^2} + \frac{L_2 S}{r^2}\right)\vec{e_r}\right] + \vec{\nabla} \times (\vec{\nabla} \times T\vec{e_r}).$$

Spherical harmonics

The scalars, U, W, S and T, and composition, ξ, are expanded in spherical harmonics, $Y_l^{mc,s}$: for example,

$$U(r, \theta, \phi, t) = U(r, t)Y_l^{mc,s}(\theta, \phi).$$

$Y_l^{mc,s}$ are defined in this thesis as

$$Y_l^{mc}(\theta, \phi) = P_l^m(\cos\theta)\cos m\phi$$
$$Y_l^{ms}(\theta, \phi) = P_l^m(\cos\theta)\sin m\phi \,,$$

where P_l^m is the normalized associated Legendre function:

$$\int_0^\pi P_l^m(\cos\theta)P_l^m(\cos\theta)\sin\theta d\theta = 1 \,.$$

Two functions of spherical harmonics are orthogonal when integrated over the surface of a sphere:

$$\int_0^{2\pi} Y_{l_1}^{m_1 c,s}(\theta, \phi)Y_{l_2}^{m_2 c,s}(\theta, \phi)\sin\theta d\theta d\phi = \delta_{l_1 l_2}\delta_{m_1 m_2}n_{m_1}$$

$$\int_0^{2\pi} Y_l^{mc,s}(\theta, \phi)Y_l^{ms,c}(\theta, \phi)\sin\theta d\theta d\phi = 0 \,,$$

where $n_{m_1} = (1 + \delta_{m_1,0})\pi$. We use the identity

$$L_2 Y_l^{mc,s} = l(l+1)Y_l^{mc,s} \,.$$

Basic state of composition

The unknown variation often separates here into basic state of hydrostatic and its perturbation. In terms of composition (or temperature), the governing equation of the basic state is

$$\kappa\nabla^2\xi_o + \sigma = 0 \,,$$

where κ is the compositional diffusivity, and σ is the rate of heating by source. When we assume that ξ_o is homogeneous on a spherical surface, the equation is rewritten as

$$\frac{1}{r^2}\frac{\partial}{\partial r}\left(r^2\frac{\partial\xi_o}{\partial r}\right) = -\frac{\sigma}{\kappa} \,,$$

and then

$$\frac{\partial\xi_o}{\partial r} = -\frac{1}{3}\frac{\sigma}{\kappa}r + \frac{C}{r^2} \,,$$

where C is a integration constant.

For internal heating case, C is often negligible, and the radial gradient of ξ_o is

$$\frac{\partial\xi_o}{\partial r} = -\frac{1}{3}\frac{\sigma}{\kappa}r$$
$$\equiv -\beta r$$

The flux at outer boundary is the largest in the spherical system.

Another case is differential heating of no compositional source, thus

$$\frac{\partial\xi_o}{\partial r} = \frac{C}{r^2} \,.$$

The boundary conditions in this case is often $\xi_o = \xi_1$ at the inner boundary $(r = R_i)$ and $\xi_o = \xi_1 + \Delta\xi_o$ at the outer boundary $(r = R_o)$. Thus, the flux is rewritten as

$$\frac{\partial \xi_o}{\partial r} = -\Delta\xi_o \frac{R_i R_o}{r^2} ,$$

and has the maximum at the inner boundary.

When we consider only the compositional convection in the Earth, the flux is often zero at the core-mantle boundary. The boundary conditions are $d\xi_o/dr = -h_i(< 0)$ at $r = R_i$ and $d\xi_o/dr = 0$ at $r = R_o$, then the compositional flux of the basic state is represented as

$$\frac{\partial \xi_o}{\partial r} = \frac{R_i^2 h_i}{R_o^3 - R_i^3}\left(r - \frac{R_o^3}{r^2}\right).$$

In the thermal convection by removal from mantle convection and the compositional convection in the Ganymede, the flux is supplied from the outer boundary. The boundary conditions are $d\xi_o/dr = 0$ at $r = R_i$ and $d\xi_o/dr = -h_o(< 0)$ at $r = R_o$, then the compositional (or thermal) flux of the basic state is represented as

$$\frac{\partial \xi_o}{\partial r} = -\frac{R_o^2 h_o}{R_o^3 - R_i^3}\left(r - \frac{R_i^3}{r^2}\right).$$

The radial distribution is shown in Figure 4.1, in which the radial ratio is set up at 0.2, and the Prandtl number is one as an example.
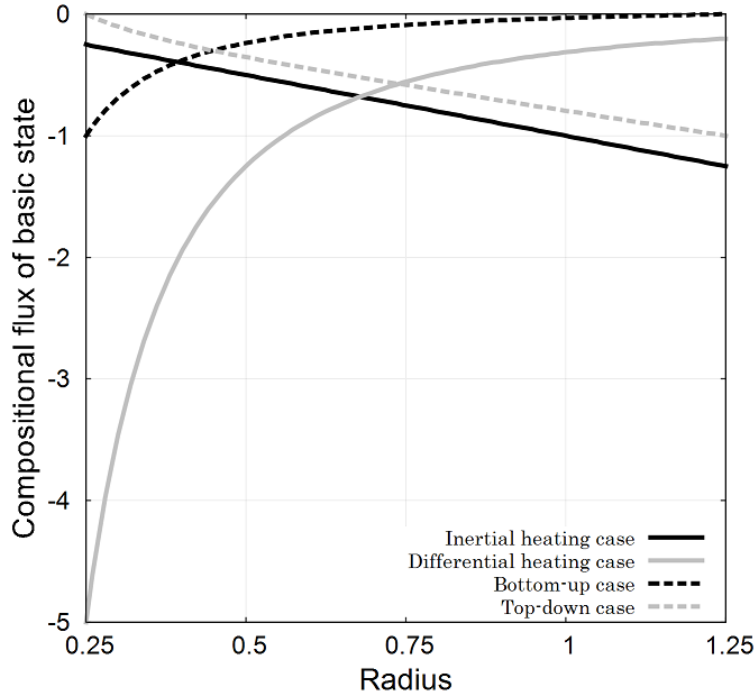
Figure 4.1: Radial gradient of compositional basic state, $d\xi_o/dr$ The black solid line is the compositional flux in the inertial heating case.; the grey solid line is in the differential heating case.; the black broken line is in the bottom-up case.; the grey broken line is in the top-down case.

Linear stability analysis

Flow patterns at onset

In chapter 2, we shows flow patterns in the bottom-up and top-down type convection at $E_k = 5 \times 10^{-5}$ as the examples. Here, flow patterns in all the cases are showed in following figures.
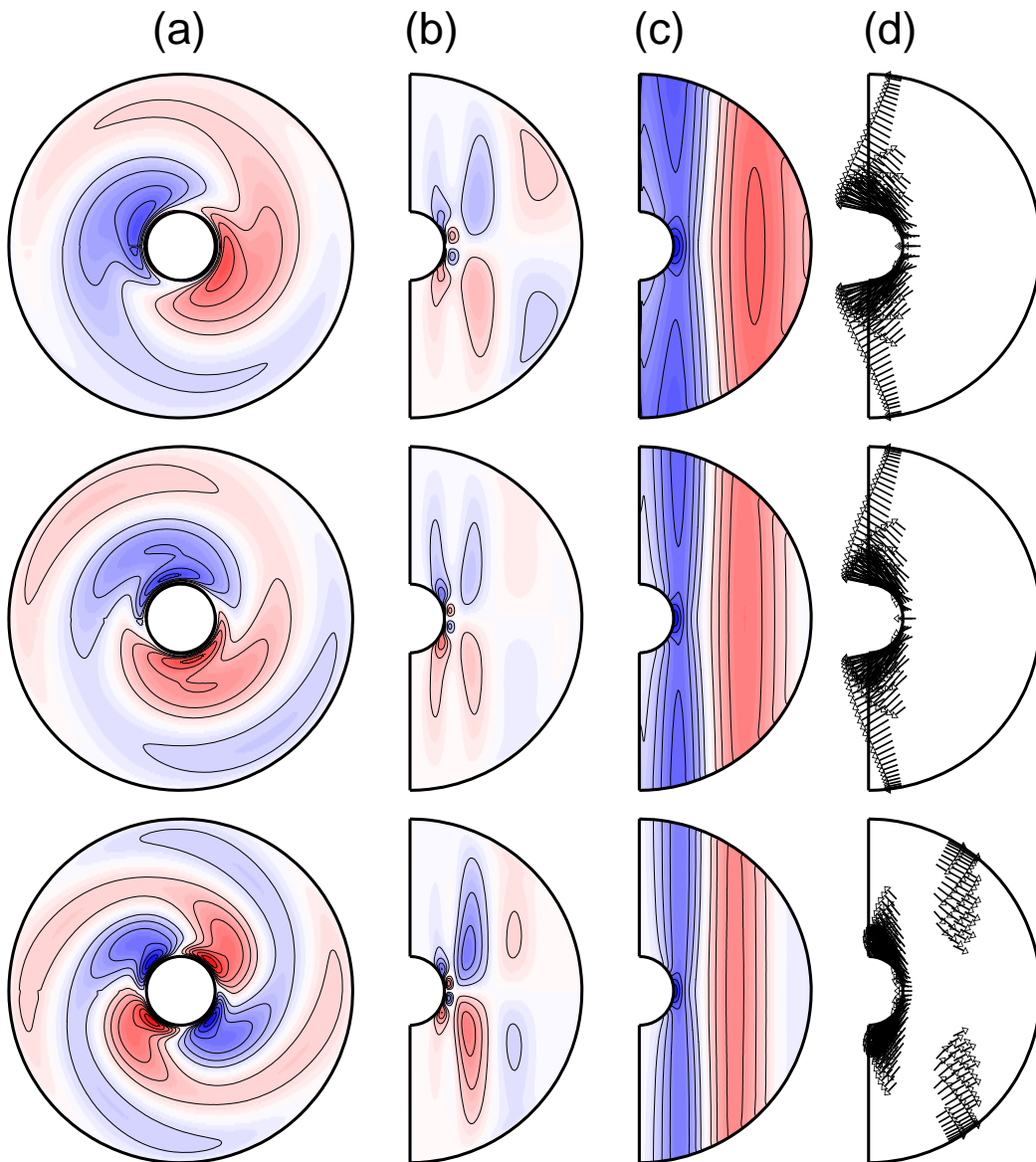

Figure 4.2: Flow patterns in the bottom-up cases, calculated at $E_k^{-1} = 1000$, 2000 and 3000 from top to bottom. The figures show that (a) rotating-axial vorticity in the equatorial plane, (b), (c) and (d) rotating-axial helicity, the azimuthal component of the velocity, and the flow vector in a meridional cross section through the middle of the cyclone.
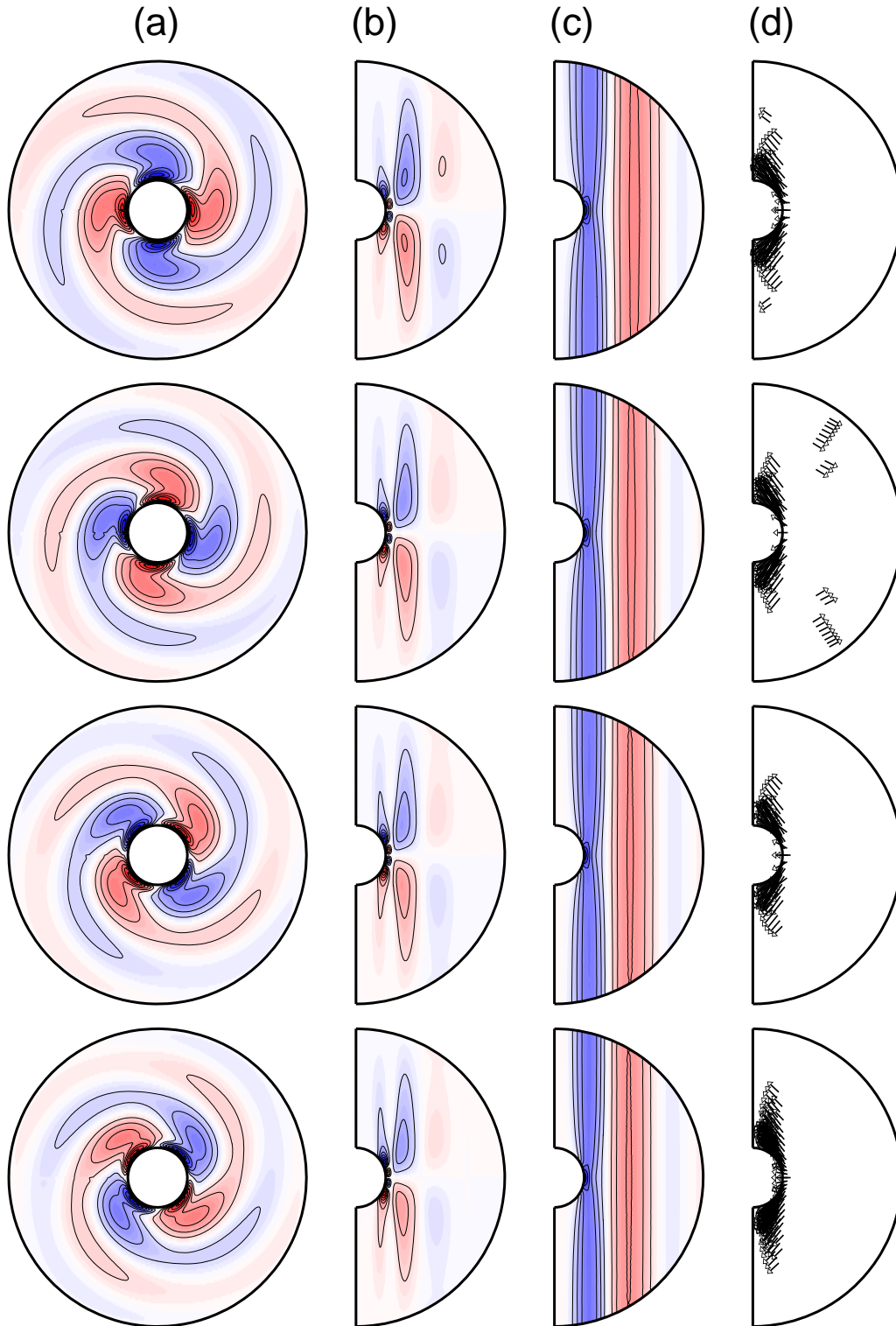
Figure 4.3: Same as Figure 4.2 but at $E_k^{-1} = 4000$, 5000, 6000, and 7000 from top to bottom.
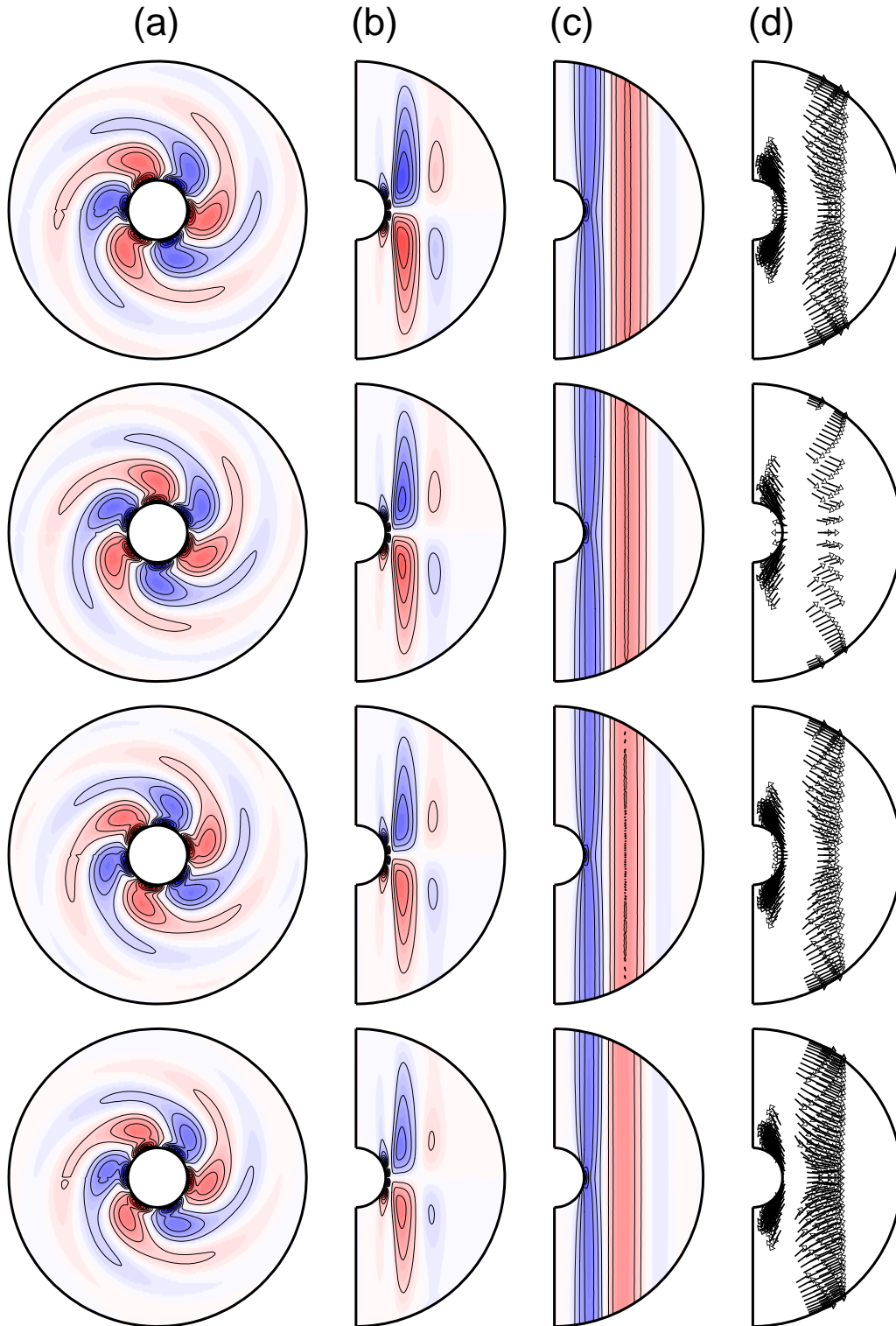
Figure 4.4: Same as Figure 4.2 but at $E_k^{-1} = 8000$, 9000, 10000, and 11000 from top to bottom.
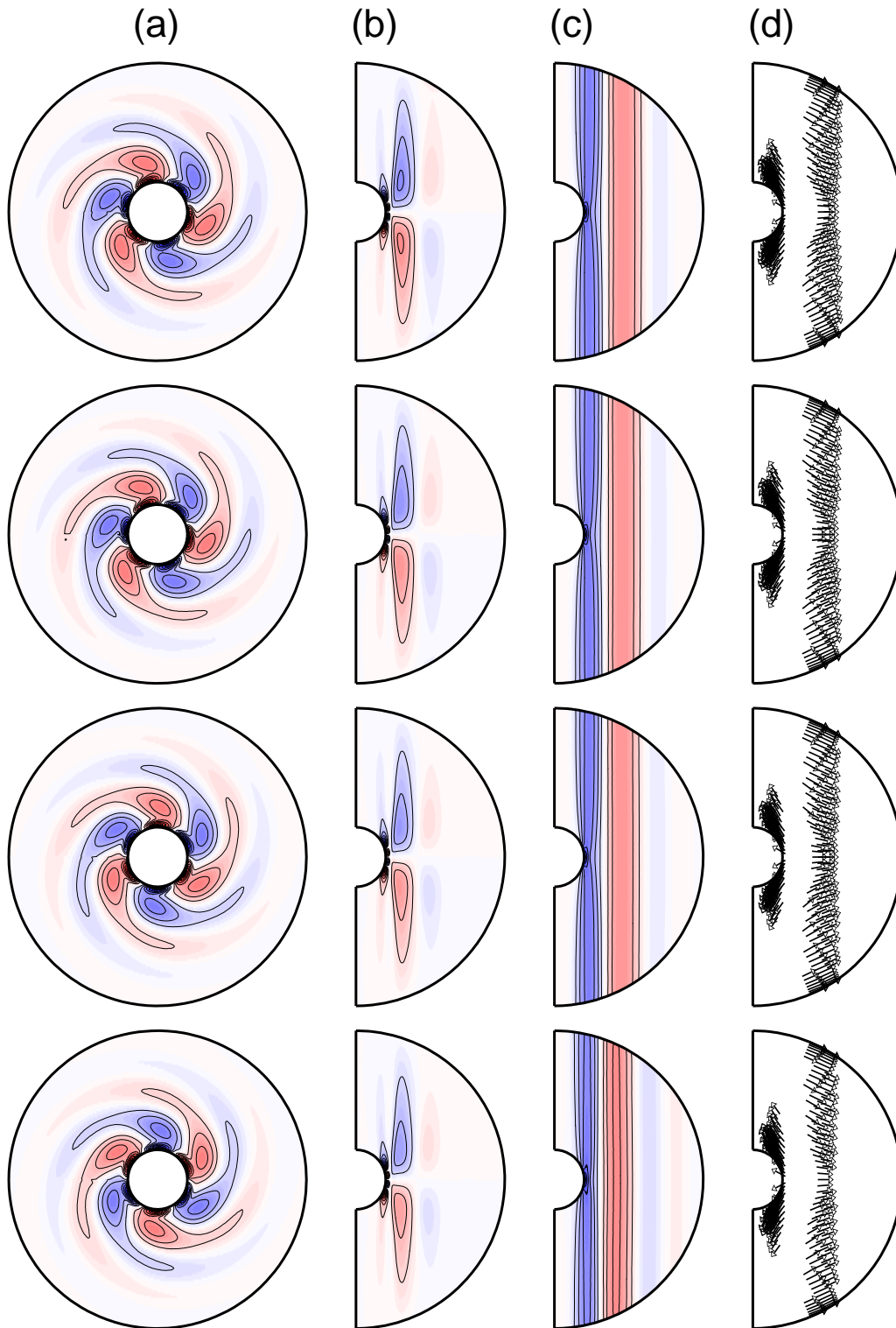
Figure 4.5: Same as Figure 4.2 but at $E_k^{-1} = 12000$, 13000, 14000, and 15000 from top to bottom.
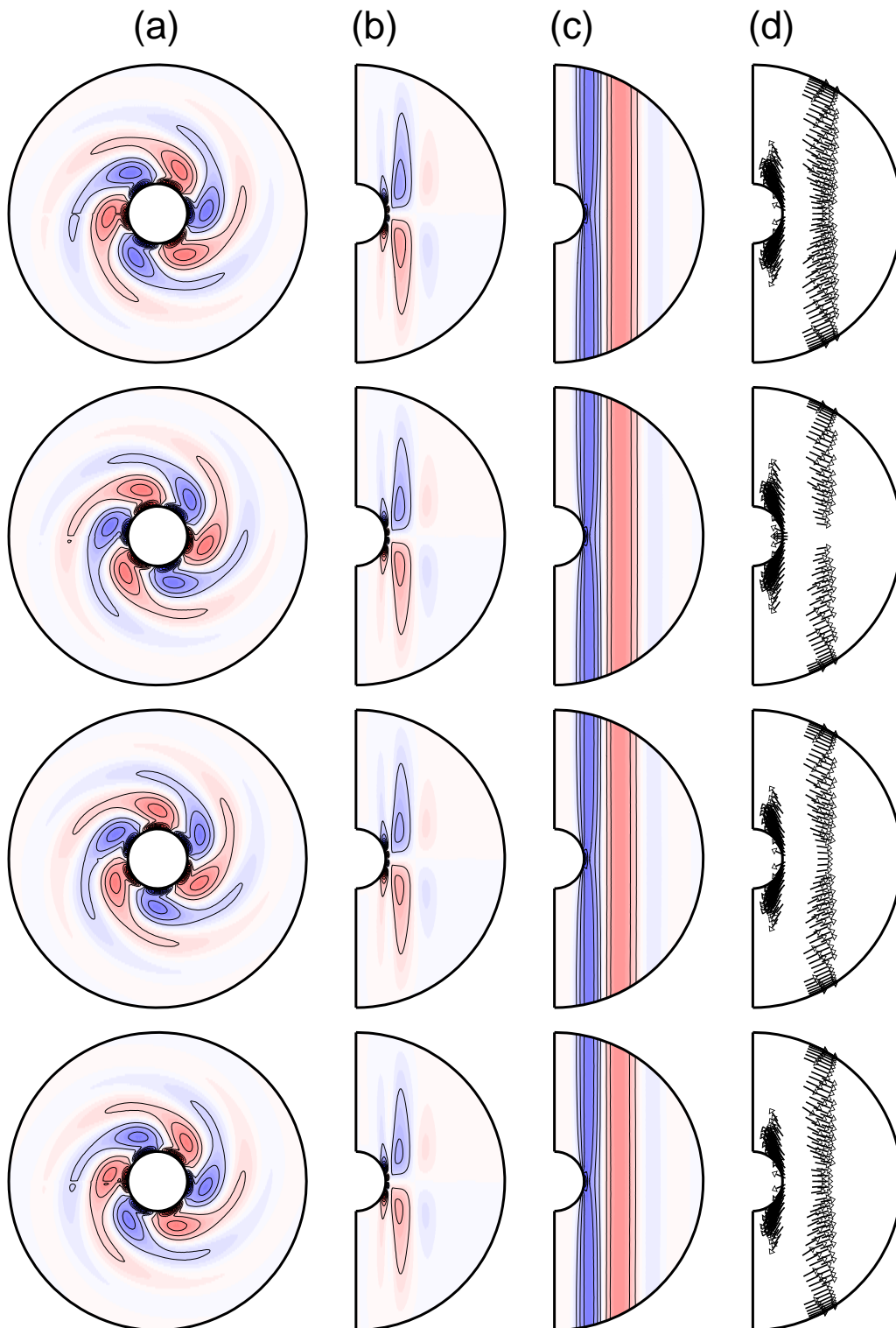
Figure 4.6: Same as Figure 4.2 but at $E_k^{-1} = 16000$, 17000, 18000, and 19000 from top to bottom.
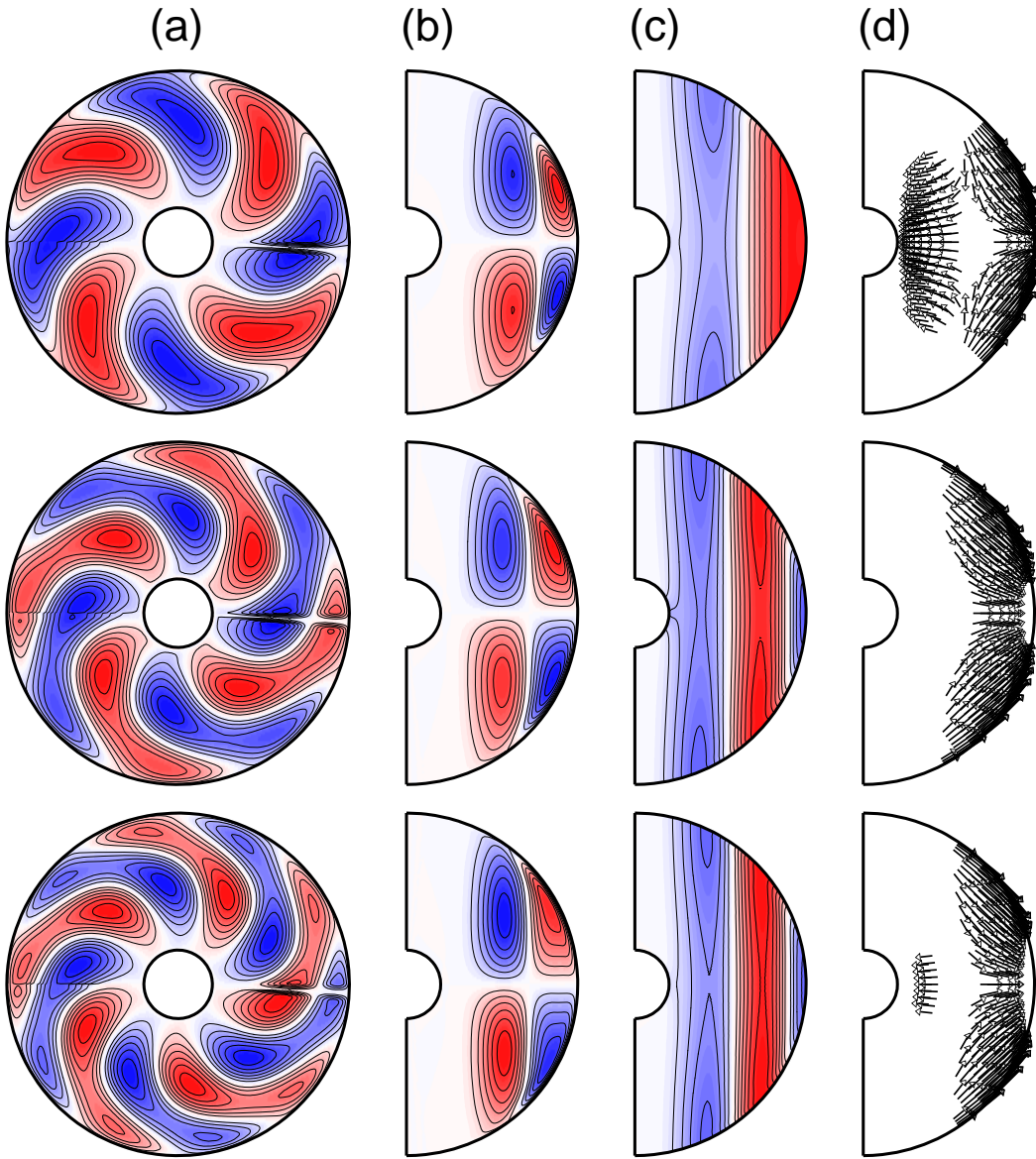
Figure 4.7: Same as Figure 4.2 but at $E_k^{-1} = 1000$, 2000 and 3000 in the top-down cases in from top to bottom.
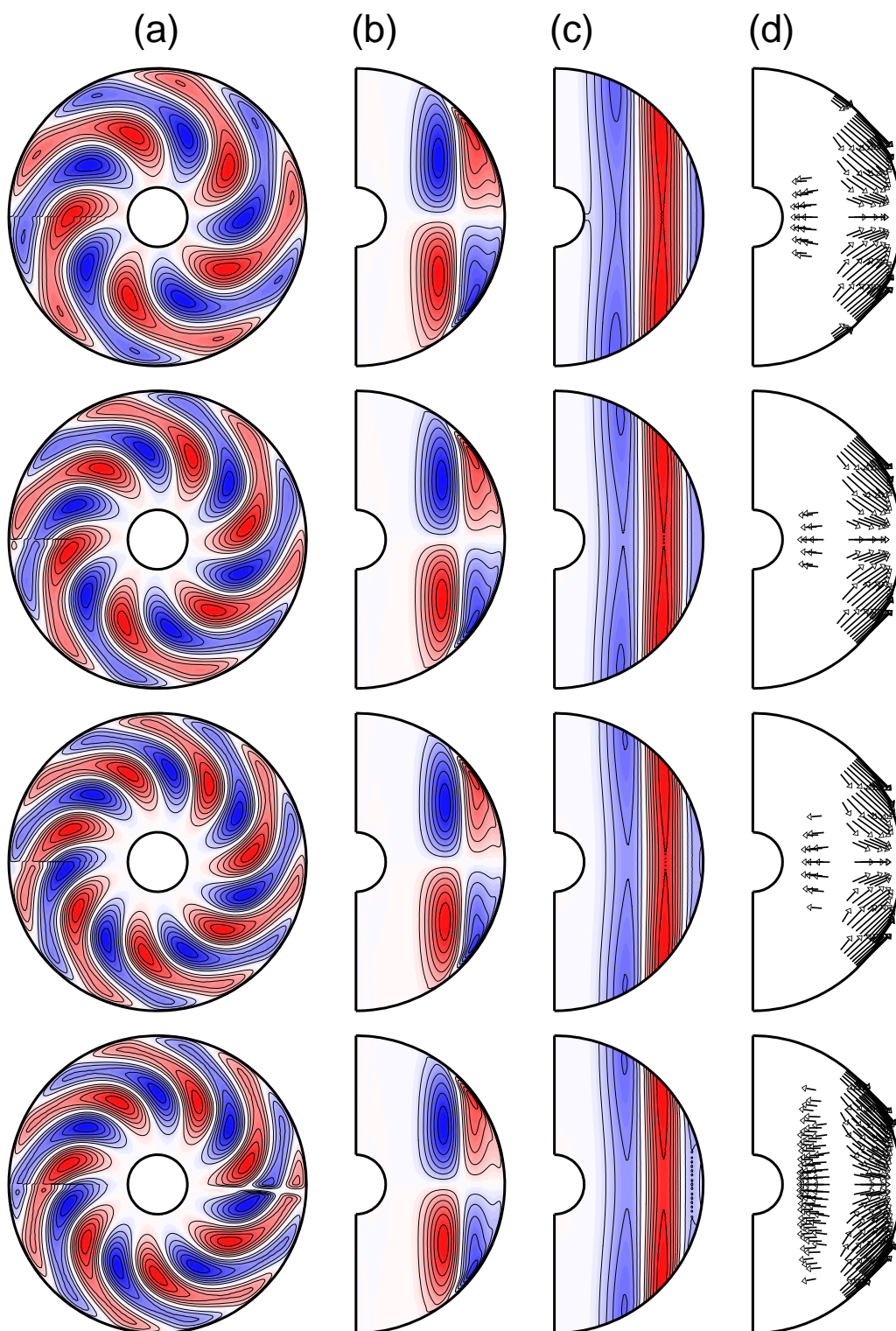
Figure 4.8: Same as Figure 4.2 but at $E_k^{-1} = 4000$, 5000, 6000, and 7000 in the top-down cases from top to bottom.
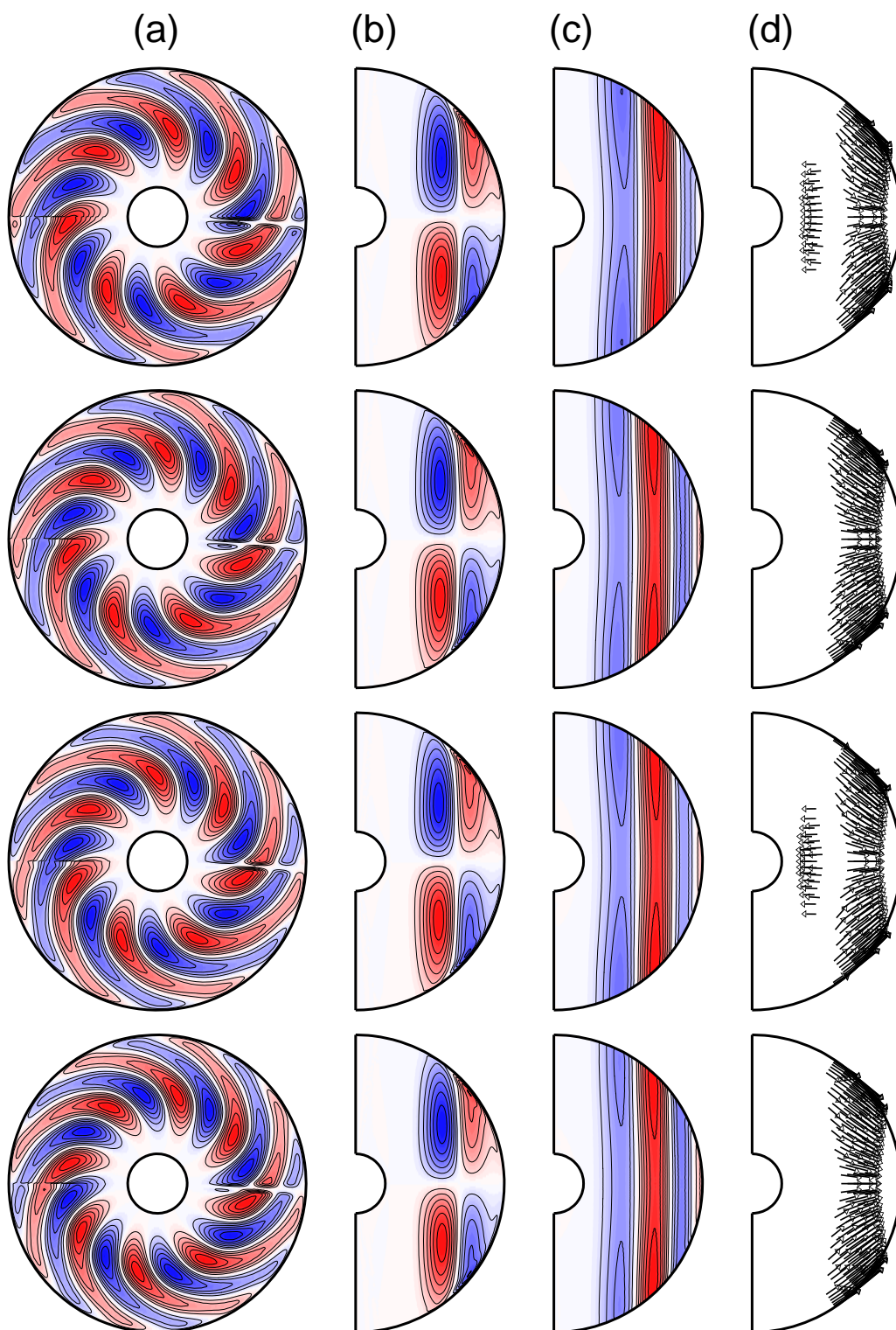
Figure 4.9: Same as Figure 4.2 but at $E_k^{-1} = 8000$, 9000, 10000, and 11000 in the top-down cases from top to bottom.
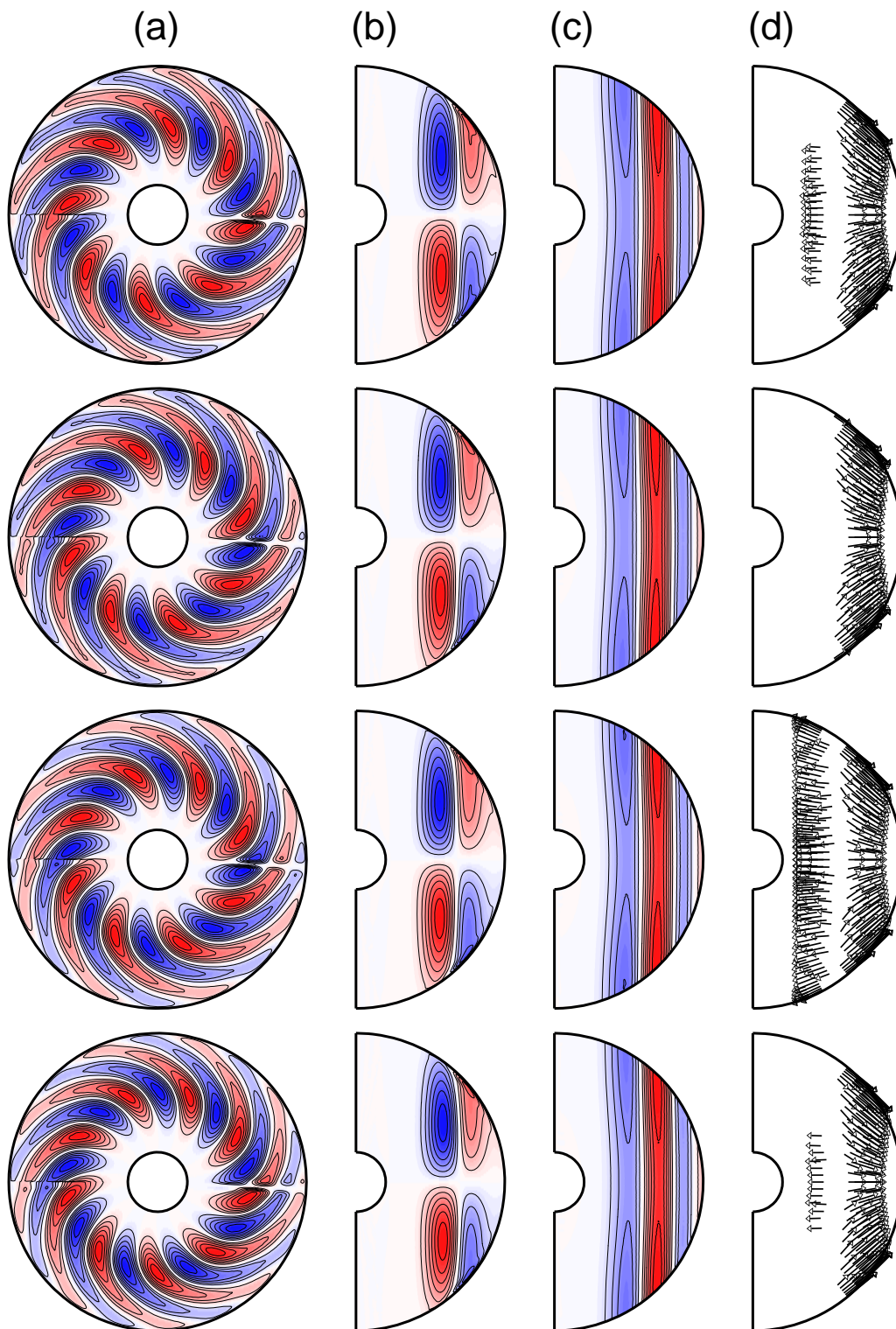
Figure 4.10: Same as Figure 4.2 but at $E_k^{-1} = 12000$, 13000, 14000, and 15000 in the top-down cases from top to bottom.
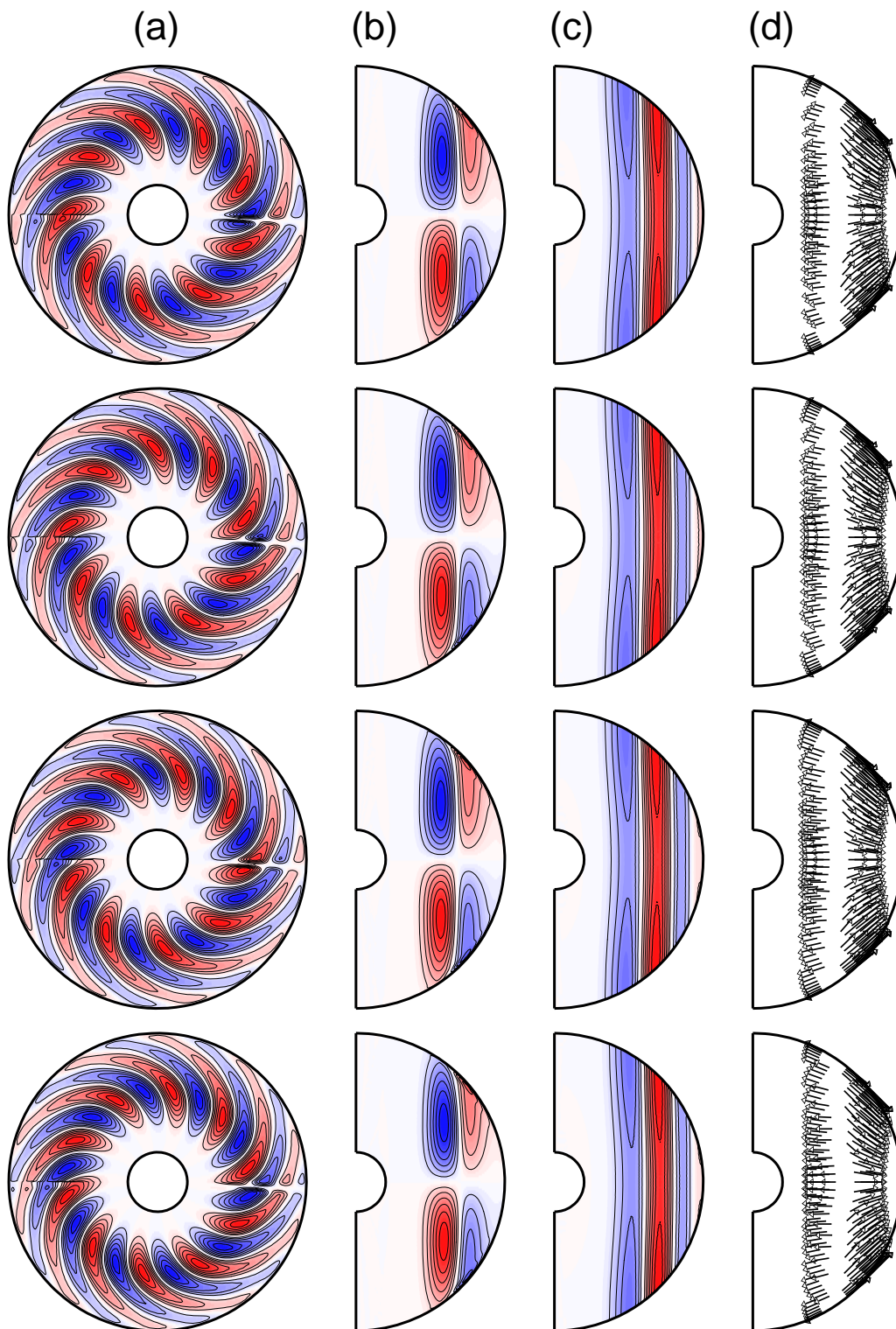
Figure 4.11: Same as Figure 4.2 but at $E_k^{-1} = 16000$, 17000, 18000, and 19000 in the top-down cases from top to bottom.

Kinetic energy budget

In chapter 2, we shows kinetic energy budget in the bottom-up and top-down type convection at $E_k = 5 \times 10^{-5}$ as the examples. Here, kinetic energy budget in all the cases are showed in following figures.
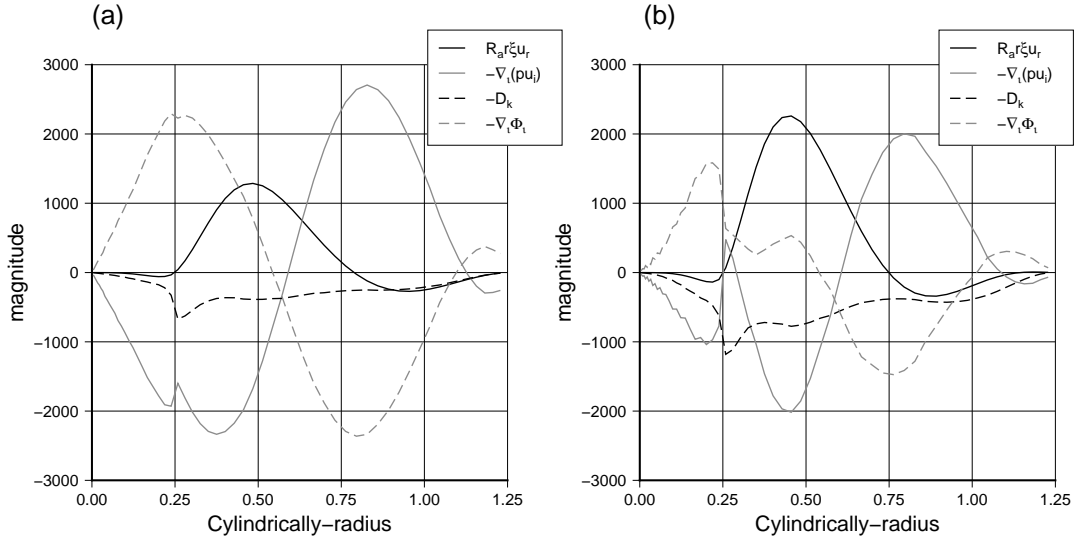
Figure 4.12: Cylindrically radial distributions of the axially and zonally averaged terms of the kinetic energy equation, calculated at $E_k^{-1} = 1000$ (a) and 2000 (b) in the bottom-up cases. Black solid line: generation term of kinetic energy by buoyancy force; grey solid line: term of dynamic energy flux convergence; black broken line: viscous dissipation term; grey broken line: term of viscous energy flux convergence.
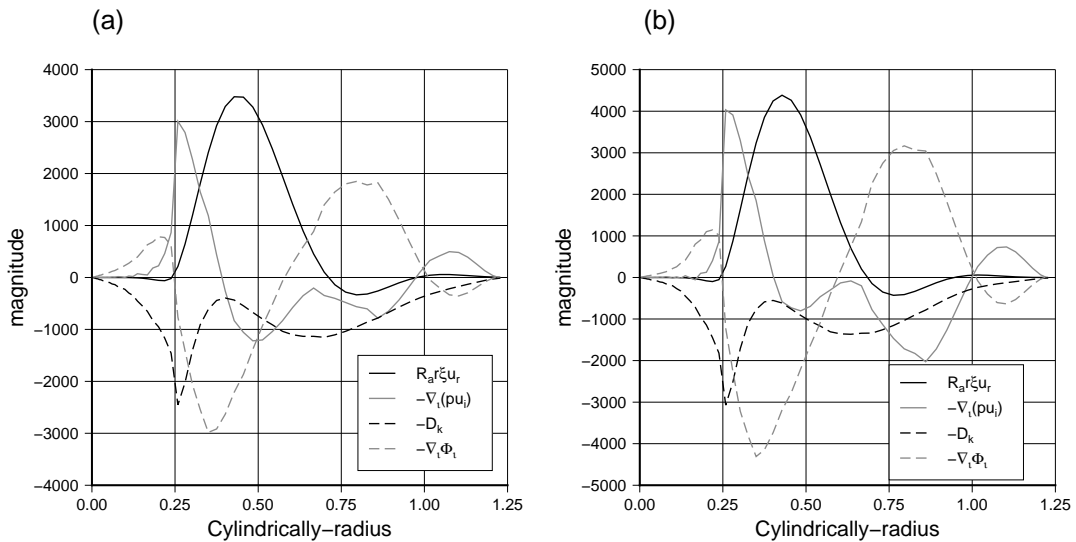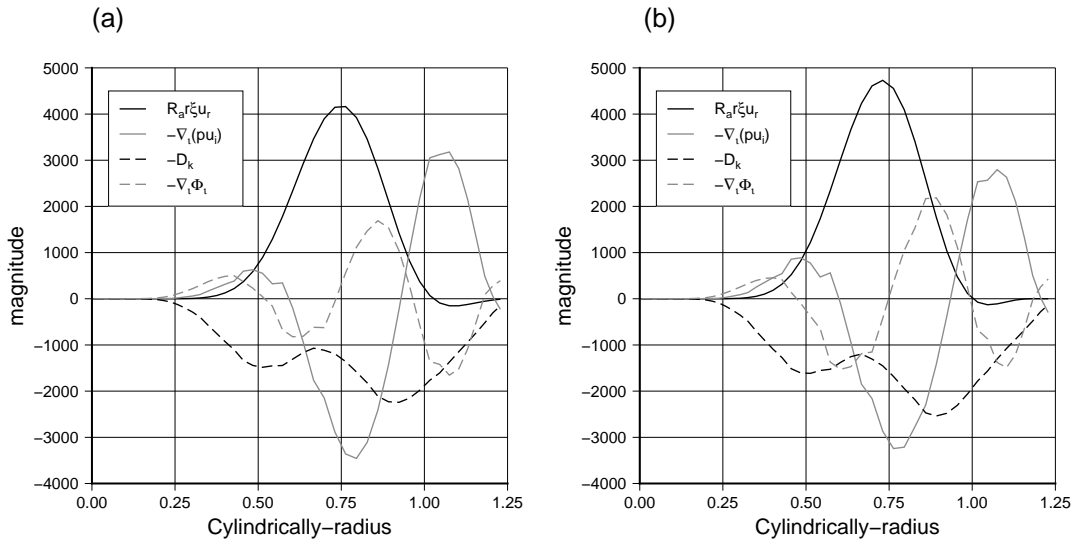

Figure 4.13: Same as Figure 4.12 but at $E_k^{-1} = 3000$ (a) and 4000 (b) in the bottom-up cases.
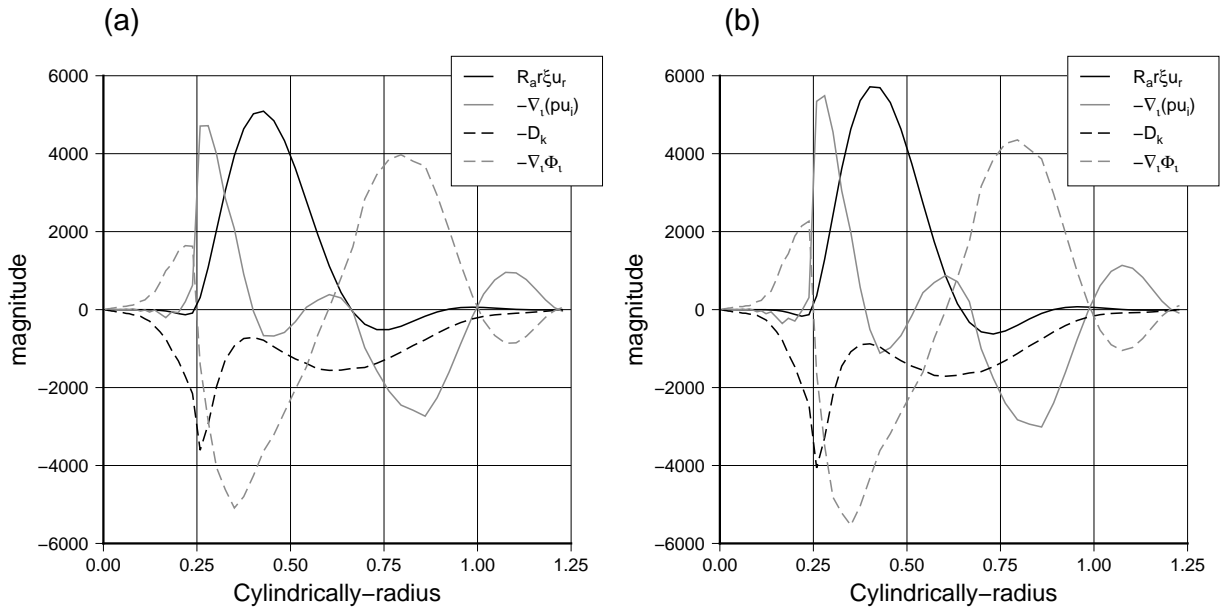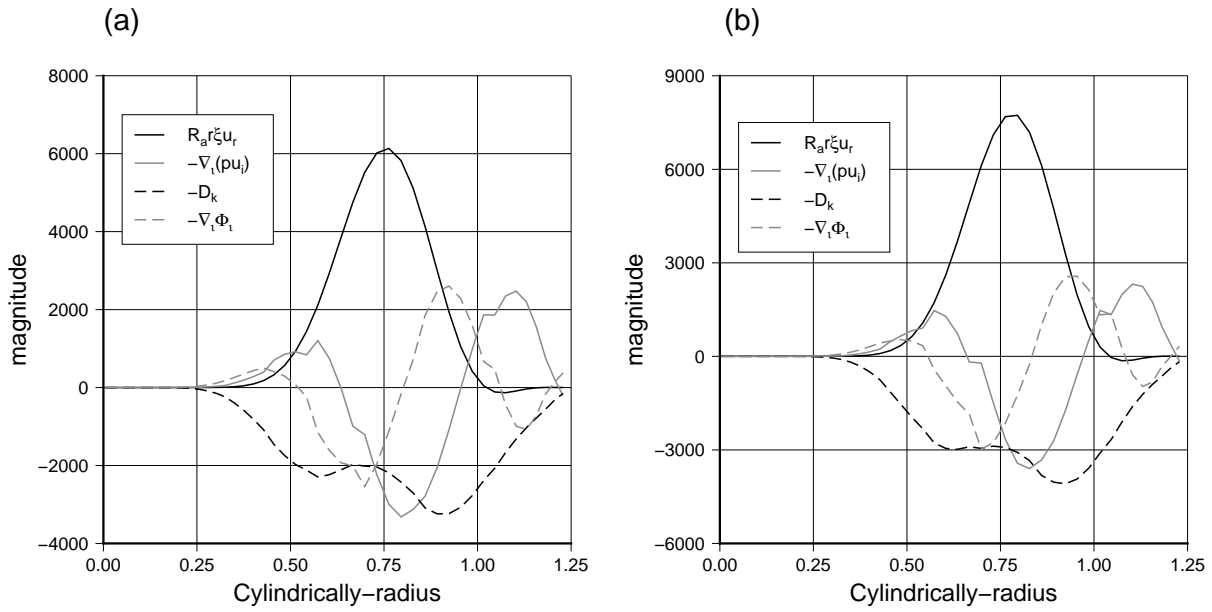
Figure 4.14: Same as Figure 4.12 but at $E_k^{-1} = 5000$ (a) and 6000 (b) in the bottom-up cases.
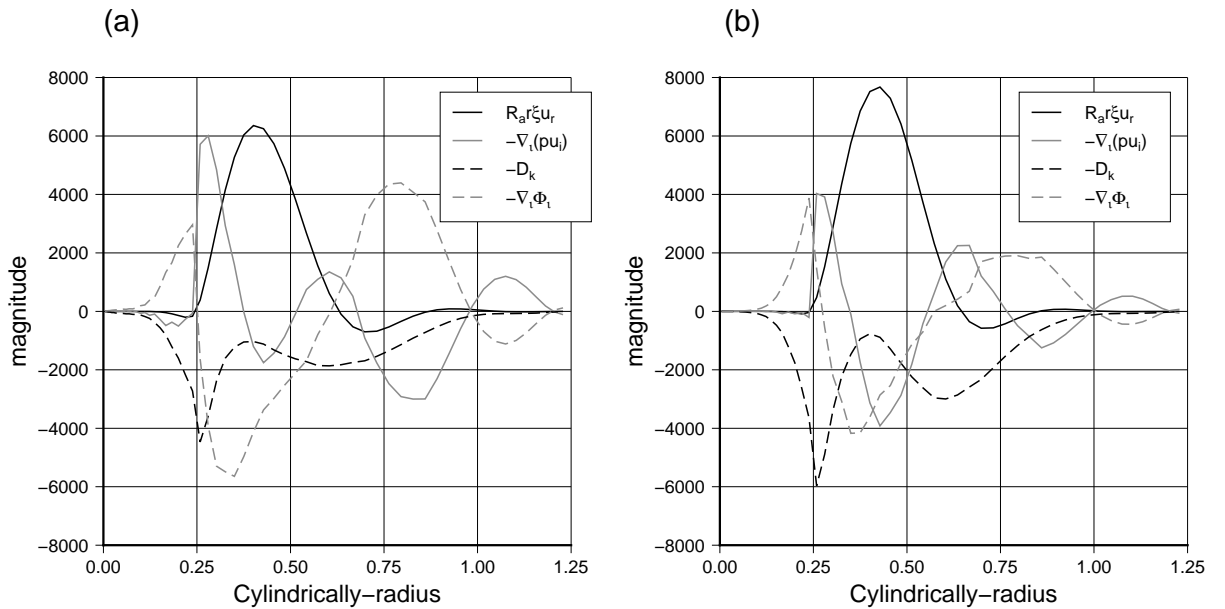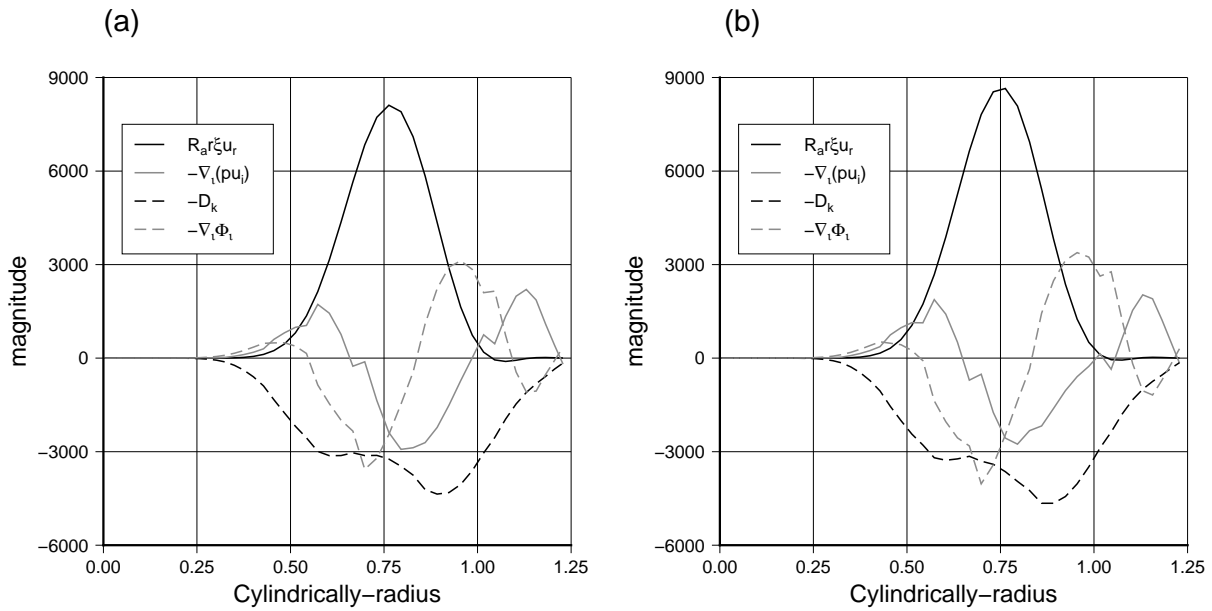

Figure 4.15: Same as Figure 4.12 but at $E_k^{-1} = 7000$ (a) and 8000 (b) in the bottom-up cases.
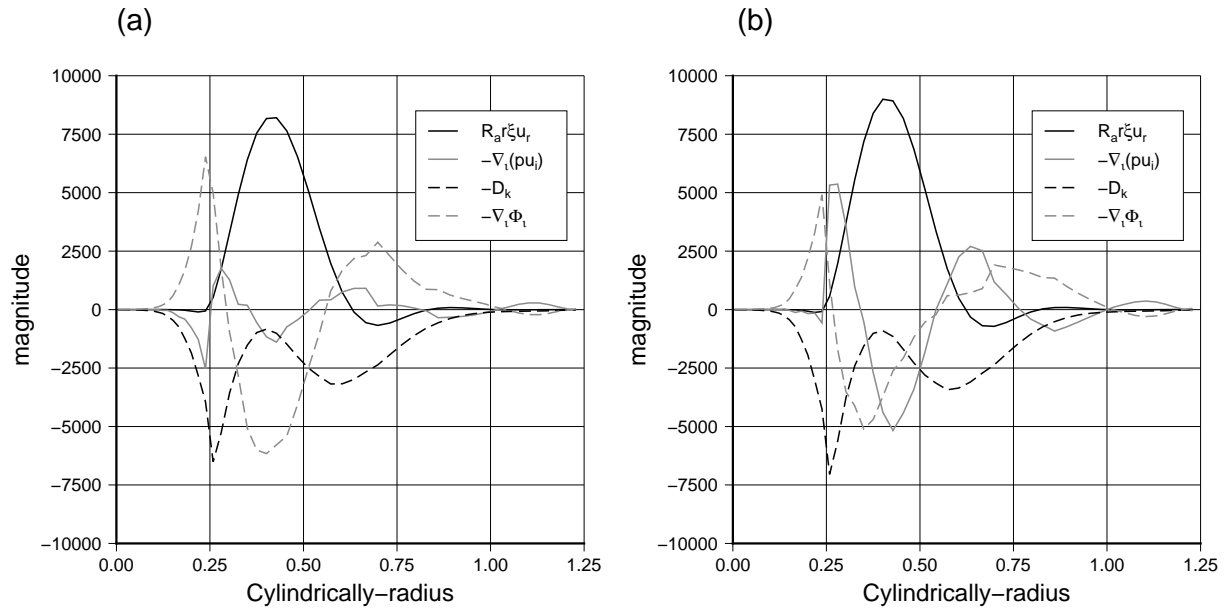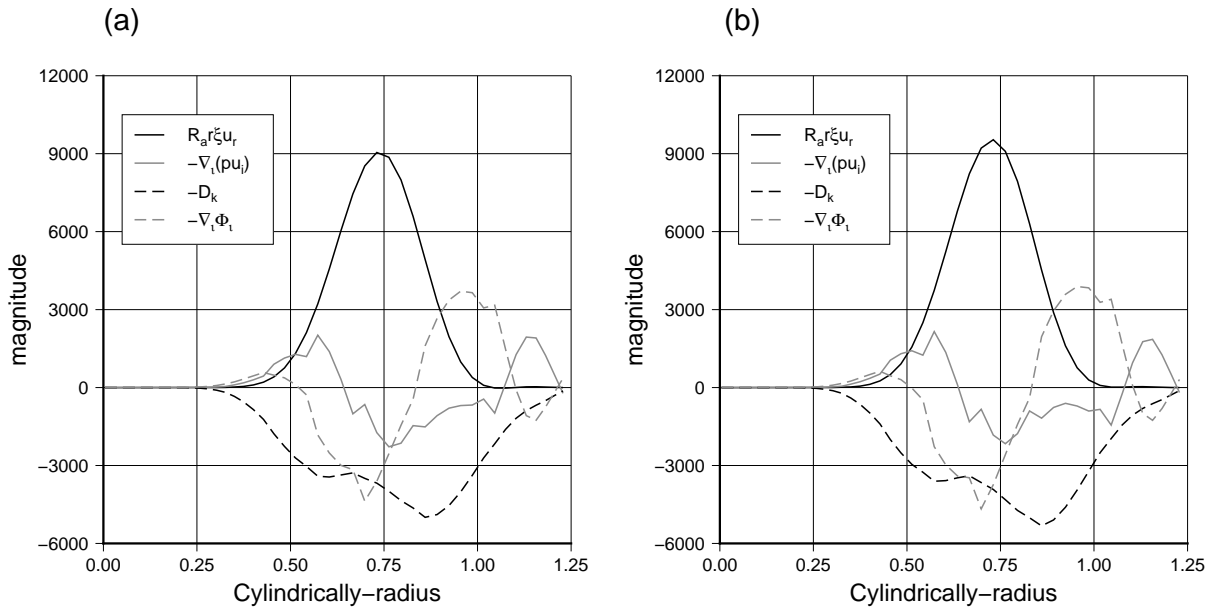
Figure 4.16: Same as Figure 4.12 but at $E_k^{-1} = 9000$ (a) and 10000 (b) in the bottom-up cases.
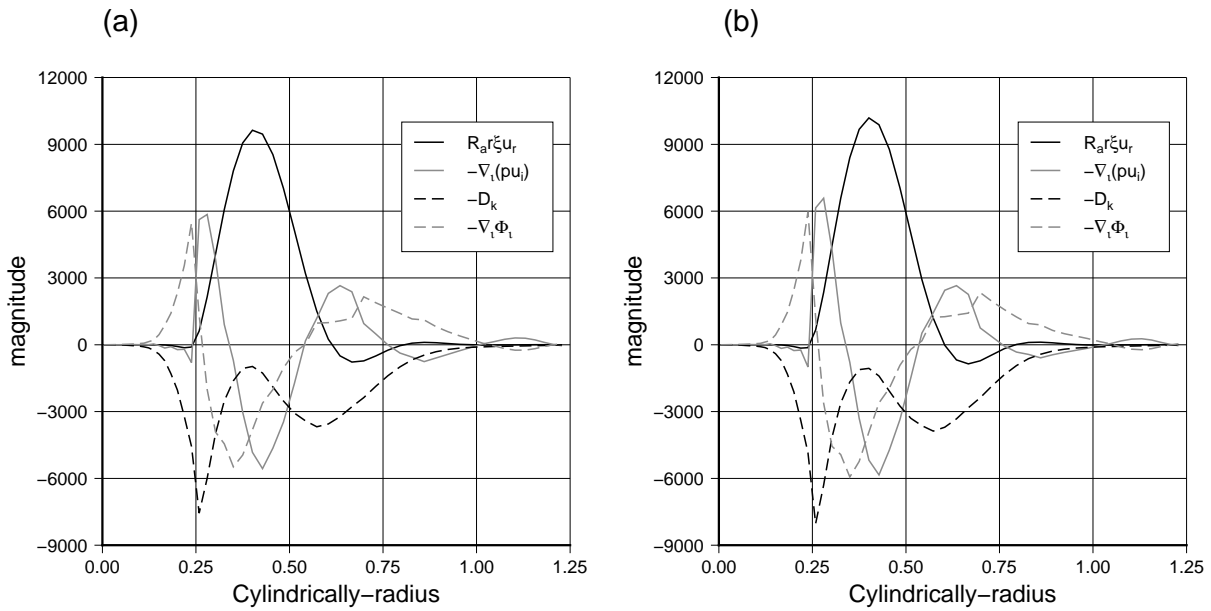
Figure 4.17: Same as Figure 4.12 but at $E_k^{-1} = 11000$ (a) and 12000 (b) in the bottom-up cases.
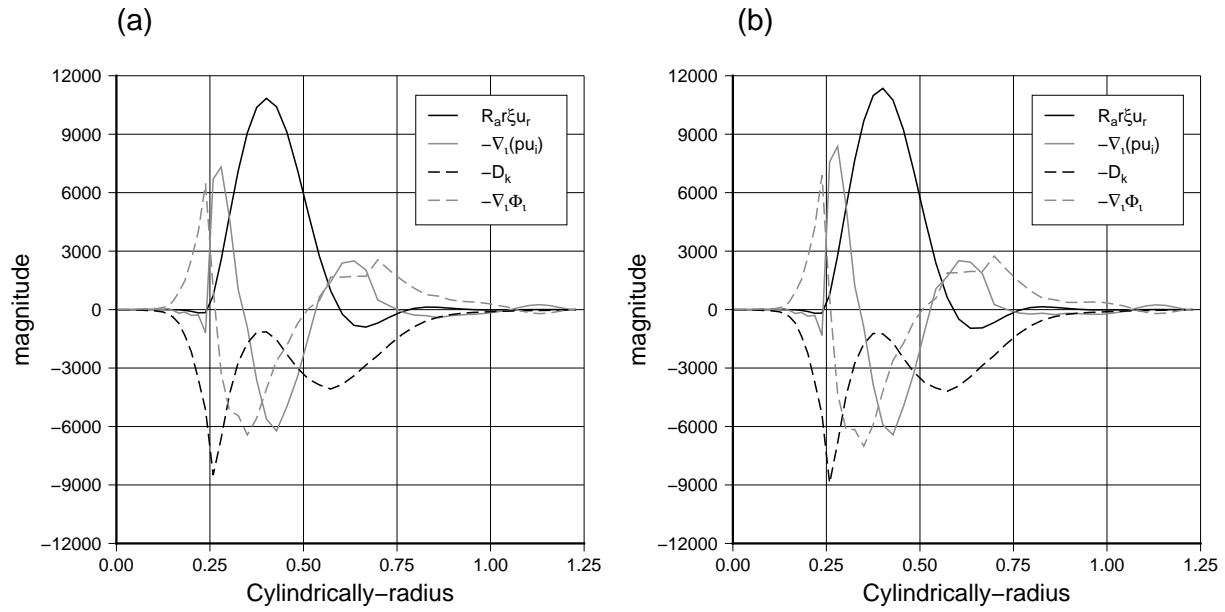
Figure 4.18: Same as Figure 4.12 but at $E_k^{-1} = 13000$ (a) and 14000 (b) in the bottom-up cases.
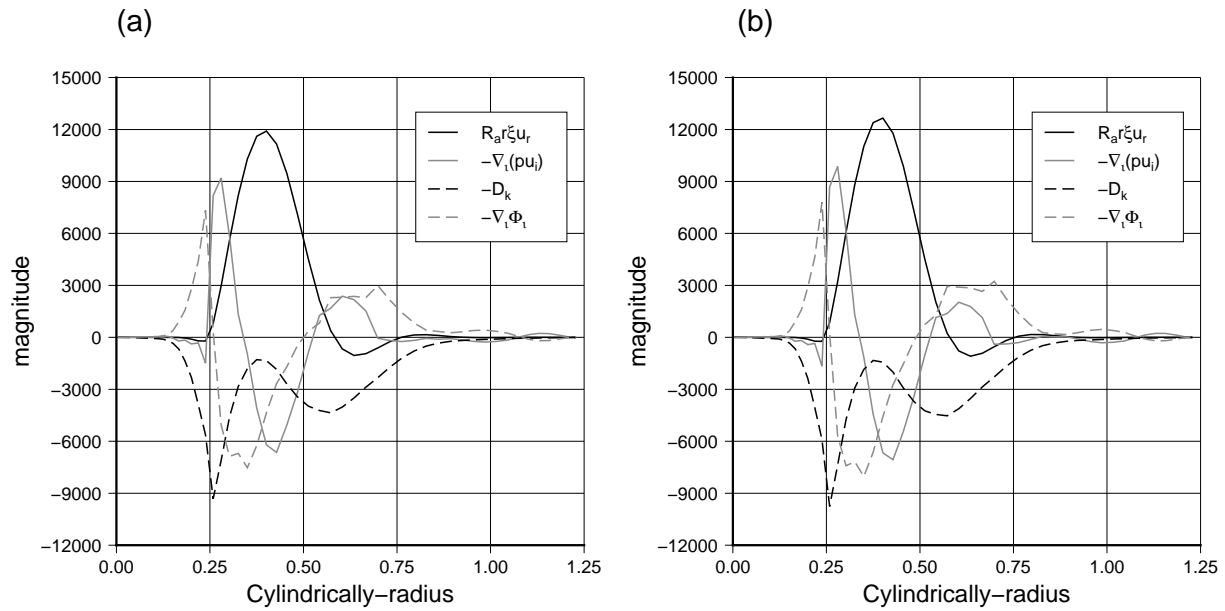
Figure 4.19: Same as Figure 4.12 but at $E_k^{-1} = 15000$ (a) and 16000 (b) in the bottom-up cases.
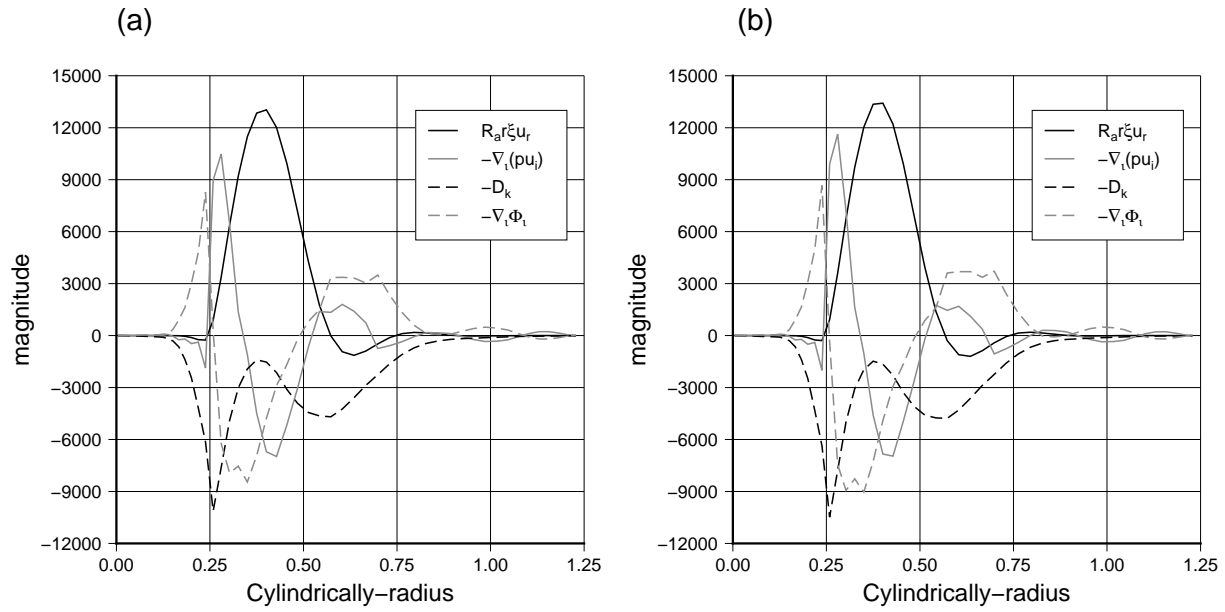
Figure 4.20: Same as Figure 4.12 but at $E_k^{-1} = 17000$ (a) and 18000 (b) in the bottom-up cases.
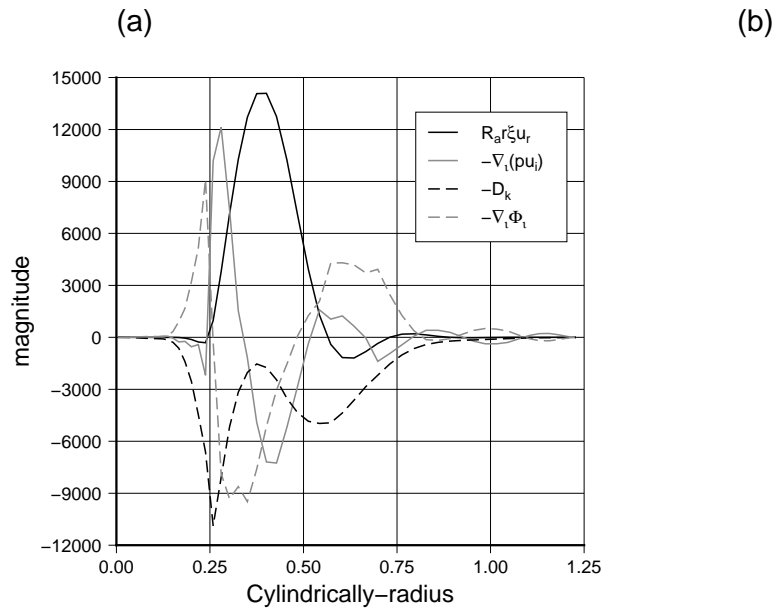
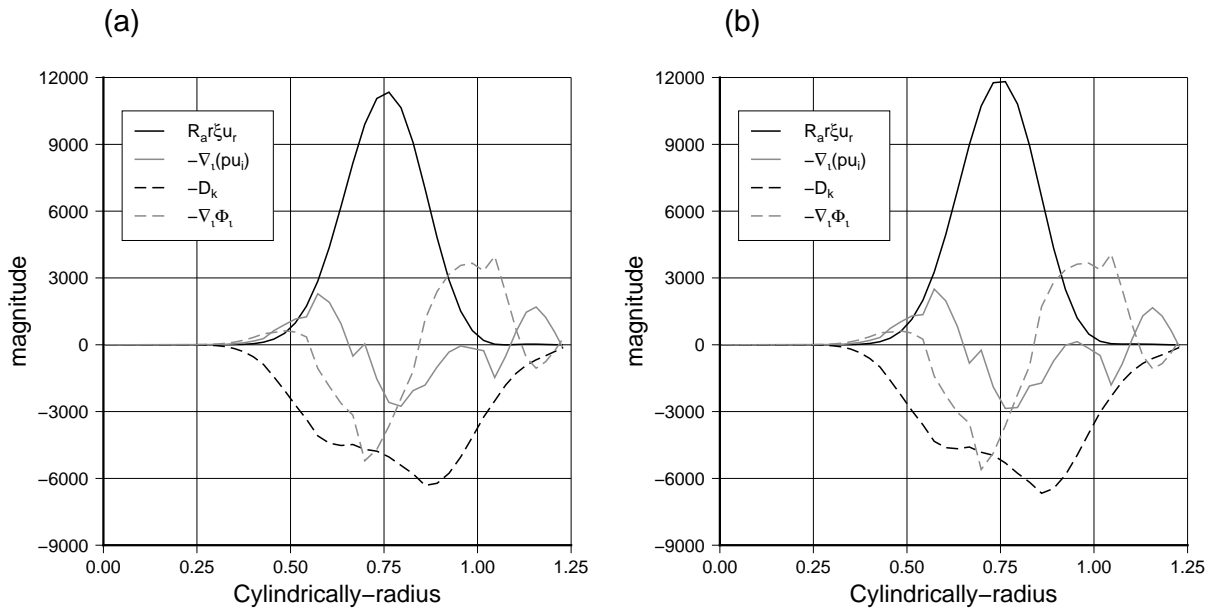Figure 4.21: Same as Figure 4.12 but at $E_k^{-1} = 19000$ (a) in the bottom-up case.
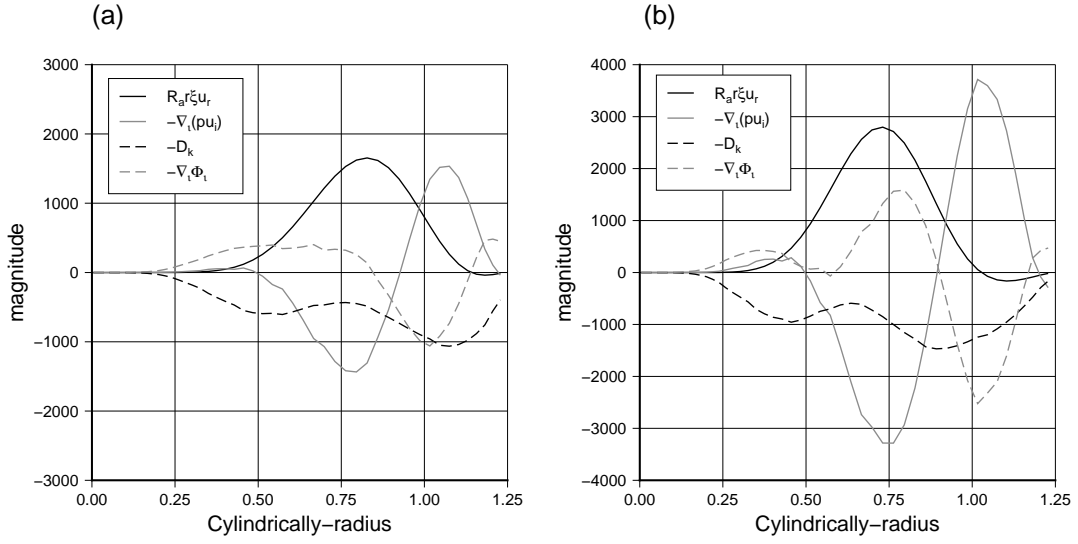
Figure 4.22: Same as Figure 4.12 but at $E_k^{-1} = 1000$ (a) and 2000 (b) in top-down cases.
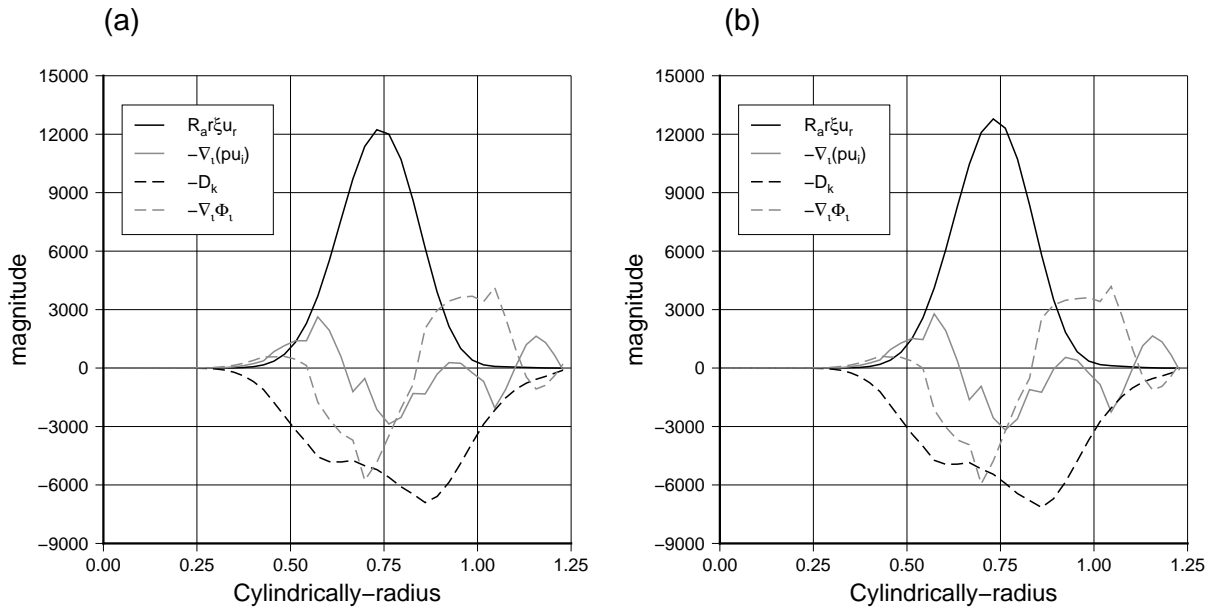

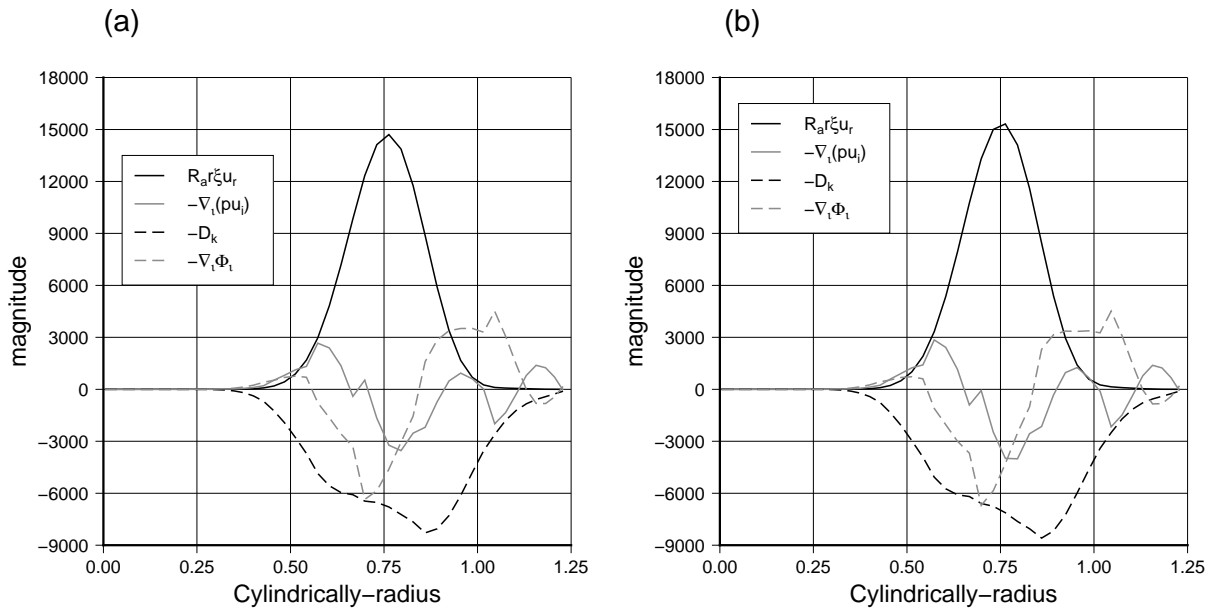Figure 4.23: Same as Figure 4.12 but at $E_k^{-1} = 3000$ (a) and 4000 (b) in top-down cases.

Figure 4.24: Same as Figure 4.12 but at $E_k^{-1} = 5000$ (a) and 6000 (b) in top-down cases.

Figure 4.25: Same as Figure 4.12 but at $E_k^{-1} = 7000$ (a) and 8000 (b) in top-down cases.

Figure 4.26: Same as Figure 4.12 but at $E_k^{-1} = 9000$ (a) and 10000 (b) in top-down cases.

Figure 4.27: Same as Figure 4.12 but at $E_k^{-1} = 11000$ (a) and 12000 (b) in top-down cases.

Figure 4.28: Same as Figure 4.12 but at $E_k^{-1} = 13000$ (a) and 14000 (b) in top-down cases.

Figure 4.29: Same as Figure 4.12 but at $E_k^{-1} = 15000$ (a) and 16000 (b) in top-down cases.
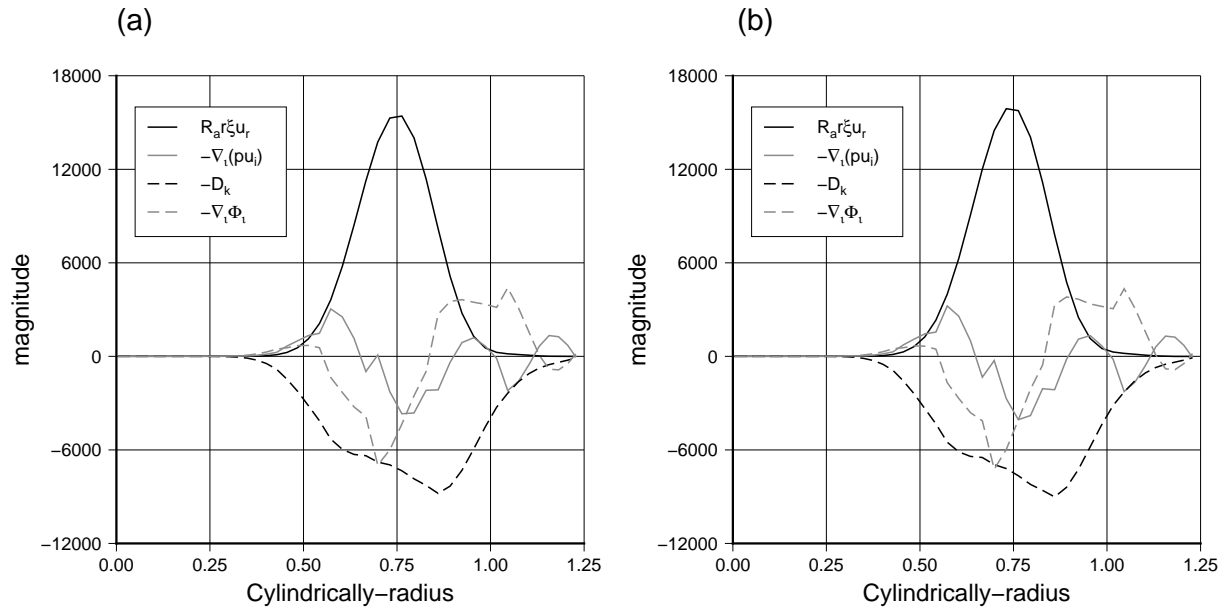
Figure 4.30: Same as Figure 4.12 but at $E_k^{-1} = 17000$ (a) and 18000 (b) in top-down cases.
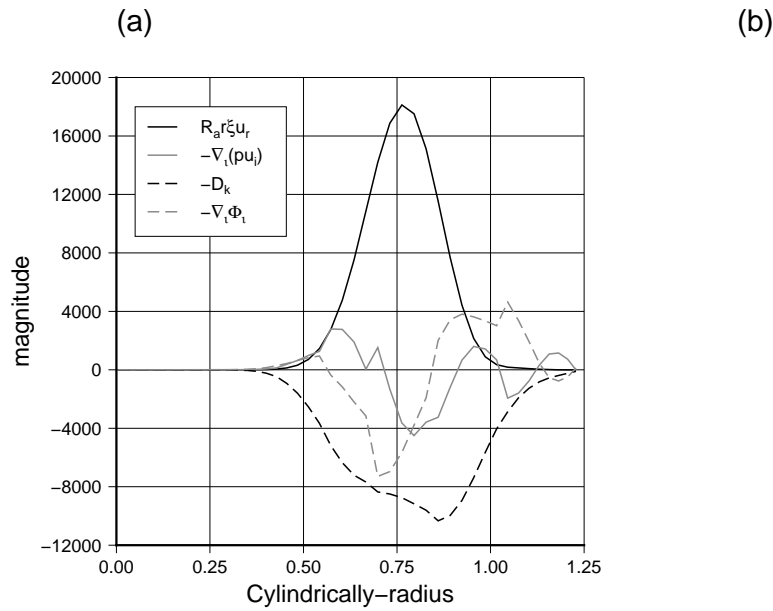

Figure 4.31: Same as Figure 4.12 but at $E_k^{-1} = 19000$ (a) in top-down case.